LASER INDUCED FREEZING

By

ASLAM HABIB CHOWDHURY

Bechelor of Science
Dacca University
Dhaka, Bangladesh
1976

Master of Science
Dacca University
Dhaka, Bangladesh
1977

Master of Science
Marquette University
Milwaukee, Wisconsin
1982

Submitted to the Faculty of the
Graduate College of the
Oklahoma State University
in partial fulfillment of
the requirements for
the Degree of
DOCTOR OF PHILOSOPHY
December, 1986

LASER INDUCED FREEZING

Thesis Approved:

Bru J Ack
Thesis Adviser

Larry E. Halliburton

Hugh L Scott

H. Olin Spivey

R.C. Powell

Norman N. Durham
Dean of the Graduate College

TO MY PARENTS

ACKNOWLEDGMENTS

The Author wishes to express the deepest appreciation to his major adviser, Dr. Bruce J. Ackerson, for his constant assistance, suppervision and guidance throughout the course for this work. Appreciation is also extended to the other mambers of the committee, Dr. R. C. Powell, Dr. L. E. Halliburton, Dr. H. L. Scott and Dr. H. O. Spivey. Additional thanks are also extended to Dr. W. Ford for serving as member in my original committee.

The Author also expresses his love and gratitude to Dr. Nemesio Caraballo for his friendship and advice. Appreciation extended to Frankie W. Jezercak, Dr. Hamzah A. Almoghvabi and Dr. Alharthi Abdulaziz for their help and friendship. Thanks extended to Khalid Loudiyi for his friendship and discussions.

We gratefully acknowlwdge the support by National Science Foundation, Division of Material Research, Low Temperature Physics Grants Nos. DMR 81-16119, DMR 85-00704 and the University Center for Water Research.

Finally, the author express gratitude to his wife, Milly, for her understanding and encouragement and express love to his son, Ibrahim and daughter, Silvia.

TABLE OF CONTENTS

LIST OF TABLES

LIST OF FIGURES

Figure Page

Figure Page

CHAPTER I

INTRODUCTION

Statement of the Problem

Colloids made of suspended polymer microspheres are very useful systems for studying many-body physics. They are physically well-characterized, inexpensive, and the particle order may show solid, liquid, and gaseous states under easily attained physical and chemical conditions. It is known that due to screened coulombic interactions, even a dilute aqueous suspension of charged particles can exhibit interparticle ordering over large distances compared to the particle diameter. Recently, these colloidal systems have been studied by a number of authors to examine statistical mechanical behavior (1 to 6). Since there is a similarity between these colloidal systems and molecular fluids, they become ideal candidates to test many theories of condensed phases, under both equilibrium and nonequilibrium conditions (7). Scattering of light from these colloidal systems provides information about static and dynamics of the interparticle order, similar to that obtained by x-ray and neutron scattering from pure atomic condensed matter states.

In this work we explore the effect of radiation pressure effects on the ordering in two dimensional colloidal liquid states. Using a crossed laser beam technique we should be able to impose a periodic (radiation) potential on the colloidal sample with a wavelength on the order of the average interparticle spacing. The colloidal particles, which have an index of refraction larger than the surrounding aqueous medium, should be drawn into the high intensity regions of the fringe pattern created by the crossed beams (1). The reorganization will destroy the Debye-Scherrer rings, which are produced on scattering light from an amorphous state where particle pairs maintain an average separation but random orientation, in favor of localized intensity maxima, which are produced by scattering from a diffraction grating of particles aligned with the fringe pattern. However, the particles also maintain there interaction to produce a registration between the rows of particles in the fringes. This interaction produces other density modes, not directly excited by the intensity potential. The result is that a solid like order may be induced in the sample by directly stimulating only one of its modes. This thesis describes the odessey to demonstrate this "laser induced freezing " phenomenon.

Purpose of This Thesis

While the main goal of this thesis is to demonstrate the phenomenon of "laser induced freezing", there are several subsidary problems which are explored as a result of this work:

1. A measurement of the scattering efficiency and amplitude of the directly excited density mode as a function of the strength of the applied intensity potential for hard sphere (weakly interacting) as well as soft sphere (strongly interacting) samples.

2. A measurement of the scattering efficiency and amplitude of the indirectly excited density modes as a function of strength of the intensity potential for the soft sphere (strongly interacting) samples.

3. A study and quantification the directly excited density mode for fixed strength of the intensity potential as a function of the fringe spacing of the applied field for both hard and soft sphere samples.

4. A study of the characteristic formation time of the directly excited density mode as a function of strength of the intensity potential for both hard and soft sphere systems.

5. A study of the characteristic formation time of the indirectly excited density modes as a function of strength of the intensity potential for soft sphere systems.

6. A measurement of the diffusion of hard spheres near a plane boundary in the presence of the normal radiation pressure force.

7. A study of the relaxation time constant of the directly and indirectly excited density modes for soft sphere systems as a function of both the strength of the intensity potential and fringe spacing.

Thus this thesis reports extensive experimental and some theoretical work on ordering in two dimensional colloidal systems subject to spatially periodic external fields. A short review of articles have been included with the theory and discussion in each chapter. In this way, each chapter is self-contained, having a review of literature, theory, experimental data, and discussion. While each chapter is self contained the first few chapters give background information helpful in the following chapters. A brief summary of the chapters is as follows: Chapter II is a development of experimental and theoretical tools relevant to the theme of this thesis, a review of literature and some experimental results, Chapter III discusses experimental details and apparatus, Chapter IV presents a study of hard sphere (weakly interacting) samples with a quantitative theoretical explanation, Chapter V presents a study of a soft sphere (interacting) sample, with a quantitative theoretical model and Chapter VI contains overall discussion, conclusion and suggestions for future work.

CHAPTER II

GENERAL BACKGROUND

Introduction

This chapter outlines severals topics which will be useful in discussing our experimental procedure and our results. We begin with scattering from single finite sized particles and then collections of particles. Measurement techniques including DLS (dynamic light scattering), CCIFS (crossed correlation intensity fluctuation spectroscopy) and CBT (crossed beam techniques) are discussed, as well as, the relations between these techniques. Finally we discuss some of the work of others on two dimensional fluid-solid systems.

Static Light Scattering

When x-ray radiation is incident on an atom, the surrounding electrons will undergo acceleration under the action of the electric field associated with the beam. Since an accelerated charge emits radiation, the atomic electrons emit and scatter the incident radiation. In this case the wavelength and size of the atom are the same order of magnitude. On the other hand, if an isolated arbitary shaped dielectric object is illuminated by a parallel beam of linearly polarized radiation of longer wavelength, then antecedent to becomes polarized in the electromagnetic field due to the displacement of the electrons with respect to the nuclei and also due to the partial orientation of any permanent dipoles that may be present. In the optical frequency range the effect of permanent dipoles is insignificant. For these long wavelengths we consider the individual dipoles to radiate uniformly in all directions (Rayleigh Scattering) in calculating the effect of the shape of the dielectric object on the scattered radiation.

Scattering from Finite Sized Particles

Now we consider a collection of scattering centers which radiate uniformly in all directions. The total electric field amplitude function, A(θ), is the sum of amplitude functions for scattering by each individual oscillator in a given direction as shown in figure 1 and is given by

$$A(\theta) = \sum_i \epsilon_i \exp(i\bar{K}\cdot\bar{r}_i) \qquad (2.1)$$

where $\bar{K}$ (= $\bar{K}i$ - $\bar{K}s$) is the scattered wave vector, the difference between the incident and scattered wave vectors

$\bar{r}$ is the distance of ith particle from the origin

and ϵ_i is a function depending on the scattering efficiency, the distance of the detector from

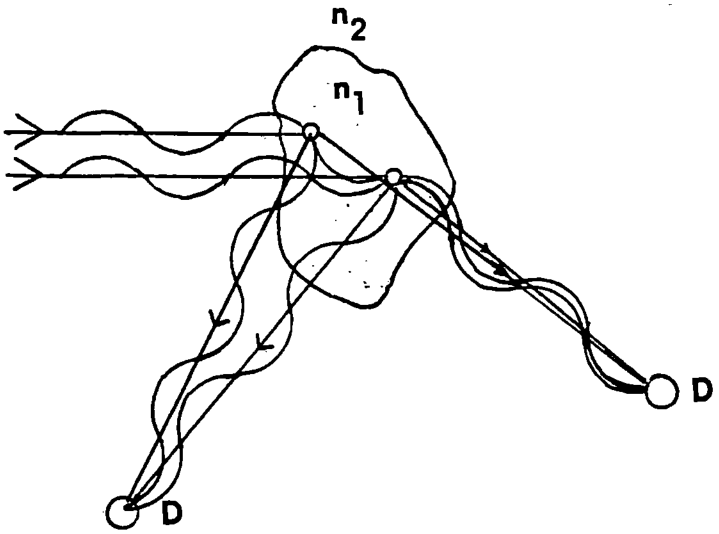

n_1 is the refractive index of the particle
n_2 is the refractive index of the surrounding
D is the position of constructive interference pattern.

Figure 1. Mutual Interference between each Oscillator in the Particle.

the scattering centers, and the incident amplitude which may depend on r_i. (For simplicity we will assume $\epsilon_i = 1$, except when stated otherwise).

In general this sum is very hard to evaluate since the position of each individual oscillator is not known. On the other hand we can treat each oscillator in a dielectric particle as a Rayleigh scatterer excited by the incident field and assume that it is unperturbed by the presence of the rest of the oscillators. We consider the case of incident radiation polarized perpendicular to the plane of scattering, where each oscillator scatters radiation to a point with different phase in general. Then the amplitude function of each oscillator is given (8) by

$$d\,A(\theta) = i\ \{(3\,k^3)/4\pi\}[(m^2 - 1)/(m^2 + 2)] \exp(i\delta)\ dV \qquad (2.2)$$

where m is the ratio of complex refractive index of the particle to the medium index of refraction

δ is the phase of the scattered radiation from each element at the observation position.

The resultant amplitude function which arises from interference of each wavelet is obtained by the vector sum (integral for continuous case) over all oscillators in the particle as

$$A(\theta) = i((3\ k^{3})/(4\pi))[(m^{2} -1)/(m^{2} + 2)] \int \exp(i\delta)\ dV. \qquad (2.3)$$

The scattered intensity of this object is directly proportional to the absolute value square of the amplitude function,

$$I \propto |A(\theta)| = |\ i((3k^{3}V)/(4\pi))[(m^{2}-1)/(m^{2}+2)]|^{2} P(\theta) \qquad (2.4)$$

and $$P(\theta) = (1/V^{2})|\int \exp(i\delta)\ dV|^{2} \qquad (2.5)$$

is known as particle form factor. It is clear that scattered intensity is directly proportional to the form factor, $P(\theta)$.

Rayleigh scattering is restricted to particles small in diameter compared to the radiation wavelength. On the other hand Rayleigh-Debye or Rayleigh-Gans results given in equation (2.4) and (2.5) assume that neither the ratio of the refractive index of the medium to the object is much larger than unity nor that the phase shift corresponding to any point in the object be large, i.e., that

$$|m - 1| \ll 1 \qquad (2.6)$$

and $$2ka|m - 1| \ll 1 \qquad (2.7)$$

where a is the radius of the sphere

and $|K|$ $(= 2\pi/\lambda)$ is the incident wave vector magnitude. For this reason neither the radius of the particle nor the relative refractive index can be taken too large.

Within the restrictions of these assumptions, the form factor, $P(\theta)$, of a homogeneous sphere can be obtained by integrating in equation (2.5) over a sphere of radius a. The result (8) is given by

$$\begin{aligned} P(\theta) &= |(3/u^3)[\sin(u) - u\cos(u)]|^2 \\ &= (9\pi/2u^3)[J_{3/2}(u)]^2 \end{aligned} \qquad (2.8)$$

where $u = Ka = 2ka \sin(\theta/2)$

and $J_{3/2}(u)$ is the three-halves order Bessel function.

The range and validity of Rayleigh-Debye or Rayleigh-Gans theory for a sphere has been investigated (8,9) by M.Kerker and W.A.Farone and his co-workers. They found that for the relative refractive index, m, close to unity as well as a phase shift less than unity, this theory agrees within 50% to 100% with the exact calculation for the sphere using Mie theory. On the other hand, numerical calculations of the anomalous diffraction approximation were done for the form factor of sphere larger than wave length and for a relative refractive index greater than unity (9). It was found that this calculation agrees with Mie theory to within 50% to 15% as the scattering angles increase from 10 to 20 degrees for a sphere of radius, a = 1 um, radiation wavelength, $\lambda =$ 0.488 um and relative refractive index, m = 1.2. Thus the Rayleigh-Gans theory gives good agreement at small scattering angles for larger radius particles, as well.

The exact theory or Mie theory for scattering from a sphere of arbitary size and any refractive index is obtained by using Maxwell's equations with appropriate boundary condtions (10,11). The solution for the resulting amplitude function for perpendicular and parallel polarization of the electric field is given by

$$A_1(\theta) = \sum_{n=1}^{\infty} [(2n + 1)/n(n + 1)]\{a_n t_n(\cos(\theta)) + b_n T_n(\cos(\theta))\} \tag{2.9}$$

and

$$A_2(\theta) = \sum_{n=1}^{\infty} [(2n + 1)/n(n + 1)]\{b_n t_n(\cos(\theta)) + a_n T_n(\cos(\theta)\}, \tag{2.10}$$

respectively. The coefficient a_n and b_n are in general complex, and are tabulated (12,13) for arbitary values of the relative refractive index and sphere radius. The functions $t_n(\cos(\theta)$ and $T_n(\cos(\theta))$ are given by

$$t_n(\cos(\theta)) = d\, P_n(\cos(\theta))/d \cos(\theta) \tag{2.11}$$

and

$$T_n(\cos(\theta)) = \cos(\theta)\ t_n(\cos(\theta) - \{\sin(\theta)\ [d\ t_n(\cos(\theta))/d\ (\cos(\theta))]\} \tag{2.12}$$

where $P_n(\cos(\theta))$ are the Legendre polynomials.

Scattering from a Collection of Particles

Let us consider a collection of particles suspended in a liquid. If these particles are randomly positioned (no long range order) and subjected to a laser light, then the scattered radiation will evidence no net interference between particles and the single particle form factor will dominate the scattered intensity distribution. If the particles interact strongly enough that they maintain an average separation from one another (short range order), the scattered radiation intensity pattern will be similar to that for x-ray (or neutron) scattering from liquids or amorphous solids. Debye-Scherrer rings concentric with the incident beam will be observed. The diameter (scattering angle) of these rings is a measure of the average particle separation and their width is a measure of the volume over which particles are correlated. If the interaction between particles is sufficiently strong, they may order into a regular lattice structure (long range order). Light scattered from these systems behaves similar to x-ray (or neutron) scattering from crystalline solids and Bragg's law applies. According to Bragg's law scattering will occur only for certain angles given by:

$$2d \sin(\theta) = \lambda \tag{2.13}$$

where θ is the half angle of scattering

λ is the wavelength used

and d is the average separation of planes of particles in the crystalline lattice.

Thus the Bragg's scattering can be used to determine particle separations from knowledge of λ and measurements of θ for crystalline systems. An example of Bragg scattering is shown in figure 2a. This is produced by focusing a single laser beam to a area of diameter 50 um in a sample of colloidal particles. The gap thickness is about 30 um which forces the particles to form a monolayer. This monolayer is observed directly using a microscope. The centeral spot in the scattering pattern is the unscattered main beam. From this scattering pattern the scattering angles are determined. In appendix (A), it is shown exactly the procedure for calculating these angles, as care must be taken to account for scattering geometry and refraction effects.

The separation between the "planes" of particles was obtained using equation (2.13). These scattering "planes" are indicated as shown in figure 2b. In this figure the particle "planes" (indicated by solid lines) are responsible for producing the scattering intensity maxima closest to the main beam in figure 2a, the first order maxima. The dash lines indicate the planes responsible for the second order intensity maxima in figure 2a. The real space structure and scattering pattern crosspond qualitatively. Quantitatively we have a hexagonal close pack structure, (hcp), whose lattice constant, a = 2.3 um can be found by using relation

$$a = 2d(hk)\sqrt{(h^2 + hk + k^2)/3} \qquad (2.14)$$

where d(hk) is the separation of the planes

and h as well as k are Miller indices.

Since the physical diameter of the particles is 1 um, the lattice parameter for touching particles would be a = 0.86 um. However, these strongly charged particles maintain a much larger separation producing the observed lattice constant.

To analyze the scattered intensity for an arbitrary collection of interacting scatters, the more general amplitude of scattering function, E(k), given by

$$E(k) = f_a(\theta) \sum_i \exp(i\bar{k}\cdot\bar{r}_i), \qquad (2.15)$$

where $|f_a(\theta)|^2 = P(\theta)$ is the single particle form factor (assumed the same for all particles) and the sum is taken over all the particle positions. Note that this is of the same form of equation (2.1) for considering internal interference of single particles. We now apply the same form for interparticle interference.

The scattered intensity, I, is directly proportional to the absolute value square of E(k) and is given by

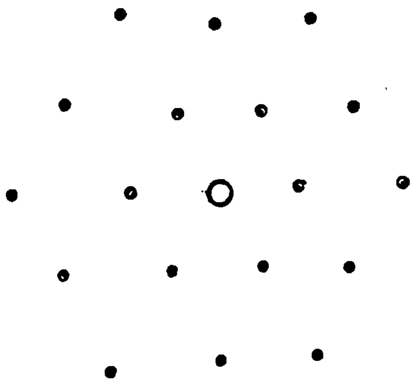

Figure 2a. A Tracing of Bragg's Spots produced by Light Scattering from a Highly Interacting Colloidal Sample

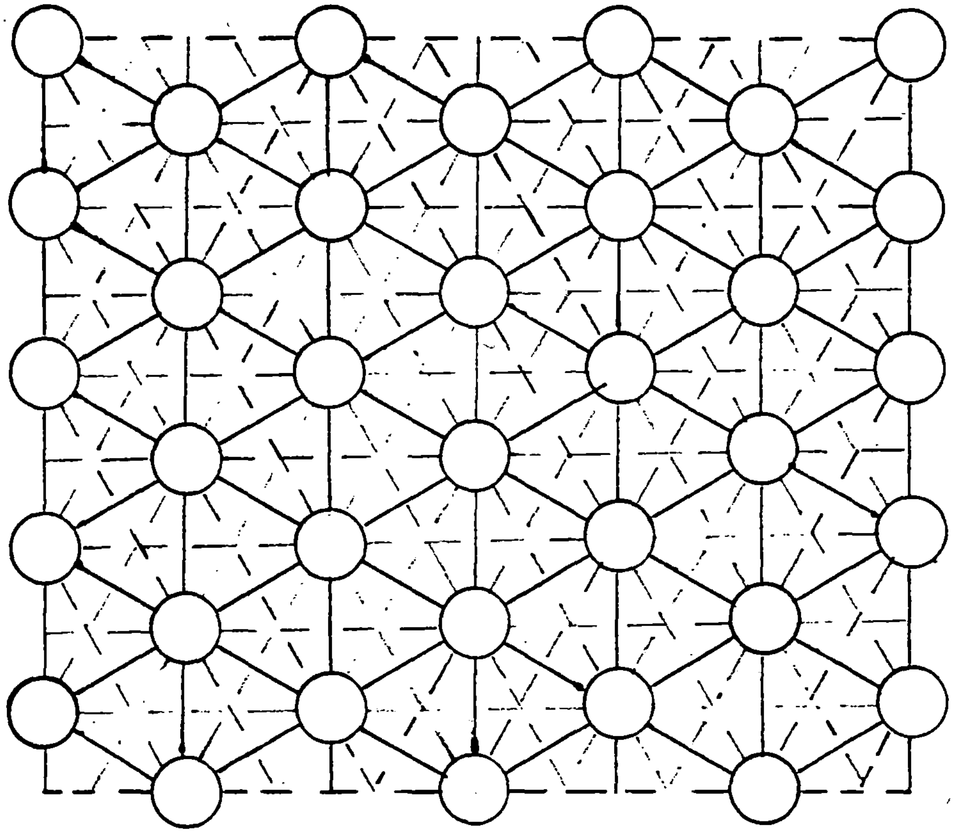

Figure 2b. The Real Space Structure of above Scattering Pattern

$$I \propto |E(k)|^2 = |f_a(\theta) \sum \exp(i\bar{k}\cdot\bar{r}_i)|$$
$$= |f_a(\theta)|^2 S\ (k) \qquad (2.16)$$

where $$S_I(k) = \sum_i \sum_j \exp(i\bar{k}\cdot(\bar{r}_i - \bar{r}_j) \qquad (2.17)$$
is called the instantaneous static structure factor. The sum can be split into two different types of terms: those for which $i = j$, the self part; and the mutual part where $i \neq j$. In the case of a liquid the particles are always sufficiently randomly positioned that the sum is diffcult to evalute. However, let us assume that there are N particles in our sample. Then the liquid structure factor can be written in terms of $S_I(k)$ as follows (15):

$$S(k) = \langle \sum_{ij} \exp\ (i\bar{k}\cdot(\bar{r}_i - \bar{r}_j))\rangle = \langle S_I(k)\rangle \qquad (2.18a)$$

and $$S(k)/N = 1 + n_o \int d^3r\ \exp(i\bar{k}\cdot\bar{r})[g(r) - 1] \qquad (2.18b)$$

where n_o is the average particle density, $g(r)$ is the pair distribution function and the brakets represent an equilibrium ensemble average.

Thus the pair distribution function $g(r)$ is related to structure factor $S(k)$ via a fourier transform. This is important because the pair distribution function is defined as

$$g(r) = n(r)/n_o \qquad (2.19)$$

where $n(r)$ is the radial density distribution function of the liquid.

Obviously the pair distribution function, $g(r)$ and radial density function have same type of behavior, i.e. as $r \rightarrow \infty$, $n(r) \rightarrow n$ and $g(r) \rightarrow 1$. What is important is that this pair distribution function gives the conditional probability for finding a particle a distance r from the origin given a particle positioned at the origin. This probability can be determined from scattering experiments.

Dynamic Light Scattering

So far the static structure factor is discussed for average particle positions, no motion of the particles is considered. But in reality the microspheres exhibit Brownian motion. As a result the scattered intensity will fluctuate in time. The rate at which the intensity changes gives a measure of particle diffusion rates, polydispersity, size, etc with suitable assumptions. If the particles are correlated, then this information about the dynamic structure factor can be obtained from the equilibrium fluctuations in position.

The dynamic light scattering (DLS) technique is a very powerful method to obtain this information. In DLS the measured photon correlation function can be expressed as intensity correlation function, $C(K,T)$. This correlation function, $C(k,T)$ is given by

$$C(k,T) = \langle I(k,t+T)\ I(k,t)\rangle / \langle I(k,t)\rangle^2 \qquad (2.20)$$

where $I(k,t)$ is the intensity at time t at the detector

$I(k,t+T)$ is the intensity at the later time t+T at the detector

and $\langle I(k,t)\rangle$ is the time averaged intensity.

Furthermore, this correlation function can be expressed in terms of electric field correlation function, $g_1(k,T)$. In the gaussian limit when there are a large number of independent correlations regions in the scattering volume, we have the Seigert relation (16)

$$C(k,T) = (1 + c|g_1(k,T)|^2) \qquad (2.21)$$

where c is an apparatus constant often called the signal to noise ratio.

and $$g_1(k,T) = \langle E(k,t+T)\ E(k,t)\rangle / \langle |E_S|^2\rangle. \qquad (2.22)$$

The electric field correlation function or intermediate scattering function, $g_1(k,T)$ is the dynamic analogue of $S(k)$ and is related to a time dependent two particle distribution function via fourier transformation. Hence $E(k,t)$ and $E(k,t+T)$ are scattered electric fields at time (t) and (t+T), respectively. The instantaneous electric field produced by scattering from the collection of Brownian particles in the sample is given in equation (2.15), as in the static case. So the two time electric field correlation function is given by

$$\langle E(K,t+T)\ E(K,t)\rangle = |f_a(\theta)|^2 \ \langle \exp i\bar{K}\cdot(\bar{r}_i(t) - \bar{r}_j(t+T)) \rangle . \qquad (2.23)$$

In the case of N identical noninteracting particles in the scattering volume the correlation function becomes (17)

$$\langle E(K,t+T)\ E(K,t)\rangle = N\ |f_a(\theta)|\ \langle \exp i\bar{K}\cdot[\bar{r}(t+T) - \bar{r}(t)]\rangle \qquad (2.24)$$

where N is the number of particle in the scattering volume

$|f_a(\theta)|^2$ is the single particle form factor (and geometry effects)

$\bar{r}(t)$ is the position of the particle at time t

and $\bar{r}(t+T)$ is the position of the same particle at later time (t+T).

When these particles exhibit simple Brownian motion, the correlation function further simplifies to

$$\langle E(K,t+T)\ E(K,t)\rangle = N\ |f_a(\theta)|^2\ [\exp(iw\ T)]\ \{\exp(-D_o K^2 T)\} \qquad (2.25)$$

where D_o is the self-diffusion constant of the Brownian particles, and according to the Stokes-Einstein relation D_o

$= KT/(6\pi\eta a)$ for spherical particles of radius, a, with viscosity of the medium, n.

The correlation function, C(K,T) is then found to be

$$C(k,T) = 1 + c\ \exp(-2D_0 k^2 T). \qquad (2.26)$$

When the Brownian particles are interacting, the form for C(K,T) given in equation (2.26) is not correct. Rather the decay is non-exponential in time, in general, and is expressed in terms of a cumulant expansion as follows (18,19):

$$C(k,T) = 1 + C\ \exp[-2(K_1 t - K_2 t^2/2! + K_3 t^3/3! - .....)] \qquad (2.27)$$

The cumulants have been derived (18,19) using equation (2.24) and a generalized diffusion (20) or Langevin equation (21) for the particle dynamics. The first cumulant in the absence of hydrodynamic interactions is given by

$$K_1 = D_0 k^2/S(k) \qquad (2.28)$$

where all quantities have been defined previously. The second and higher cumulants become important at intermediate values of k for strong interactions, in general. On the other hand, C(K,T) for non-interacting particles is given by equation (2.26) ($K_1 = D_0 k^2$, $K_{n>1} \rightarrow 0$). For dilute system of hard spheres (22), $K_I = D_0 k^2(1 + b\,\phi)$ in the small k limit when the effect of both S(k) and hydrodynamic interactions are included. Here b = 1.45 is the "first Virial coefficient" for hard spheres. Polydispersity, a distribution of particles size and/or diffusion constants, will also give a non-exponential time decay for C(k,T) which must be analyzed using a cumulant expansion (21). We refer the interested reader to the liturature cited for more detailed discussions of polydispersity and interactions.

Cross-Correlation Intensity Fluctuation Spectroscopy

Cross-correlation intensity fluctuation spectroscopy (CCIFS) is a relatively new method of light scattering. In contrast to the standard scattering techniques which monitor the static or dynamic structure factors (which are related to particle pair correlation functions), the CCIFS technique is sensitive to higher order particle correlation functions (2,3).

In these experiments two detectors are used to monitor the scattering from a small illuminated volume in the sample. Only a few correlation regions (local structure) are observed and the scattered radiation is nongaussain in general (2,3). Generally, in these experiments, one detector is positioned at a fixed wavevector k and the other is scanned over a series of values q. The intensities are crossed correlated to find the CCIFS function, which is defined as

$$C(k,q,T) = \langle I(k,0)\ I(q,T)\rangle / \langle I(k)\rangle\langle I(q)\rangle \qquad (2.29)$$

and is a generalization of the dynamic light scattering function (equation (2.20)) to two wavevectors. Assuming the single scattering Born approximation (as with the DLS expression) C(k,q,T) may be expanded as follows:

$$\begin{aligned} C(k,q,T) = \langle \sum_i \sum_j \sum_l \sum_m & \epsilon[\bar{r}_i(0)]\ \epsilon[\bar{r}_j(0)]\ \epsilon[\bar{r}_l(t)] \\ & \epsilon[\bar{r}_m(t)]\ \exp\{i\bar{k}\cdot[\bar{r}_i(0) - \bar{r}_j(0)] \\ & + i\bar{q}\cdot[\bar{r}_l(t) - \bar{r}_m(t)]\}\rangle / S(\bar{k})S(\bar{q}) \qquad (2.30) \end{aligned}$$

where
$$\begin{aligned} S(\bar{k}) = \langle \sum_i \sum_j & \epsilon[\bar{r}_i(0)]\ \epsilon[\bar{r}_j(0)]\ \exp\{i\bar{k}\ [\bar{r}_i(0) - \\ & \bar{r}_j(0)]\}\rangle \qquad (2.31) \end{aligned}$$

is the static structure factor. Because the scattering volume is small, the static structure factor and C(k,q,T) are generalized to include the fluid amplitude factor $\epsilon(r)$ which determines the size of the scattering volume. For $\epsilon(r) \equiv 1$ everywhere, S(k) reduces to the previous result given in equation (2.16).

Experimental results have been obtained for a two dimensional monolayer of strongly interacting colloidal particles (2,3) in the colloidal liquid phase. The authors have reported a two dimensional hcp structure as the averaged local structure in a sufficiently dense colloidal liquid. This was evidenced by the fact that when both $|K|$ and $|q|$ are equal to the magnitude of K_{DS}, the maxima of C(K,q,0) on the first Debye-Sherrer ring exhibited six evenly spacing maxima as a function of the angle between K and q. Anticorrelations were observed between these maxima.

This work has been interpreted using an harmonic solid model (23). However the underlying lattice to which the particles are referenced is considered to be polycrystalline, and the orientation of a given crystalline is taken to be a random function of time in the liquid state. The assumption was made that the dynamics of this reorientation is slow enough not to interfere with local lattice vibrations. The crystal lattice is assumed to be large compared with the scattering volume. The vibration problem was treated the same as for an infinite two dimensional lattice. So the particle coordinates are separated into two parts, one part represents the reference of the particles to an underlying lattice which is orientationally averaged, while the other part represents deviation from the lattice sites which is assumed small and averaged over thermal fluctuations. Detailed calculations have been done for a two dimentional hexagonal close pack structure (3). The cross-correlation function, C(K,q,0) shows that the particles are highly correlated when $q = K = K_{DS}$ at azimuthal angular separations between K and q of 0°, 60°, 120°, 180° and anticorrelated at 30°, 90°, 150°, where the angle sweep was from 0° to 180°. The same type of results will be obtained for angles between 180° to 360°, which is just the mirror reflection of the former. A more general form of cross-correlation has been examined (4). Here the authors make a general expression of C(K,q,T) in equation (2.30), replacing the four sums by an integral over a four-point particle distribution function. This distribution function is reexpressed in terms of many particle correlation functions. The results make explicit the connection to several different cross correlation experiments performed in recent years.

Crossed-Beam Techniques

Crossed-beam Techniques, (CBT) are a very important experimental tools that are used to study both solids and liquids. This process can be thought of as the production and reading out of a holographic index of refraction grating in an optically non-linear medium. Here two laser "write" beams are crossed in a sample to produce a set of interference fringes which modify the optical properties of the sample. If a third "probe" beam has the same wavelength as the two inital write beams and propagates in the direction opposite one of them, then the "scattered" beam propagates back in the opposite direction of the other write beam. This scattered wave is termed the "phase conjugate" replica of the initial object beam because its wave fronts match those of the object beam exactly, except that the sign of the time appears reversed. This technique is also termed as degenerate four-wave mixing (1,24).

This technique has been used to study the non-linear optical scattering in nematic liquid crystals (25). Here the incident beams interface spatially to create an index modulation via their reorientation effects on the molecules. When aided by a dc magnetic field, the reorientation and nonlinear responses of the medium are enhanced and measurements of diffraction efficiency were done, as a function of the optical intensity, magnetic field and time. This technique has also been applied to absorbing media (such as solids and liquids) where local temperature variations form a phase grating which is probed by scattered light of different frequency (e.g. non-degenerate four-wave mixing). The diffusion of this thermal grating was also studied (26,27). Recently, degenerate four-wave mixing has been performed in alexandrite crystals ($BeAl_2O_3$:Cr^{3+}), where the decay rate of the excited state population grating were measured as a function of the beam-crossing angle (28). This technique is also used to the study the self diffusion of fluorescent particles (20). These fluorescent particles may be photobleached by a brief exposure to an intense laser beam to form fluorescent grating. This grating scatters light, but decays in time due to particle diffusion. Thus a recovery time can be measured. Finally, we mention that degenerate four-wave mixing experiments have been performed on colloid suspensions, (comprised of dielectric spheres suspended on water) where the dielectric spheres are drawn into the high intensity regions to form a grating, which in turn scatters light (1).

This thesis describes related crossed beams experiments for strongly interacting and essentially non-interacting particles, suspended in water. Here photophoretic or radiation pressure forces submicron plastic spheres into rows aligned along the light intensity interference fringes produced by crossed beams. The alignment of the particles can be detected by probing with a third laser beam which is scattered from the induced diffraction grating. Alternatively, the structural alignment may also be detected by self scattering of the incident laser beam. When the crossed laser beams are eliminated, the particles diffuse and the time decay of the diffracted probe beam light can be used to determine the collective diffusion constant of the particles. In the case of non-intercating particles the collective diffusion constant is equal to the self diffusion constant. Diffusion constants may also be measured by dynamic light scattering techniques (DLS). DLS monitors the decay of spontaneous density fluctuations and can be used to determined the collective diffusion coefficient, in general. Thus we see that CBT is a stimulated version of DLS.

Mathematical Description of Fringes Produced by Crossed (Gaussian Profile) Beams

Let us consider two infinite electromagnetic plane waves with electric fields $\bar{E}(1)$ and $\bar{E}(2)$ respectively, which intersect at angle 2θ as shown in figure 3. These two plane waves can be represented as

$$\bar{E}(1) = E(10)\exp\, i(\bar{k}1\cdot\bar{r} - wt + \phi1) \qquad (2.32a)$$

and

$$\bar{E}(2) = E(20)\exp\, i(\bar{k}2\cdot\bar{r} - wt + \phi2) \qquad (2.32b)$$

where k1 is the wave vector of plane wave 1

k2 is the wave vector of plane wave 2

$\phi1$ is the phase angle of plane wave 1

$\phi2$ is the phase angle of plane wave 2

E(10) is the amplitude of the electric field of the plane wave 1

E(20) is the amplitude of the electric field of the plane wave 2

$\bar{r}$ is the displacement

w is the angular frequency of the waves

and t is the time.

The time dependent part is suppressed hereafter, because we are interested in the intensity distributions for beams of equal frequency. The total electric field, $\bar{E}$ is the vector sum of the two fields

$$\bar{E} = \bar{E}(1) + \bar{E}(2). \qquad (2.33)$$

Furthermore, in practice, the plane wave will not have infinite lateral extent we will now assume the beam to have a gaussian beam profile. With these approximations we have

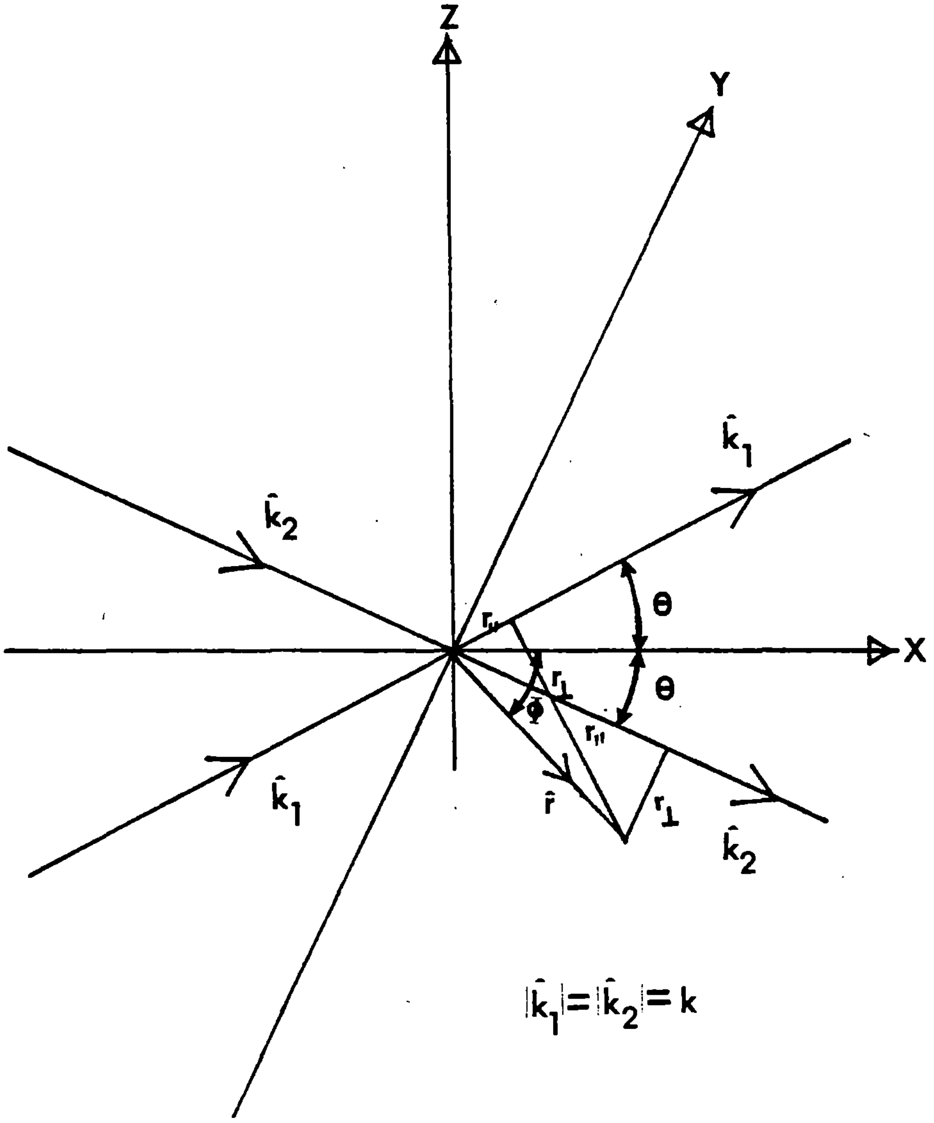

Figure 3. The Crossed-Beam Geometry

$$\bar{E}(1) = E(10)\ [\ \exp\ \{-ar^2\sin^2(\theta + \phi)\}]\ \times$$
$$[\ \exp\ i(\bar{k}1\cdot\bar{r} + \phi 1)] \qquad (2.34a)$$

and
$$\bar{E}(2) = E(20)\ [\ \exp\ \{-ar^2\sin^2(\theta - \phi)\}]\ \times$$
$$[\ \exp\ i(\bar{k}2\cdot\bar{r} + \phi 2)] \qquad (2.34b)$$

where $1/\sqrt{a}$ is the decay constant for the laser beam width

θ is the half angle of crossing

and ϕ is the direction of r.

The intensity distribution, I, for these two beams is directly proportional to the product of the total electric field and its complex conjugate, $\bar{E}^*\bar{E}$, i.e

$$I \propto \bar{E}^*\bar{E} \qquad (2.35)$$

where
$$\bar{E} = E(10)[\exp\{-ar^2\sin^2(\theta+\phi)\}][\exp\ i(\bar{k}1\cdot\bar{r} + \phi 1)] +$$
$$E(20)[\exp\{-ar^2\sin^2(\theta-\phi)\}][\exp\ i(\bar{k}2\cdot\bar{r} + \phi 2)].$$

Thus, the intensity distribution, I, is given by

$$I \propto \bar{E}^*\bar{E} = E(10)\ [\exp\{-2ar^2\sin^2(\theta+\phi)\}] +$$
$$E(20)\ [\exp\{-2ar^2\sin^2(\theta-\phi)\}] +$$
$$2E(10)E(20)[\exp\{-ar^2(\sin^2(\theta+\phi) +$$
$$\sin^2(\theta-\phi))\}]\cos\{2kr\sin(\theta)\sin(\phi)$$
$$+ \phi 1 + \phi 2\} \qquad (2.36)$$

where E(10) and E(20) are assumed to be real electric field amplitudes.

To simplify further analysis, we specify $\phi (= \pi/2)$ and assume that E(10) = E(20) = E(0) to find

$$\bar{E}^{*} \bar{E} = 2E(0)\ [\exp(-2ar^{2}\cos^{2}(\theta))] \times$$
$$[\ 1 + \cos(2kr\sin(\theta) + \phi 1 + \phi 2)] \qquad (2.37)$$

The last term on the right hand side can have the maximum value +1 and minimum value -1 depending on r for fixed Ø1 and Ø2. In fact the phase Ø1 and Ø2 only shift the intensity pattern with respect to origin, and can effectively be ignored. We can identify a length scale for the fringes such that

$$2kd\sin(\theta) = 2\pi$$

or $$2d\sin(\theta) = \lambda \qquad (2.38)$$

where d is the fringes separation

and λ is the incident laser beam wavelength.

Hence by knowing the crossing angle and the incident beam wavelength, the fringe spacing can be determined. Note that the intensity of the successive maxima are decreasing in amplitude from that of the central maxima because of the gaussian nature of the input beams. This is shown in figure 4 where z-axis represents intensity and x-y plane is the propagation plane. Here we assume that the diameter of the beam is 15 um, the decay constant is 1.8E10/um^{2}, the

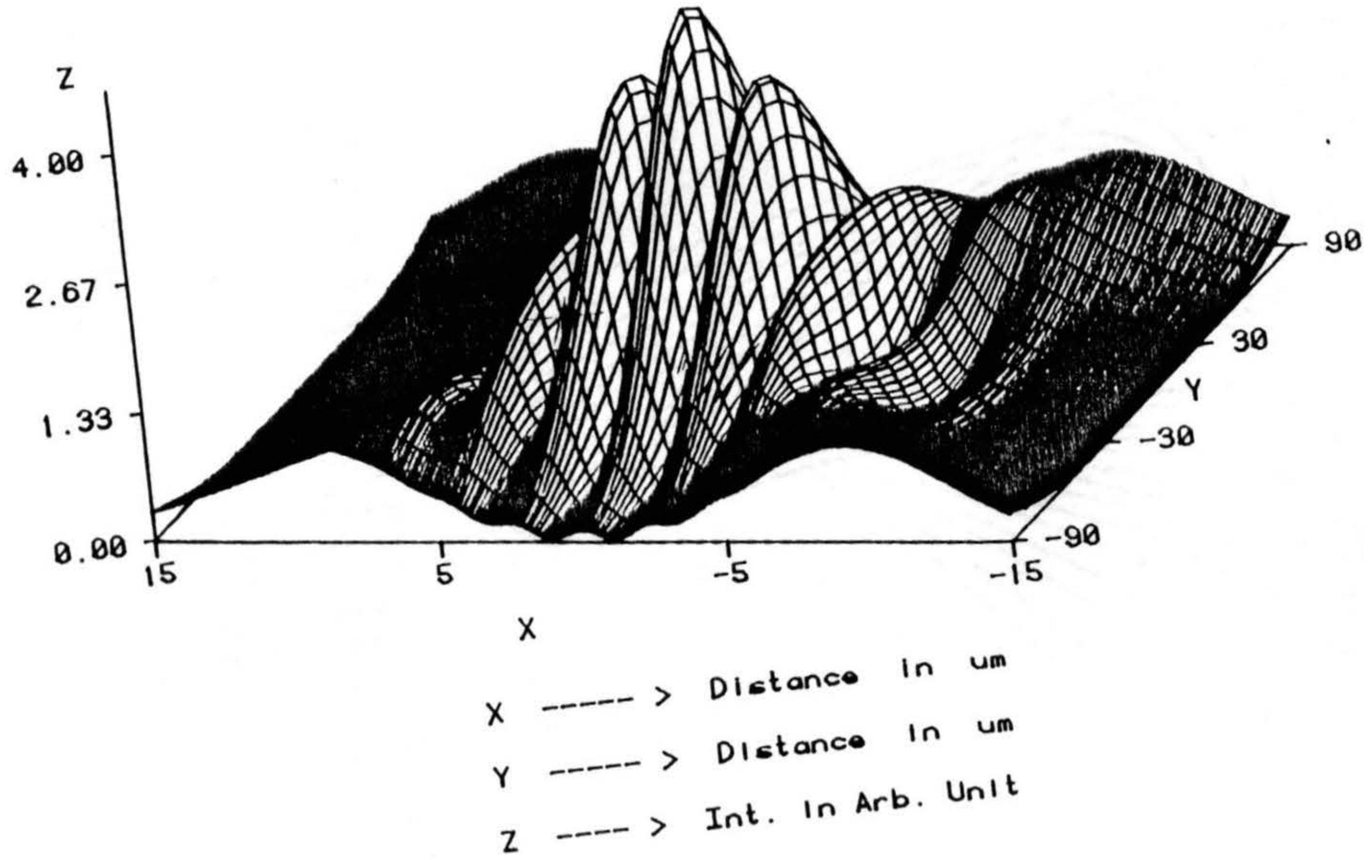

Figure 4. Intensity Distribution of Two Crossed Gaussian Beam Profile in the X-Y Plane

crossing angle is 12.6° degree and the wavelength is 0.488E-6 um. The two beams are propagating in x-y plane and crossing at the origin of the coordinates.

The Photophoretic or Radiation Pressure Forces

When a dielectric sphere is placed in a uniform electric field, it becomes polarized. The relation between the polarization, $\bar{P}$, and the electric field, $\bar{E}$, is given by (29)

$$\bar{P} = [3(\epsilon - 1)/4\pi(\epsilon + 2)]\ \bar{E}(0) \qquad (2.39)$$

where ϵ is the relative dielectric constant of the sphere to the medium.

If this dielectric sphere is illuminated by a linearly polarized plane wave of radiation then it will be polarized in the electromagnetic field due to the displacement of the electrons with respect to the nuclei and also due to the partial orientation of any permanent electric dipoles that may be present. Because the incident field oscillates harmonically, then to a close approximation the induced polarization will follow synchronously as follows

$$\bar{P}\ \exp(iwt) = [3(\epsilon - 1)/(4\pi(\epsilon + 2)] \times \bar{E}(0)\ \exp(iwt) \qquad (2.40)$$

where w is the angular frequency of oscillation.

The resulting electric dipole moment of a dielectric sphere in the presence of an electric field is given (29)

$$p = [(\epsilon - 1)/(\epsilon + 2)]\ a^3\ E(0) \qquad (2.41)$$

where a is the radius of the dielectric sphere.

Furthermore, equation (2.41) can be written in terms of the refractive index of the dielectric sphere, n_a and refractive index of sourrounding, n_s as follows

$$\begin{aligned} p &= n_s^2\ [(n^2 - 1)/(n^2 + 2)]\ a^3\ E(0) \\ &= \alpha\, E(0) \qquad (2.42) \end{aligned}$$

where n is the ratio of index of refraction of sphere, n_a to sourrounding, n_s .

In the presence of this radiation field, forces are exerted on a neutral dipole (the polarized sphere). In a dilute medium this 'ponderomotive' force is simply the Lorentz force (30)

$$\bar{F}(\text{grad}) = (\bar{p}\cdot\bar{\nabla})\ \bar{E} + (1/c)(\partial\bar{p}/\partial t) \times \bar{B} \qquad (2.43)$$

where $\bar{B}$ is the magnetic field induction

and $\bar{F}$(grad) is the force on the sphere.

Furthermore, if we assume $\bar{p} = \alpha\,\bar{E}$ as above in equation (2.43), the first term on the right hand side can be written as

$$(\bar{p}\cdot\bar{\nabla})\,\bar{E} = \alpha\,(\bar{E}\cdot\bar{\nabla})\,\bar{E}$$
$$= \alpha\,[(1/2)\bar{\nabla}E^2 - \bar{E}\times \mathrm{curl}\ \bar{E}]. \qquad (2.44)$$

Then using Maxwell's equation

$$\mathrm{curl}\ \bar{E} + (1/c)(\partial\bar{B}/\partial t) = 0 \qquad (2.45)$$

and the equation (2.44), equation (2.43) can be written as

$$\bar{F}(\mathrm{grad}) = \alpha[(1/2)\bar{\nabla}E^2 + (1/c)\,\partial(\bar{E}\times\bar{B})/\partial t]. \quad (2.46)$$

The first term of the right hand side of the equation (2.46) shows that the dielectric spheres are moved towards the high intensity regions of the incident radiation, when the dielectric constant of the spheres is larger than the surrounding medium. On the other hand, if the dielectric constant of the spheres are smaller than the surrounding, then the spheres would be moved out of the high intensity regions. The second term involving the Poynting vector is responsible for moving the dielectric spheres in the direction of the beam propagation. This is true for all cases; but when the dielectric spheres are not transperent, then radiomatric force may dominate. This can cause the spheres to move in the opposite direction of propagating beams.

Micron size particles have been accelerated and trapped in stable optical potential wells using only the force of radiation pressure from a continuous laser (31). A.Ashkin (32) shows this effect on a dielectric sphere, where a sphere is drawn into the high intensity region of focussed light radiation. A single vertically directed focussed TEMoo-mode cw laser beam of approximately 250 mW is sufficient to move and ultimately support stably a 20 um glass sphere (33). The restoring force on the sphere due to gravity is balance by the radiation pressure. There exsits two distinct stable regimes of levitation for solid spheres, one located above the focus, the other below it (34). A sphere can switch back and forth between these positions.

In our own preliminary experiments a laser beam of wavelength (488 nm) was focused to an area of 15 nm in a sample cell of thickness ~ 70 um and containing a dilute suspension of 1 um diameter spheres at a density of 10E10 particles/c.c. The particles are moved into the high intensity region and pushed in the direction of propagation. As a result of this radiation pressure, these particles are pushed against the downstream wall. The self diffracted intensity maxima were observed as shown in figure 5a. This diffraction pattern is a two dimensional hexagonal structure. The scattering angle from this first neighbour intensity maxima O(10) or O(01) measured with respect to the incident 'beam, was 24 degrees and the second neighbour intensity maxima O(11) was 43 degrees. Using the Bragg's law for two dimensional hexagonal close pack structure,

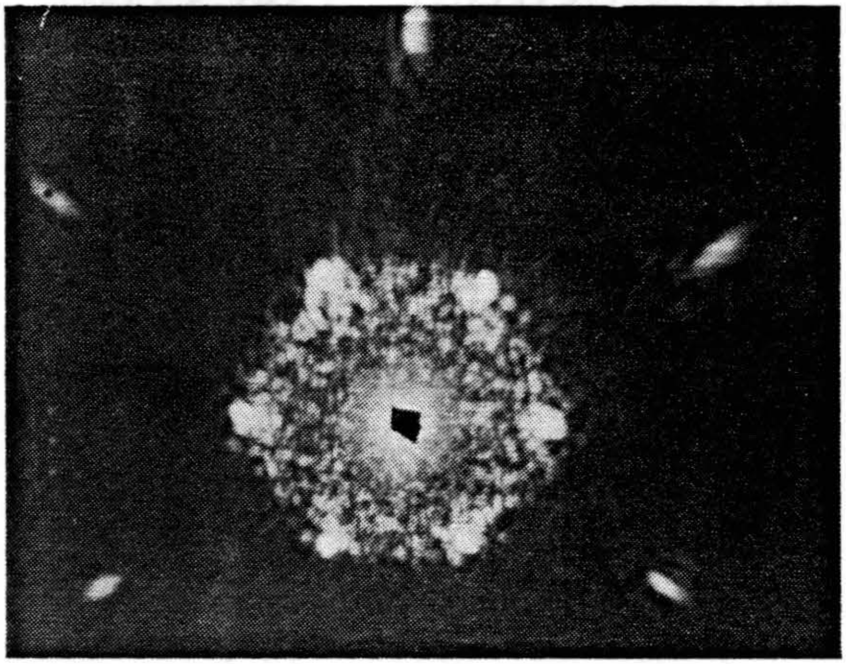

Figure 5a. Bragg's Spots Produced by Scattering from a Close Packed Structure Trapped by a Single Focused Laser Beam

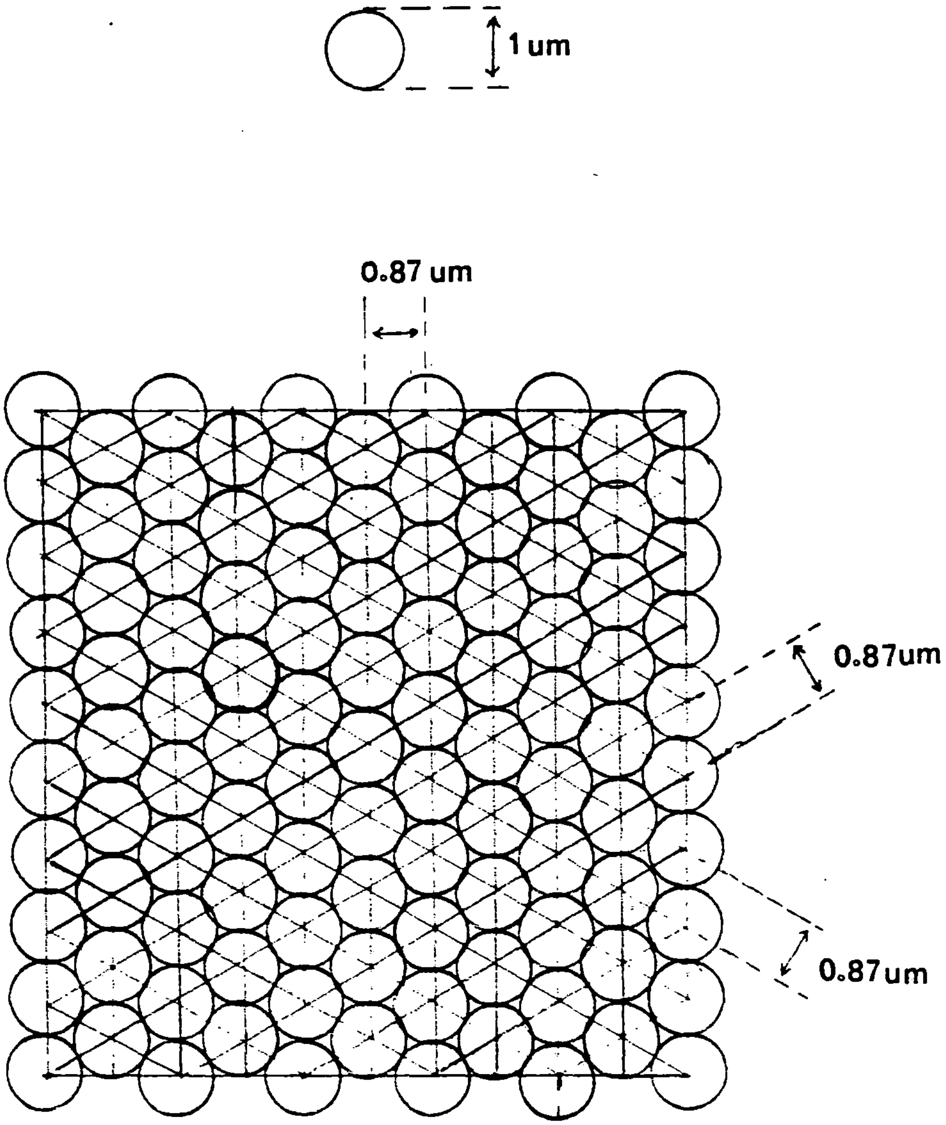

Figure 5b. Two Dimensional Hexagonal Close Packed Structure

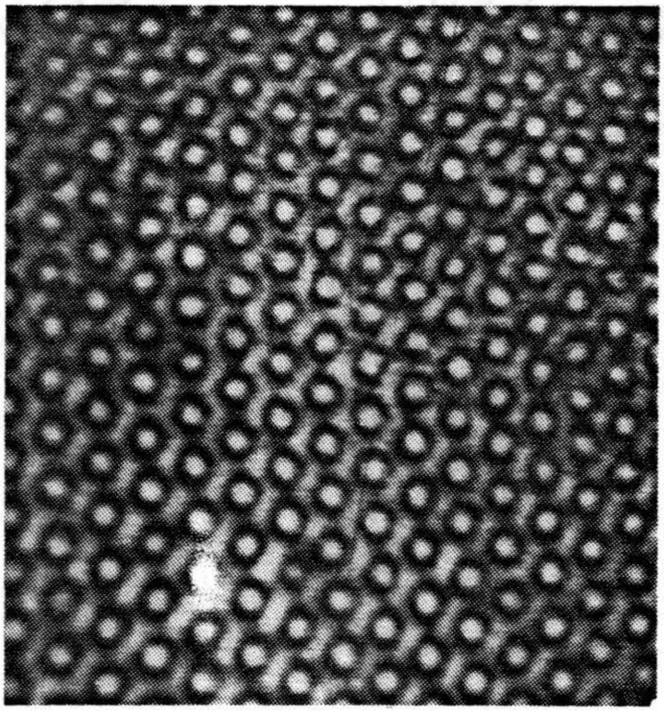

Figure 5c. Real Space Structure in a Sample Compressed by Radiation Pressure.

$((1/d(hk))^2 = (4/3a^2)(h^2 + hk + k^2)$, where d(hK) is the plane separation and a is the lattice constant), the real space configaration was reconstructed as shown in figure 5b. A microscopic objective was used to image the real space structure picture as shown in figure 5c. These two pictures give the same structure with the same dimensions.

The effect of both the first term and second term of equation (2.46) is demonstrated in the above experiment. Note that if the dielectric spheres are not transparent then radiometric force dominate over radiation force. This may cause the dielectric sphere move opposite to the propagation of the beam but they will also be moved in the high intensity regions(33).

Radiation Pressure for Finite Size Particles

The effect of an field gradient on dielectric spheres has been discussed in the pervious section with the implicit assumption that the particles are small in dimension compared to the variation in the field gradient. In our experiments the particle size and field gradient variation can be of the same order of magnitude. Thus we need to consider the effect of the field gradient variations within a single particle.

If we are interested in the lateral force (force perpendicular to the direction of propagation) produced on the particles in a radiation field, then we focus our attention on the first term in the equation (2.46). Here 0

$= -\alpha E^2/2$ acts like a potential whose negative gradient produces the force of interest. In a crossed beams experiment, the fringes will produce a spatially periodic potential which is purely harmonic for infinite beam widths.

Let us assume a sphere of radius a is subjected to the potential produced by the fields in equation (2.37) in the limit $a \rightarrow 0$, $\emptyset_1 = \emptyset_2 = 0$, and $q = 2k\sin(\theta)$. The force exerted on the sphere is dependent on the intensity potential averaged over the whole sphere. The average intensity potential, U(avg) is given by

$$U(avg) = (1/V)A \int_V [1 + \cos(\bar{q}\cdot\bar{r})]\, d^3\bar{r}' \qquad (2.47)$$

where A is a constant (a fuction of the magnitude of the intensity, the diameter of sphere and the dielectric constant of the sphere as well as the medium)

$\bar{q}$ has the direction of the periodicity of the potential (and magnitude $q = 2\pi/d$, where d is the width of the intensity potential)

$\bar{r}$ is the distance of the sphere from the origin

and V is the volume of the sphere.

The integration is carried out over the volume of the sphere. Let us assume that the sphere is at distance, b from the origin and the direction of b is parallel to q, as shown in figure 6. The equation (2.47) is then written as

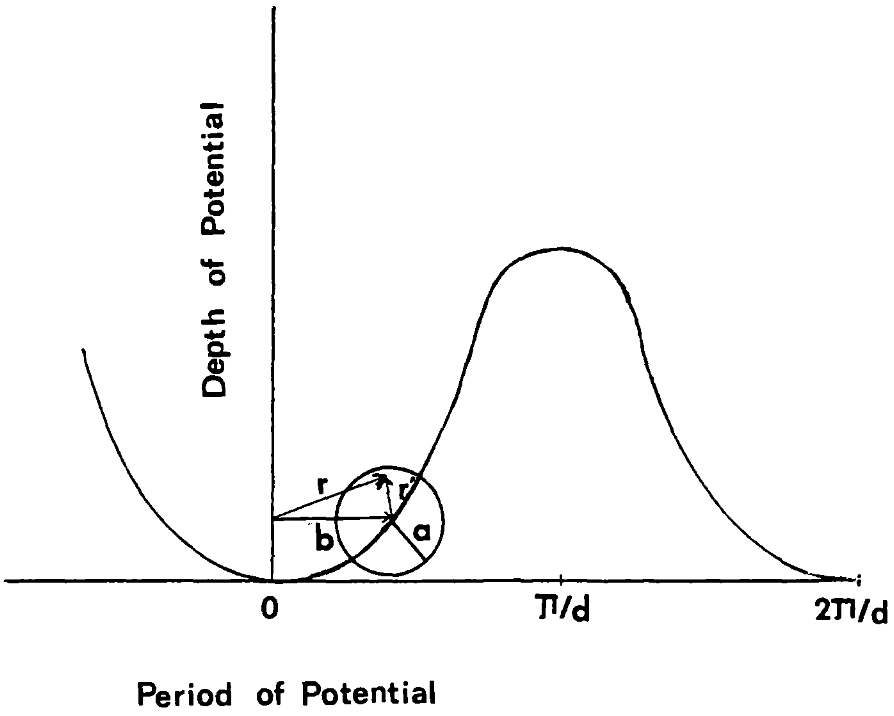

Figure 6. Finite Sized Dielectric Sphere in a Periodic Intensity Potential

$$U(avg) = (2\pi/V)A \int_0^a r' \, dr' \int_0^\pi \sin(\theta) \, d\theta \, [1 + \cos(qb + qr'\cos(\theta))] \qquad (2.48)$$

This integration is straightforward, and the result is given by

$$U(avg) = A \, [1 + (3\cos(qb)/qa) \, j_1(qa)] \qquad (2.49)$$

where $j_1(qa)$ is the 1st order spherical Bessel function.

Let the sphere be placed at the origin (b = 0). Assuming a point particle ($a/d \rightarrow 0$), the average potential on the sphere is maximum (U(avg) = 2A). On the other hand, as the radius of the sphere compare to fringes spacing increases ($a/d \rightarrow \infty$) the average potential decreases to zero. When the sphere is displaced from the origin such that b = 2d, then in the limit of point particles, the average potential is zero. As (a/d) increases the average potential oscillates and decreases to a constant. One sees that in the limiting case that ($a/d \rightarrow \infty$), the potential goes to zero. The average potential is constant. This means that the force on the sphere is zero.

Comparison of CCIFS and CBT

CCIFS is a technique which monitors the local order in fluid systems by cross correlating light scattered to two spatially separated detectors. Due to interactions, local density modes will be coupled and scatter light preferentially with certain symmetries. A minimun of two detectors may be used to measure these correlated density modes. In CBT a single density mode is directly stimulated in the fluid, and scattering will produce diffraction pattern from the stimulated mode, as well as, other modes slaved to it. Thus in both techniques, the (local) coupling of fluid density modes is being monitored. In this section we explore the connection between CCIFS and CBT. Recall that the equal time equilibrium CCIFS scattered intensity distribution was given in equation (2.30) and can be written as

$$C(k,q,0) = [(\int \sum_{ij} \sum_{lm} \epsilon_i \epsilon_j \epsilon_l \epsilon_m \exp[i\bar{k}\cdot(\bar{r}_i - \bar{r}_j) + i\bar{q}\cdot(\bar{r}_l - \bar{r}_m) - \Psi/KT] \, d(r))/Z]/[S(k)S(q)] \tag{2.50}$$

and re-expressed as

$$C(k,q,0) = (S(k)S(q)[1 + \delta_{k\pm q}] + C_4(k,q))/S(k)S(q) \tag{2.51}$$

where $C_4(k,q)$ is a nongaussain factor including four particle correlation functions. This term becomes negligiblly small compare to the denominator for large scattering volumes.

$$S(k) = \int \sum_{ij} \exp(i\bar{k}\cdot(\bar{r}_i - \bar{r}_j) - \Psi/KT\} \, d(r)/z \qquad (2.52)$$

is the apertured static structure factor

and $$z = \int \exp(-\Psi/KT) \, d(r), \qquad (2.53)$$

is the partition function. The scattered intensities are represented in terms of the first Born approximation and averaged over an equilibrium distribution of particles subjected to mutual interaction potential, Ψ .

The CBT scattered intensity distribution may be written as

$$\langle I(k)\rangle = \{\int \sum_{ij} \exp(i\bar{k}\cdot(\bar{r}_i - \bar{r}_j) - (\Phi + \Psi)/KT) \, d(r)\}/\{ \exp(-(\Phi + \Psi)) \, d(r)\} \qquad (2.54)$$

where the first Born approximation is again used to represented the scattered intensity with scattered amplitude $\epsilon(r_i) = 1$ (infinite scattering volume). The scattered intensity is averaged over an equilibrium distribution of particles with interacting potential, Ψ , and external potential, Φ , where Φ is given by

$$\Phi = A \cos(\bar{q}.\bar{r}). \qquad (2.55)$$

A is the amplitude of the external potential (dependent on input power) and q is wave vector of the periodic potential.

Furthermore, the scattered intensity in the expression (2.54) assumes a single probe beam scattered from the sample, and the self-scattered beams are filtered out.

By expanding equation (2.53) in a power series in A, the amplitude of the external potential, a formal relation between CCIFS and CBT can be demonstrated (35). The terms linear in A are zero due to the translational symmetry of the liquid state. The quadratic terms in A involve particle correlation functions averaged over the same phase factors as in CCIFS. Taking into account the expansion of denominator of equation (2.53) in A, as well, we have

$$\langle I(K)\rangle = S(K) + (A/KT)^2 [S(K)S(q)\delta_{K\pm q} + C_4(K,q)] + O(A^3) \qquad (2.56)$$

where S(K) and $C_4(K,q)$ are defined as before. The scattering volume size is unrestricted here and $C_4(K,q)$ is no longer dominated by Gaussain terms as the scattering volume becomes large.

From the above expression we see the similarity between these two techniques. The advantage of CBT is that there are no aperture functions modulating the influence of multiparticle correlation functions on the calculated scattering ($\epsilon(r) = 1$). On the other hand, extreme care must be taken in order to collect the data. This CBT techinique suggests a new way to investigate multiparticle correlation functions, as well as, the solid liquid phase transition.

Commensurate and Incommensurate Phase in Two Dimensional Systems

For a long time it was believed that two dimensional solids could not exist. The classical two-dimensional harmonic soilds cannot have long range order (36,37). However, the absorption of rare-gas monolayers on graphite have interesting properties (38). As the temperature and pressure of the rare-gas is varied, these systems exhibit a large variety of phases. At high temperature and low density the monolayers form a two-dimensional (2-D) fluid like phase. At low temperature, as well as, low pressure they exhibit a 2-D crystal-like phase which register on the underlying lattice (39). This fluid-solid structure bears some resemblance to our problem of looking at a two dimensional colloidal liquid in the presence of a periodic external field.

The monolayer problem may be studied theoretically by considering an array of spheres connected with springs and having an average spacing a (spatial period $2\pi/a$). When these systems are subjected to a external periodic potential of spatial period, $2\pi/d$, then depending on the strength of the external periodic potential, this harmonic structure undergoes phase change like the absorped atoms on the graphite substrate (39,40). If the external potential is weak (or absent) the harmonic term would favour a lattice constant a which is in general incommensurable with potential spacing, d. This is in general termed the incommensurate phase (IC) and represented in figure 7a. In this case diffraction spots would not coincide with the Bragg spots of the periodic potential. However, if the external potential is strong enough, it may be favourable for the lattice to relax into the external periodic potential, where the average spacing, a, is simply rational fraction of the period, d. This is termed as commemsurate phase (C) and is shown in figure 7b. The diffraction pattern for this case coincides with the potential. However, these two phases (C & IC) do not exhaust the stable configurations (40). If the potential is not strong enough to force the particles into a commensurate phase, the particles will move towards the minima of the potential. The average period may approach a simple commensurate value but remain incommensurate. This gives rise to a additional chaotic structure as shown in figure 7c. The diffraction pattern does not have well defined Bragg spots. For instance, if the potential is very strong compared to the interaction potential, then clearly there exists a metastable state where the atoms are distributed randomly among the potential minima. This is also termed a chaotic phase. Later in the Chapter V we will find it useful to use similar terminology in analying our data.

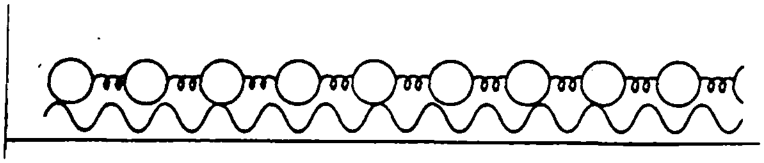

Figure 7a. Incommensurate Phase

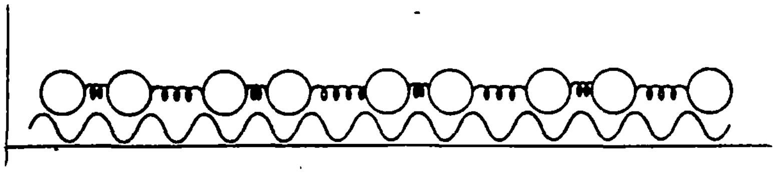

Figure 7b. Commensurate Phase

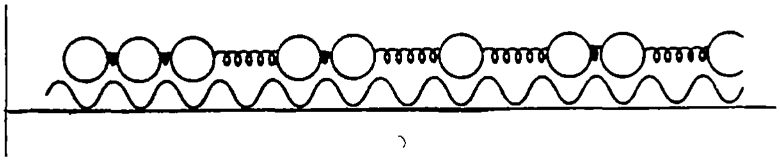

Figure 7c. Chaotic Phase

CHAPTER III

EXPERIMENTAL BACKGROUND

Introduction

This chapter gives details of the experimental techniques used. The general experimental design is given, with details of cell design, sample preparation, and data collection techniques.

Experimental Details

The basic CBT experimental set-up is straightforward. It consists of the following items: two beam splitters, two front surface reflecting mirrors, one right angle prism with orthogonal sides having a reflecting coating, one lens, two pin diodes, amplifers, A/D converter, digital oscilloscope, analog oscilloscope, apple IIe computer, sample cell, screen, optical bench, chopper, He-Ne laser and/or an argon ion laser.

The two crossed beams are produced from the main laser beam by using a coated optically flat beam splitter as shown in figure 8. The intensity ratio of transmitted to reflected beam was 40/60 and the angle between transmitted beam and reflected beam was made 90 degrees (for maximum efficiency). The two mirrors were placed about 30cm from the beam

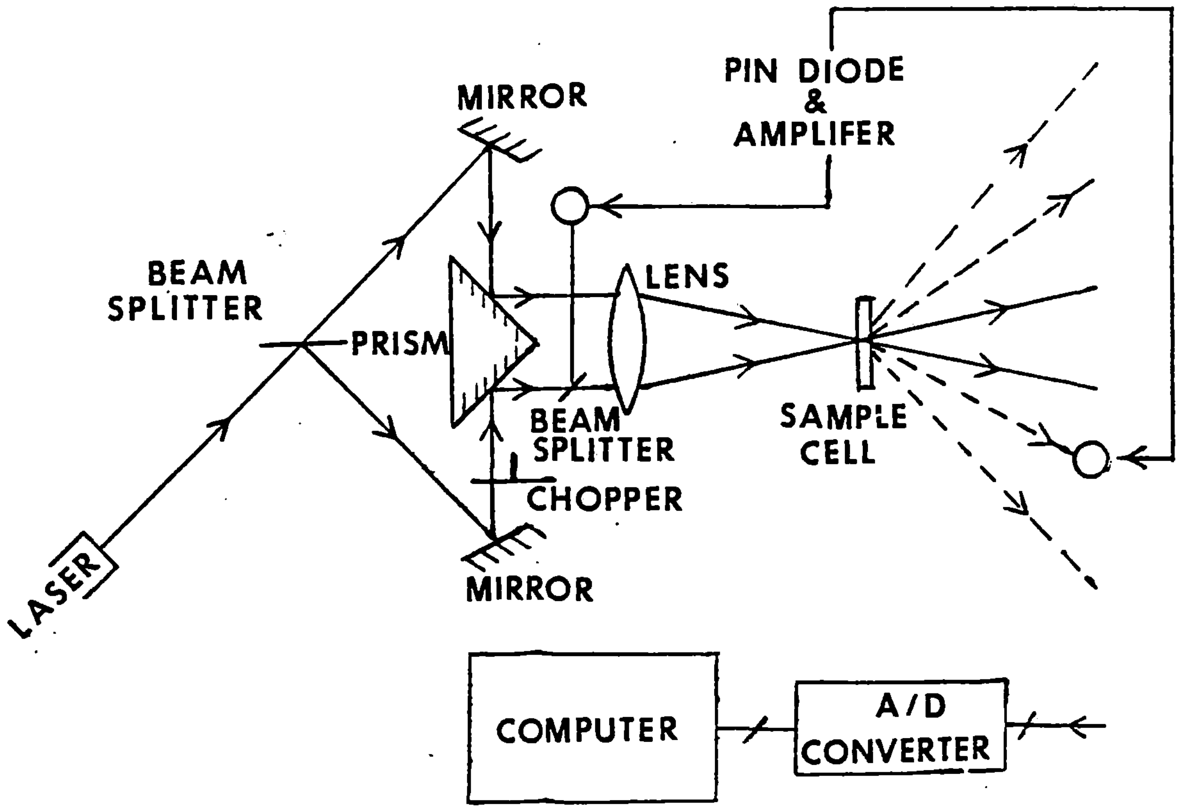

Figure 8. Experimental Setup

splitter to direct each beam onto a prism shaped mirror. The prism was mounted on moveable table which is placed symmetrically with respect to the two mirrors. The optical path length of these two beams were made approximately equal and within the coherence length of the laser. These two laser beams upon reflecting from the prism propagated parallel to one another in the same plane with the main beam. The beam separation of the two parallel beams could be controlled by translating the prism table. This adjustment changed the crossing angle of the beams by making use of the double convex lens. In this way the angle could be varied in the sample from $\theta = 1^{\circ}$ degree to $\theta = 30^{\circ}$ degree assuming that the index of refraction of the sample is 1.33. The higher intensity beam was attenuated by introducing another beam splitter with transmission to reflection ratio 1/3:2/3. The reflected beam is used for triggering, while the transmitted beam (propagating parallel to the other beam) now has equal intensity with the other beam. One pin diode was positioned to detect the reflected beam. The photocurrent was amplified by a 741 operational amplifier using the simple circuit shown in figure 9. The signal is then fed to the triggering channel of the a/d converter. A lens of approximately 11cm focal length was used to focus the beam in the sample. The scattered intensity at a given scattering angle was picked up by the second pin diode. This pin diode converted the light signal to electrical signal and amplified it as described previously. This electrical signal was then fed to

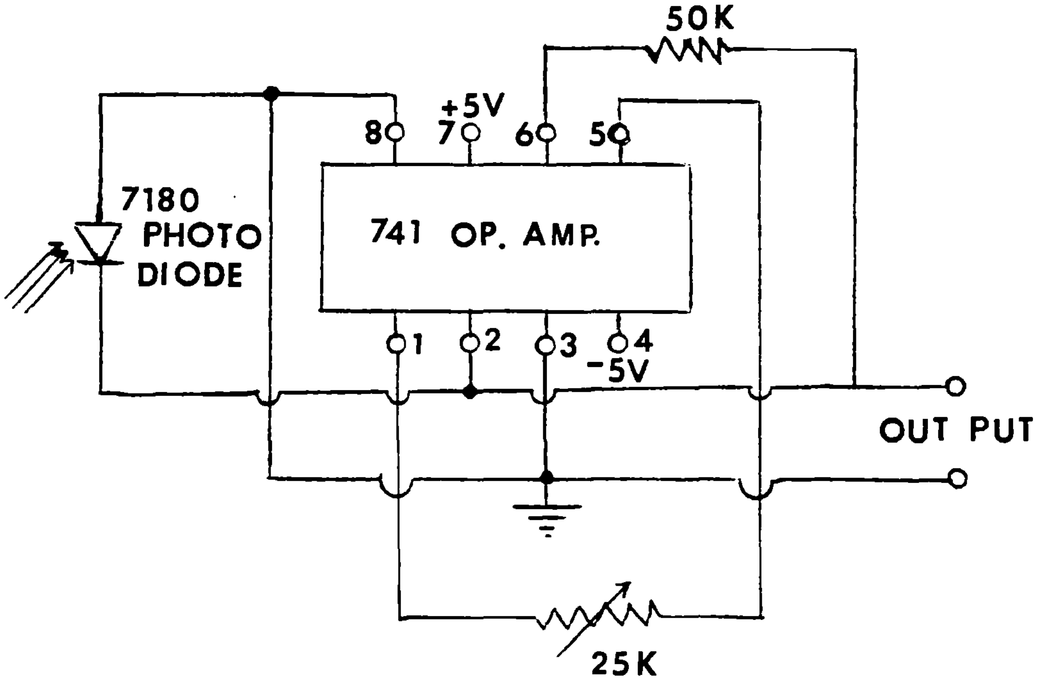

Figure 9. Circuit Diagram of Pin Diode and Operational Amplifiers

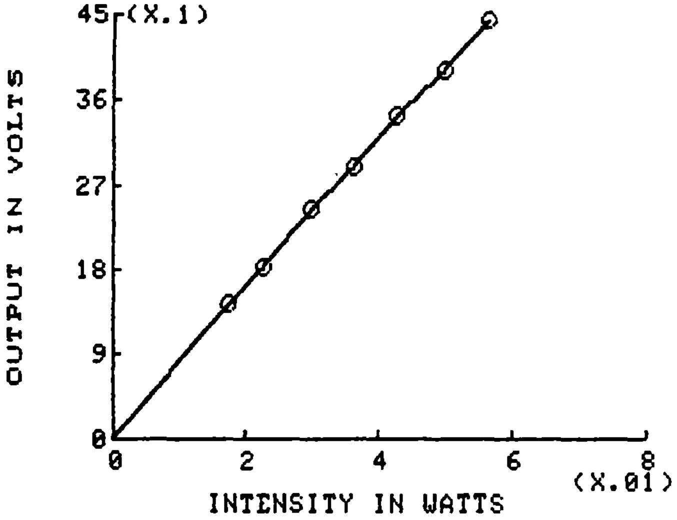

Figure 10. Plot of Amplifier's Output Voltage vs Input Intensity

another channel of the a/d converter for data collection. The output signals could also be fed to an analog oscilloscope to observe the signal. The output of the a/d converter or digital oscilloscope was connected to the apple IIe computer. A chopper was used to eliminate the crossed beams and the chopping rate was controlled by a variac. This chopper has a circular blade which was attached to a motor. When the triggering beam was eliminated, a triggering signal was generated. A linear relationship between intensity and amplified voltage was observed (as shown in figure 10.).

Cell Design

The sample cell consists of the following items: three quartz plates, a metal cell holder and an O-ring. The dimensions of two of the quartz plates are 1in diameter and 1/8in thickness. The other quartz plate has thickness of 1/8in and is 1/4in in diameter. This design is shown in figure 11. The small quartz plate is glued to one of the other larger quartz plates using epoxy. This is then placed inside one of the cell holder cavities. The other cavity holds the opposite quartz plate which is separated from the first by means of a silicon rubber O-ring. The gap between the plates is varied by adjusting the screw tension. To assemble the cell, an O-ring is placed on the top of double plate in this cell housing cavity. The other plate was placed on top of the O-ring to form a seal, protecting effectively against evaporation. The other cell holder wall

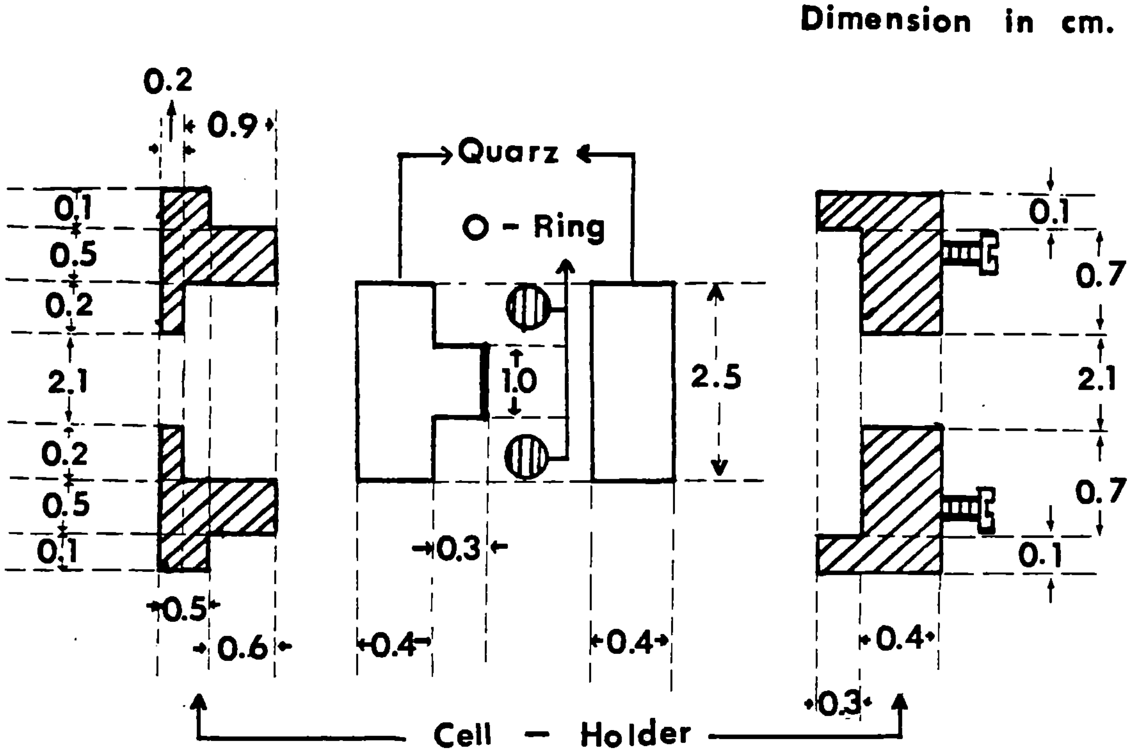

Cell Design

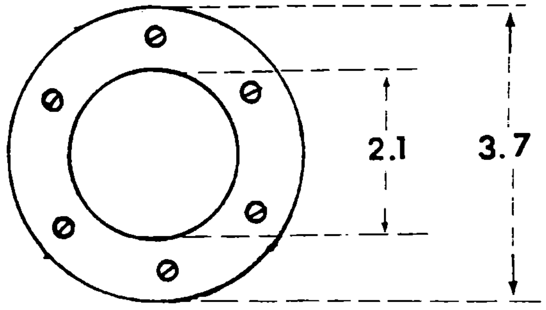

Front View

Figure 11. Thin Film Cell

was then placed on the top of the quartz plate and tightened by means of screws. Thus the sample is in contact with only the quartz plates and O-ring.

Spacing Measurement

The spacing between the two quartz plate cell walls was measured in the following ways: first by using a microscope and then by an interference technique. A rough measurement of the gap was measured by focussing a low power microscope at the bottom and top surface of the plates of the cell. The uncertainty in the gap measurement is estimated at about 20%. However, some parts of this experiment needed very accurate gap measurements (i.e. an uncertainty within 1%). Thus we utilized an interference method described by Hurd (5).

Here a collimated laser beam enters a parallel plate cell at an angle θi as shown in figure 12. Before injecting the sample in the cell, the gap is filled with air. Therefore, the refractive index is same as outside the cell and there is strong scattering at the gap interface. A reflection occurs at every interface, but only the reflections from the interface adjacent to the thin air film proved to be important. Interference in the beams reflected from either side of the interface will depend on the spacing L.

Consider figure 12. the phase of ray 1 at A and of ray 2 at C are the same. The optical path length difference

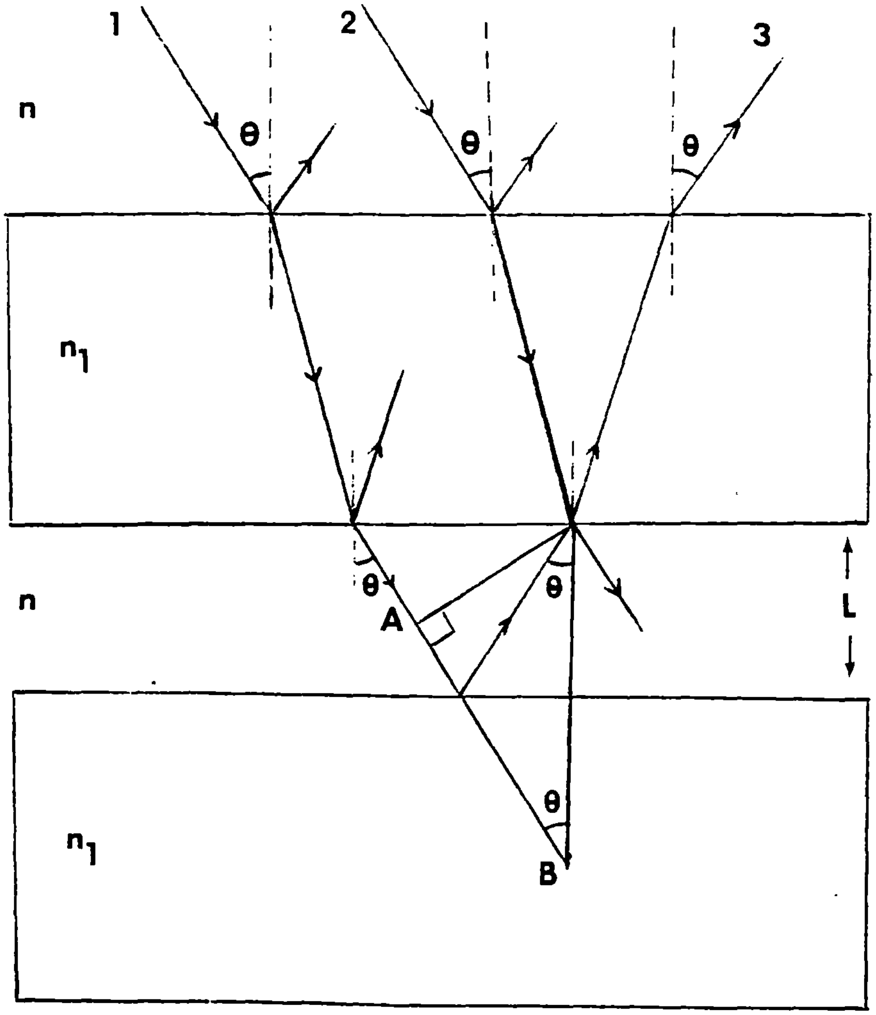

Figure 12. Spacing Measurement

between ray 1 and ray 2 is simply nAB where n is the refractive index of the thin film (n = 1, for air). This path difference between ray 1 and ray 2 may be expressed as 2Lcos(θi). If n > n1 (the refractive index of the cell wall) an extra factor $\lambda/2$ is to be added to the path difference because of the phase change an reflection. Keeping in mind that ray 1 and ray 2 are not separate beams but selected rays within the incident beams, and ray 3 is only one of the entire number of reflected beams. The problem is to determine the order of the interference.

Destructive interference, that is, a darkened ray 3, occurs when the path difference is a half-odd integer number of the wavelength. Hence the order "m" is given by

$$m = [2L \cos(\theta i)] / \lambda \qquad (3.1)$$

where λ is the incident radiation wavelength.

Now suppose the cell is rotated so that θi increases. The path length difference will decrease and destructive interference will occur until θi has increased enough that the next lower order of interference is found. At this point a fringe will again darken ray 3 so that the condition is immediately identifiable. Knowing the two angles, θi and θf, at which sequencial order numbers are found allows one to solve for L from equation (3.1) and identical equation for m - 1.

Accuracy and precision can be increased by passing over a number of fringes before reading θf. The number of fringes passed over is given by

$$\Delta m = [2L/\lambda]\{\cos(\theta i) - \cos(\theta f)\} \qquad (3.2)$$

which gives gap L is

$$L = (\Delta m\lambda) / [2\{\cos(\theta i) - \cos(\theta f)\}]. \qquad (3.3)$$

In most situations the limitation on the precision is the uncertaintie in the angle. When that uncertainty of the gap is .1 um, the relative error in L is 1%; thus a 5 um spacing can be measured to within 50 A uncertainty. Another important limitation is in the measurement of spacing below 1 um where different laser lines must be used to see any interference at all for the accessible incident angles.

Cell Cleaning

The walls of the sample containers constantly contribute to the ionic impurities by the leaching out of charged ions. At least one quantitative study has been done (41) on this problem and some suggestions made for eliminating it. In this study, the following procedure was adopted to clean sample containers:

1. Washing sample containers and cells vigorously with a soap and a brush.
2. Boiling in deionized water with Micro for 1 hour.

3. Rinsing in deionized water, then re-boiling in deionized water. Repeating process several times.
4. Final rinse was done using water deionized and filtered in a Barnstead system (18 mega-ohms resistivity).
5. Handling with tongs and storing in a clean dry place.
6. Keeping parts covered until use.

Actually, there is little hard evidence that leaching is indeed a problem, but the circumstantial evidence is convincing enough to use care in cell preparation.

Sample Preparations

The two clean quartz plates are put together inside the cell container with an O-ring between them and mixed bed resin (Analytical grade mixed bed resin AG 501-X8(D) 20-50 mesh, fully regenerated, Bio-Rad Laboratories) inside the cell. A wedge shaped gap can be produced by drawing one side of this cell tighter than the other. It is this wall separation gradient that will allow us to get a monolayer of particles.

When the latex has been placed in cells with ion exchange resin, it is advisable to mix them mechanically for a few hours to speed the deionization process. However, violent or prolonged mixing is contraindicated by a "scum" of particles that forms at any air-water interface. This air may contain carbon dioxide which can be dissolved and may contribute to the impurities problems. We avoided this problem by filling the cell completely with water. An effective way to handle clean latex without opening the container is via plastic tubing with syringe tapers on its ends. Latex can be removed from a vial using the soft plastic top or quartz tube and loaded in a syringe needle, then the sample cells can be loaded by injecting through the O-ring cell in the same way. If the cell is filled completely, air contact will be minimal. The problem is now with aggregation of latex, but the percent of aggregation is very small compared to the rest of the sample. This sample is then placed in a quiet place with no thermal gradients that might cause convection. Within a few hours one generally finds nice liquid and crystalline structures which can be detected by illuminating with laser light. Some samples will simply never crystallize. Others phase separate showing liquid and crystalline regions. When it becomes necessary to transport them, we try to do so with the least amount of agitation possible.

A/D Converter

We used two different A/D converters to collect data in our experiments. The first A/D converter used for this experiment is the AI13 analog input system data acquisition module (Interactive Structure Inc.). The AI13 analog input system is a high-performance 12-bit data acquisition system for Apple IIe computer. It plugs directly into one of the

Apple expansion slots and gives the Apple the ability to make precision voltage measurements. Any instrument or sensor producing an electrical signal becomes an Apple IIe input device. Software selects the input range, and sensor output range from +- 5 Volts to 0-100 milliVolts can be accomodated with 12-bit accuracy.

The AI13 analog system has 16 input channels. The channel selection and range are a single store operation, which are then read in 2 bytes directly from the AI13. Software is in complete control of both order and speed with which the channels are read. The analog conversions can be started by a varity of signals including an external trigger pulse.

AI13 fully supports high-performance programming techniques, such as high speed Assembly language sampling. The selection and sampling time of each channel is 6 microseconds, hold and conversion time is 13 microseconds, total conversion time is 20 microseconds and sampling aperture is 125 nanoseconds.

Digital Memory Oscilloscope

The Model 85 aScope Digital Oscilloscape (Northwest Instrument Systems, Inc.) is a dual-channel, fully programble, digital memory oscilloscope. It is designed to work with an Apple II, Apple II+, or Apple IIe computer. The Apple computer must have a Disk II, display, 48k of memory and the DOS 3.3 operating system. The model 85 aScope is controlled by the Apple through programs. In any case, once the operating software is loaded and one or two probes are attached to the back of the Apple, we have a working DC-to-50 MHz digital oscilloscope.

The analog information is received by the probes and is sampled very rapidly, digitized and turned into binary data. The model 85 aScope can average successive frames of a waveform to remove random noise and will store the entire data to the disk. The software then converts and displays a waveform on the Apple monitor.

Data collection

All of our measurements involve measuring the intensity of scattered light, either as a function of input laser power, or of time, or of beam crossing angles. However, the intensity of the signals fluctuate in time, which complicates the data collection process. For these reasons, two different procedures are used for data collection. One of them is for static or average intensity data collection and other one is for dynamic or time dependent data collection. The static procedure basically uses the A/D converters as a digital voltmeter. The dynamic procedues utilizes the digital scope or A/D converter to signal average time sweeps.

A statistical method is used to get a continuous reading of the average intensity for static measurements. We defined the weighted average, S, by:

$$S = \sum_n w^n \; D(n) / \sum_n w^n \qquad (3.4)$$

$$= \sum_n w^n (1 - w) \; D(n) \qquad (3.5)$$

where D(n) is the nth data sample measurement relative to the present time interval. D(0) is the current data, D(1) is the data taken before D(0), D(2) is the data taken before D(1), D(3) is the data taken before D(2) and D(n) is the data taken before D(n-1) data. Equation (3.4) is the same as standard average when the weight factor, w is unity. In practice, however, the weight factor was chosen be to less than unity and greater than zero in order to weight the present reading the most. This allowed us to have running average with minimized fluctuations and yet would reveal any systematic drifts in the signal. The value S is then dispalyed on the monitor or printer which worked as a digital voltmeter.

The fluctuations in the signal are estimated by the following running average:

$$s = [(1-w)\{\sum_n w^n D(n)^2 - (\sum_n w^n D(n))^2 (1-w)\}] \qquad (3.6)$$

This number is also displayed on the monitor or printer. When the fluctuation in the signal is small, this calcualted fluctuation is also small. The basic program for calculating these averages is given in appendix (C).

In the case of the dynamic data collection, a totally different method is used. Here two types of devices were used, one was the 16 channel AI13 A/D converter and the other one was the digital memory oscilloscope.

In the first case one of the channels of the A/D converters is selected for triggering and another is utilized for data collection. This triggering was implemented by means of software and is based on the input to the triggering channel. When a signal derived from the beam chopper drives the triggering channel low (or high depending on experiment), then the program was allowed to collect data. This data collection is done utilizing an assembly language program supplied by the manufacturers of the A/D converter. This program fills up a Basic array with data, when called, and the time interval between the data points is controlled by software. The intensity versus time data are then signal averaged (using our own Basic program) by adding the present data run to any previous data runs and saving the results in the memory, until the desired number of sets of data have been averaged. The average intensity value versus time is then saved on floppy disk for further analysis. This basic program will also display the current average plot of data vs time. This basic program is given in the appendix (D). The assembly program supplied by the company is shown in appendix (E).

In the second case the digital memory oscilloscope was used. It acts like a oscilloscope with difference that it can average maximum of 255 frames. It has two channels: one of them is used as a triggering channel and one is for data collection. The software for this system is supplied. The triggering channel selection can be done by the software. Either channel can be used as the triggering channel, with either a low or high input logic depending on experiment. The number of frames to be averaged and time interval between data points is selected by software. This program will display the plot of average signal vs time and also saves it on disk.

The basic difference between these two systems is minor and dependent on the particular experiment. The AI13 A/D converter has 16 channels and all of them can take data simultaneously whereas digital memory oscilloscope(DMO) has only two channels. The number of data points in a run is fixed in the case of DMO (256 points) whereas the A/D converter can take essentially any number of data points in a run. While the time interval between the data points can be varied in the same run for the A/D converters, the time interval between the data points is fixed for the DMO. In any case the choice depends on the particular experiment.

Laser and Laser problem

A Spectra physics model 164 laser was used in our experiments. The two beams derived from the primary beam are focused down to a circular area of diameter 40 um and crossed to produce fringes with separation, d on the order of a few microns. Small mechanical vibrations will produce violent motion of the fringes and destroy the whole experiment. Initially we detected a vibration in the laser head. Because the laser is a water cooled laser, there seemed to be turbulent motion in the plasma tube. This produced a small vibration in the beam which was enough to destroy any standing fringes pattern. This problem was eventually overcome by implementing several different proposed solutions: (a) reversing the water flow in the laser head, (b) using an air trap in the water outlet of the laser head which acts like a mechanical shock absorber, (c) minimizing the spatial size of the experiment and making a firm attachment of the laser chasis to the supporting table and (d) the experimental table was floated on air shocks. Still, sometimes these vibrations were observed in the fringes. Finally these vibrations seemed to be correlated with turbulent motion in the laser tube produced by kinks in the tube supplying water to the laser head. Thus, the final step to eliminate vibration required careful suspension of the hose supplying the cooling water.

CHAPTER IV

NON-INTERACTING SAMPLE STUDIES

Introduction

It has been demonstrated that transparent dielectric spheres can be moved into high intensity regions, as well as, in the propagation direction of laser light (1,31-34). On the other hand, if a sample of these spheres is subjected to crossed laser beams, then the spheres register in the high intensity regions forming a phase grating which diffracts light (1). The strength of the grating depends on the strength of the intensity potential. A study of the amplitude of the phase grating for weakly interacting particles is presented in this chapter, as a function of the height of the intensity potential and beam crossing angles. A comparison is made between these results and a theory for non-interacting particles. For particles larger than 1 um diameter, the radiation pressure easily moves the spheres to the down stream cell wall. This gives us a chance to study the diffusion of the micro-spheres near a single boundary in the absence of other interactions. Dynamical measurements of diffusion indicates a slowing of the diffusion near a wall. In this chapter the author will try to understand this phenomenon experimentally and theoretically.

Results for Non-Interacting Particles
(or Strongly Screened Particles)

This chapter describes details of the data collection procedure and results for static and dynamic experiments on non-interacting colloidal particle samples. By non-interacting particles we mean that the long range coulomb force between particles is highly screened. Thus the particles only interact near contact with strongly repulsive forces. A further increase in added salt will decrease the screening length, and van der Waals attractive forces will produce coagulation. Data was taken using the pin diode as describe in Chapter III.

A lens of 10 cm focal length was used to focus the incident beam in the cell. The crossing angle of the two beams was varied between 6 t0 13 degrees by translating the prism mirror. The two crossed beams produced a periodic intensity potential (i.e. holographic fringe pattern as mentioned in the Chapter II) with fringe spacings, d varing from 1.67 um to 3.21 um. The sample cell gap spacing ranged from 30 um to 50 um. The beam was focus to a spot of diameter 45 um (the calculation of the size of the spot is shown in appendix (B)).

The micron sized particles were drawn to the high intensity region and pushed toward the downstream wall by radiation pressure forces. These particles aligned in rows in the high intensity region to become a transparent diffraction grating. While a third laser beam of different frequency has been used to produce a diffraction pattern of the induced grating, the two interfering beams inducing the grating also produce a self-diffracted intensity pattern. This self scattered diffraction pattern has been used in data collection (rather than using third probe beam). For the non-interacting samples the pin diode was positioned with appropriate attenuation to collect intensity data at the position of the first (or higher order) intensity maxima produced by scattering of the laser beam from the induced diffraction grating. The figures 13a, 13b and 14a, 14b show the diffraction pattern and real space structure for the two different angles. The off axis scattering pattern (diffuse lines above and below the row of intensity maxima) is observed in the figure 13a and figure 14a due to the fact that particles were observed to have fairly uniform spacing parallel to the intensity fringes. Using Bragg's law for the scattering angle of these lines, the spacing of spheres was found to be exactly the diameter of the spheres. This is indicted in figure 13b and 14b by direct imaging through a microscopic objective.

It was also observed that if the fringe separation is less than the diameter of the sphere, then the spheres do not form the grating. This is because the average or net force on the particle is reduced as described in Chapter II. Basically this results from a competition between two adjacent fringes to draw the spheres into their high

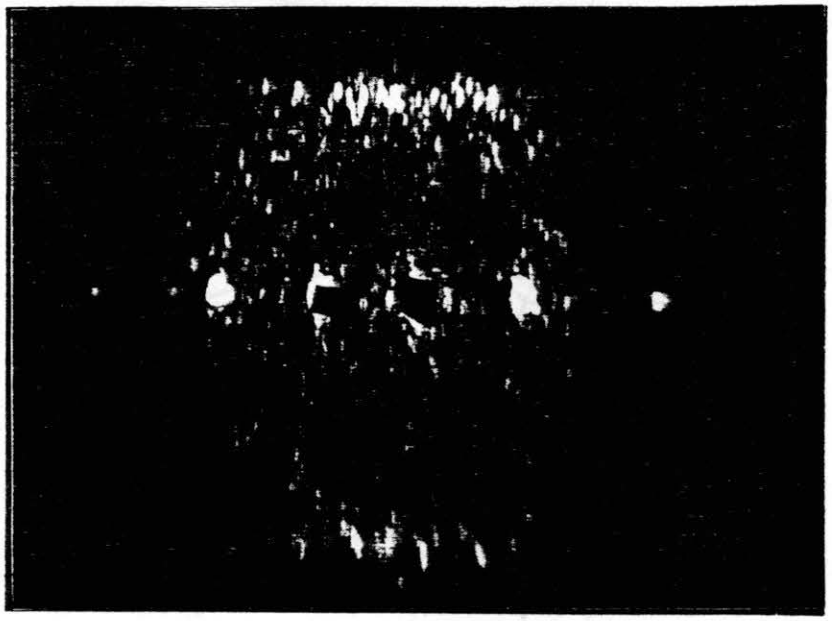

Figure 13a. Self-Diffracted Maxima. The Fringe Spacing is 2.17 um and Diameter of the Spheres is 1.09 um

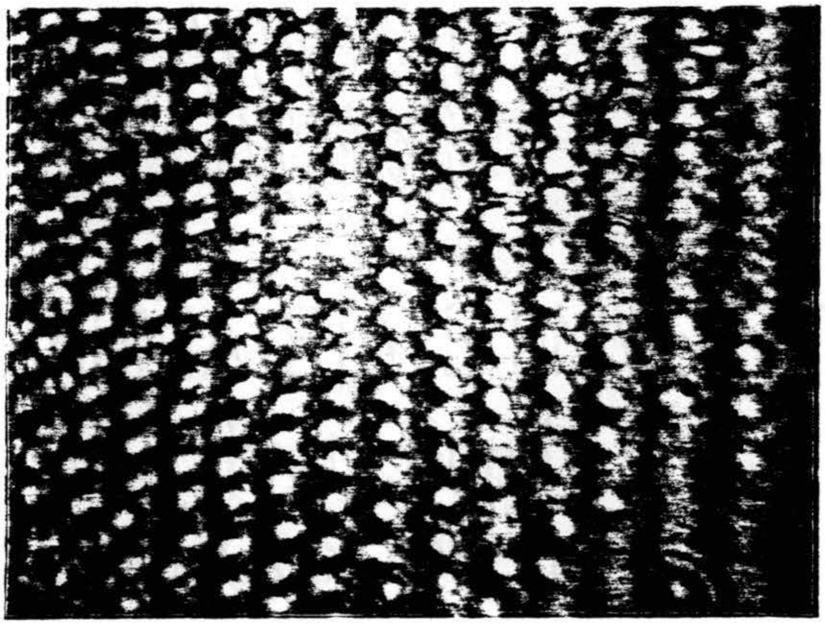

Figure 13b. Real Space Picture. The Fringe Spacing is 2.17 um and Diameter of the Spheres is 1.09 um.

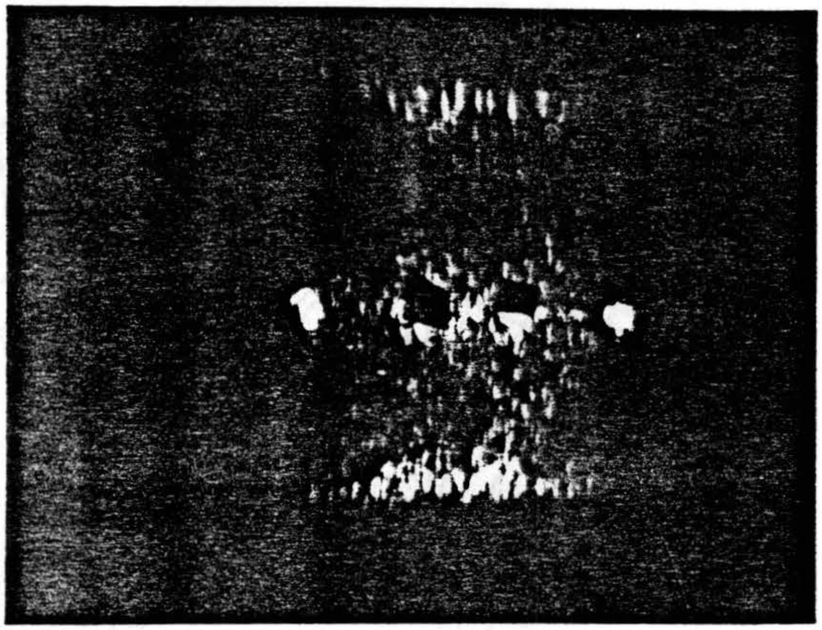

Figure 14a. Self-Diffracted Maxima. The Fringe Spacing is 3.21 um and Diameter of the Spheres is 1.09 um.

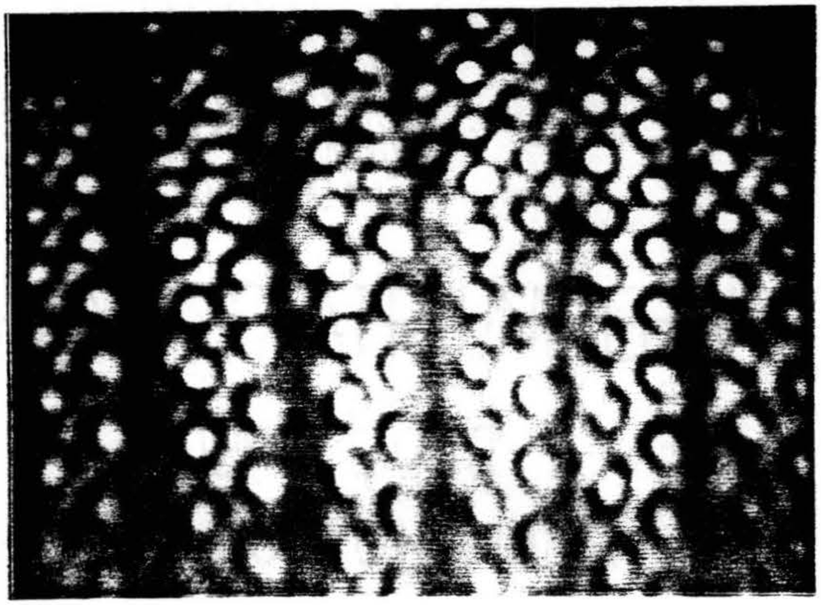

Figure 14b. Real Space Picture. The Fringe Spacing is 3.21 um and Diameter of the Spheres is 1.09 um.

intensity regions. If the fringe separation is larger than the diameter of the sphere but smaller than twice the diameter of the sphere then the grating is formed by single row of pirticles. The real space picture is shown in figure 13b for 1.09 um diameter particles. In this case the angle of crossing is from 12 to 9.5 degrees, the wavelength is 488 nm and a focal length of 11.5 cm was used. On the other hand when the fringe separation is larger than twice the diameter of the sphere then double and triple rows of spheres were found in a single intensity regions. This is shown in figure 14b for crossing angles 6 to 8 degrees.

Data Collection

The magnitude of the intensity of scattered light can be studied as a function of input power and also as a function of time when the holographic grating is modulated in time. Thus the data collection is described in two parts, static or time independent and dynamic or time dependent.

Time Independent Study

In the time independent study the pin diode was positioned on the diffracted maxima such that the area of the diffracted spot is larger than the area of the pin diode (in order to minimize the stray light going to the pin diode). The incident laser intensity was varied. Thus the intensity of the crossed-beams were varied in order to change the depth of the intensity potential. The averaged intensity was measured using the procedure describe in chapter III. When the running average intensity did not drift, the input power of laser and the average intensity data were recorded.

Plots of input power versus relative intensity of the first or second order diffracted maxima were made for four different crossing angles (12, 9.5, 8 and 6.5 degree) and for four different particle sizes (0.481 um, 0.9 um, 1.09 um and 2.02 um). Results are shown in figure 15 to 20. A least square power fit curve is drawn through the data points for each graph. A cubic power law was found to give a reasonable fit for particle sizes 0.481 um for all crossing angles (1) and 0.9 um for 12 degrees crossing angles as shown in figure 15 and figure 18 respectively and less than cubic power law was found for particle sizes 0.95 um, 1.09 um and 2.02 um for crossing angles smaller than 12 degrees as shown in figure 16, figure 17, figure 19 and figure 20. Because the radiation pressure forces are proportional to the volume of the particles (2.46), it is clear that as the diameter of the spheres become larger there is a greater force holding the spheres at the maxima of the intensity. On the other hand, the force on the spheres increases as the ratio of radius of the spheres to the fringes decrease. This is discussed in Chapter II. Hence, as the spheres increase in size, they become more confined at the center of the fringe. This causes the out put signal deviate from the cubic fit. In fact if the spheres are perfectly ordered and

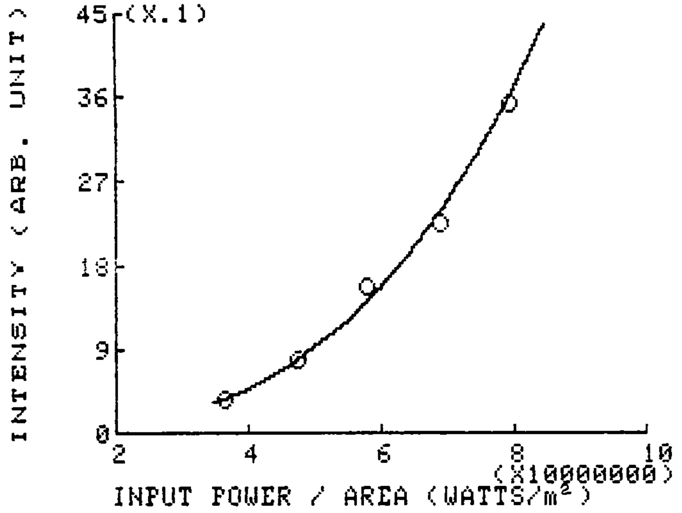

Figure 15. Plot of Output Intensity vs Total Power Per Unit Area. The Fringe Spacing is 2.63 um and Diameter of the Spheres is 0.481 um. Y = A * X ^ 3

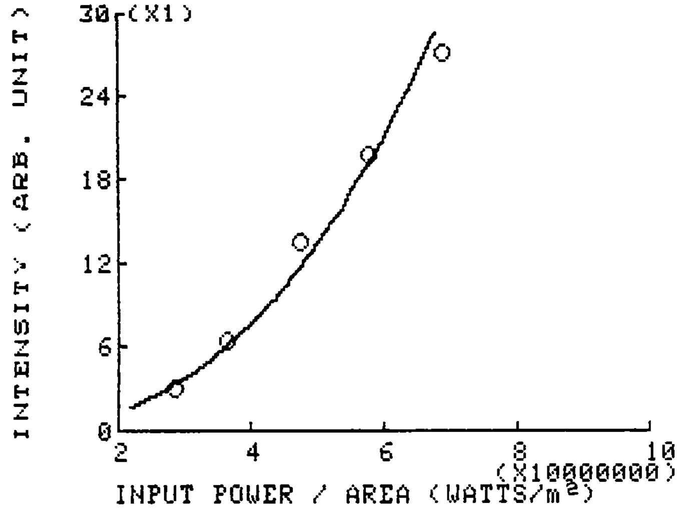

Figure 16. Plot of Output Intensity vs Total Power Per Unit Area. The Fringe Spacing is 2.63 um and Diameter of the Spheres is 0.95 um. Y = A * X ^ 2.5

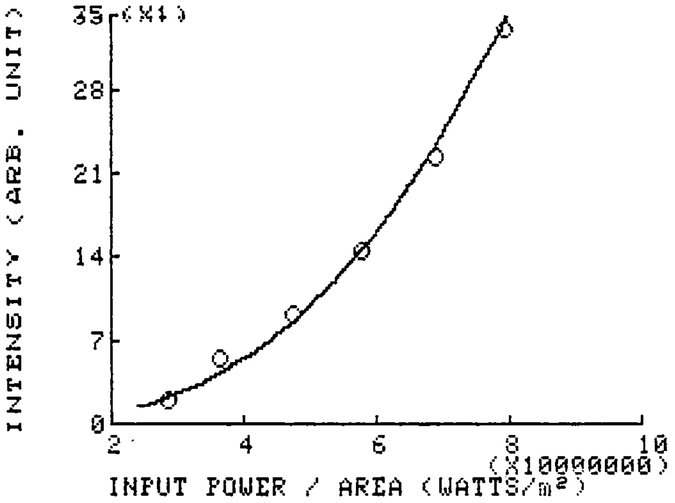

Figure 17. Plot of Output Intensity vs Total Power Per Unit Area. The Fringe Spacing is 2.17 um and Diameter of the Spheres is 0.95 um. $Y = A * X ^ 2.7$

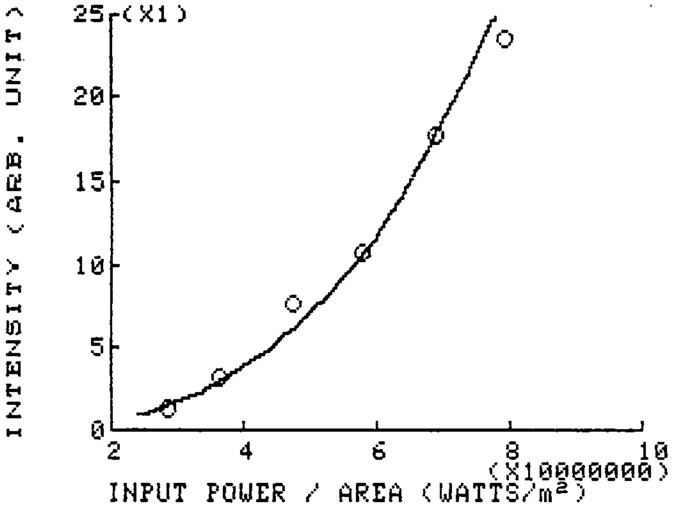

Figure 18. Plot of Output Intensity vs Total Power Per Unit Area. The Fringe Spacing is 1.77 um and Diameter of the Spheres is 0.95 um. $Y = A * X ^ 3.1$

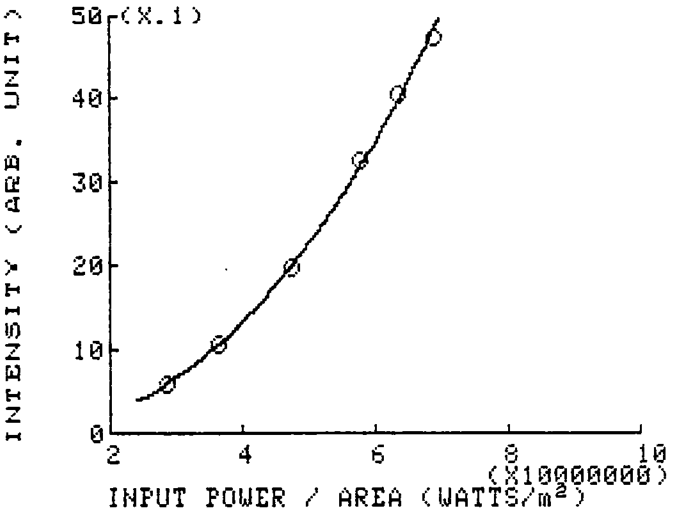

Figure 19. Plot of Output Intensity vs Total Power Per Unit Area. The Fringe Spacing is 2.17 um and Diameter of the Spheres is 1.09 um.
Y = A * X ^ 2.6

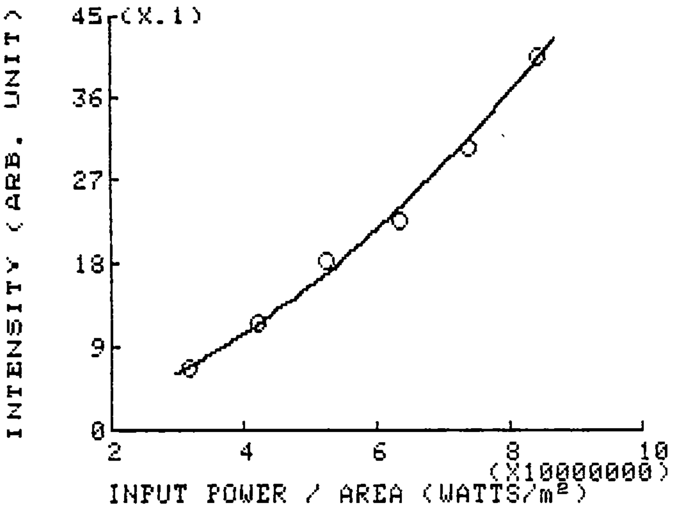

Figure 20. Plot of Output Intensity vs Total Power Per Unit Area. The Fringe Spacing is 2.89 um and Diameter of the Spheres is 2.02 um.
Y = A * X ^ 2

fixed in position, then the alignment is complete and the diffracted intensity should be a linear function of the input intensity for self scattering studies.

Theoretical Model for Particles Alignment in Radiation Potential Well

At low input power we expect the self-scattered intensity to follow a cubic dependence on the input power, because the particles align in proportion to the depth of the intensity potential and scatter coherently proportional to the square of this depth. The third power comes from the strength of the incident beam which scatters from the induced grating. However, once the particles are perfectly aligned by a strong enough radiation field, there can be no further increase in scattering other than that due to the increase input power. Thus we expect the self-scattered response to be cubic at low input power and linear at large input powers. To understand in detail the dependence on input power and temperature, we extended a model presented by D.Rogovin and co-workers (42-44).

First we consider the force on the spheres is given by the equation (2.46) in the Chapter II

$$\bar{F}(grad) = \alpha[(1/2)\bar{\nabla}E^2 + (1/c)\partial(\bar{E} \times \bar{B})/\partial t]. \quad (4.1)$$

Here the first term on the right hand side represents the force which moves the particles into the high intensity regions and the second term represents the force which moves the particle in the direction of propagation of the incident beams. The force for the motion along the intensity gradient (neglecting motion along the direction of propagation) can be written in terms of a potential (see equation (2), reference (1))

$$\overline{F}(\mathrm{grad}) = -\overline{\nabla}U(r) = (\alpha/2)\overline{\nabla}E^{2} \qquad (4.2)$$

where E^{2} is given by equation (2.36), which on neglecting the gaussian beam shape term gives,

$$E^{2} = 2E(10)^{2}[\ 1 + \cos(2kr\ \sin(\theta))] \qquad (4.3)$$

where $|K| = 2k \sin(\theta)$ is the reciprocal of the fringe spacing, d.

Let us try to discuss this quantitavely. If the frictional coefficient is large enough and density is not too far from an equilibrium distribution, then the spatial variation of the probability density of the system, n(r,t) will be similar to that of the imposed potential, U(r). Using the Planck-Nernst equation for the microparticle density one can write

$$\partial n(r,t)/\partial t = D\overline{\nabla}\cdot(\overline{\nabla}n(r,t) + (\overline{F}/KT)n(r,t)\} \qquad (4.4)$$

where $\overline{F} = -\overline{\nabla}U(r)$ is the force on the sphere and D is defined as the diffusion coefficient. For infinite dilution D is given by Stokes' law for spherical particles of radius a,

$$D = KT / 6\pi\eta a, \tag{4.5}$$

For steady state $\partial n(r,t) / \partial t = 0$ and this equation reduces to

$$\mathrm{div}(\overline{\nabla} n(r) - n(r)\overline{\nabla} U(r)/KT) = 0. \tag{4.6}$$

This potential, U(r), can be written more explictly using the result from equation (4.2). At equilibrium the solution of this equation is the Boltzmann distribution:

$$n(r,0) = A \exp(- U(r)/KT) \tag{4.7}$$

where A is a normalization constant.

Hence the probability of finding a sphere in one dimension is given by

$$n(r,0) = A \exp((\alpha E(10)^2/KT)[1 + \cos(2Kr \sin(\theta))]). \tag{4.8}$$

This can be verified by direct substitution into equation (4.6). For particles with $(n_a > n_s)$ the potential causes the spheres to move into the high intensity regions of this periodic intensity potential and to register in rows to form diffraction grating.

The normalization constant, A, can be obtained by the relation

$$\int n(r,0)\ dr = 1. \qquad (4.9)$$

Substituting the expression for n(r,0) in the above integral we find

$$A\int_0^d \exp[(\alpha E(10)^2/KT)\{1 + \cos(2Kr\sin(\theta))\}]dr = 1. \qquad (4.10)$$

Rearranging the equation (4.15) and substituting $p = \alpha E(10)^2/KT$ and $z = 2Kr\sin(\theta)$ we get

$$A\ [\exp(p)/2K\ \sin(\theta)] \int_0^{2\pi} \exp(p\cos(z))dz = 1. \qquad (4.11)$$

This equation can be evaluated by using the standard integral relation

$$1/2\pi \int_0^{2\pi} \exp(+\ z\cos(\theta) + in\theta)\ d\theta = I_n(z).$$

Hence, the normalized probability for finding a sphere at a position r is

$$n(r,0) = (K\ \sin(\theta))/\ I_0(p)$$

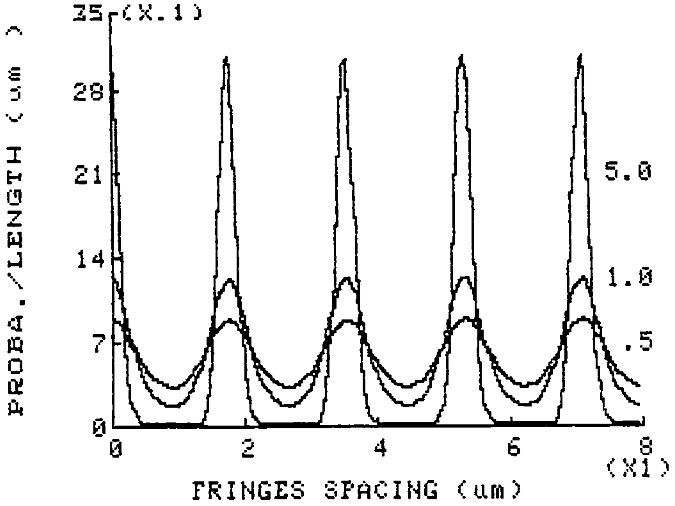

Figure 21. The Fringe Spacing is 1.77 um and the Maximum Potential Energy Relative to KT for 0.5, 1.0 and 5.0 is Presented. Probability for Finding a Sphere as a Function of r.

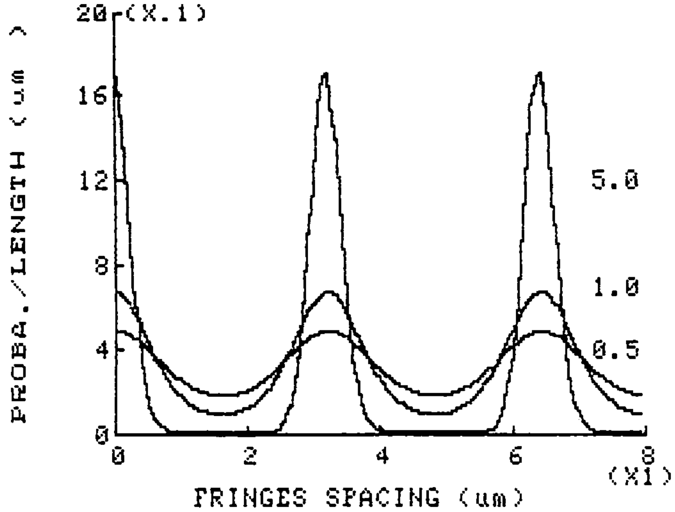

Figure 22. The Fringe Spacing is 3.20 um and the Maximum Potential Energy Relative to KT for 0.5, 1.0 and 5.0 is Presented. Probability for Finding a Sphere as a Function of r.

$$\exp[p\cos(2kr\sin(\theta))]. \qquad (4.12)$$

The figures 21 and 22 show a plot of n(r,0) vs r for three different values of p and four different crossing angles. It is clear that as the p increases, the function n(r,0) becomes sharply peaked. In fact this will behave as a periodic distribution of delta functions in the limit of high incident intensity and/or for sufficiently large spheres in well separated fringes. This probability function spreads out at low intensity or for smaller spheres. From the graph it is clear that n(r,0) is maximum at the middle of the high intensity regions.

Effect of Coherent Self-Scattering by the Two Incident Beams

Because the particle structure is probed by self-scattering of the incident beams, we have two overlapping scattering patterns which add coherently. In this section we formulate the effect of this more complicated scattering geometry. The total scattering intensity is given by (equation (2.16))

$$I \propto |f_a(\theta)^2| \; |\sum_i \exp\,(i\bar{K}\cdot\bar{r}_i)|^2 \qquad (4.13)$$

where $|f_a(\theta)|^2$ is the single particle form factor

and $|K| = 2k\sin(\theta)$ is scattered wave vector.

To proceed it is convenient to consider the scattering amplitude, H(k), for a collection of particles where

$$I \propto |f_a(\theta)|^2 |H(k)|^2 \qquad (4.14)$$

such that

$$H(k) = \left(\sum_i \exp\, (i\bar{k}\bullet\bar{r}_i) \right) \qquad (4.15)$$

Since the probability function, n(r,0) is known for our system and is a continuous function of position rather than a discrete function, the sum in the equation (4.15) can be replaced by the integral. Thus the scattering amplitude can be written for a single k vector as

$$H(k) = \int n(r,0)\ dr\ \exp(i\bar{k}\cdot\bar{r}) \qquad (4.16)$$

Because there are two incident beams in the self scattering experiment, there are two scattered diffraction patterns, (one for each incident beam). Furthermore the two patterns combine coherently due to the mutual coherence of the two incident beams. We now discuss how to properly analyze the scattered intensity under these conditions. Let the detector be placed on the lower side of the beam (1) and (2) at a point which is the 2nd order diffraction spot of the beam (1) and first order diffraction spot of the beam (2) as shown in figure 23. Because the cross beams from the grating, the scattering angle turns out to satisfiy the condition for minimum deviation, and this relation can be written as

$$2d \sin(\theta n/2) = n\lambda \qquad (4.17)$$

where d is the fringe separation

θn is the nth order scattering angle

and λ is the wave length.

Since the diffracted spot of interest is the combination of the first order diffracted spot of the beam (2) and 2nd order diffracted spot of the beam (1), the angle between diffracted beam and the two read beams can be obtained. Let us assume that 2 Ψ is the diffraction angle of the beam (1) which allows us to write the equation (4.17) as

$$d \sin(\Psi) = \lambda \qquad (4.18)$$

Using the relation 2d $\sin(\theta) = \lambda$ from the chapter (1) we get the relationship

$$\sin(\Psi) = 2 \sin(\theta) \qquad (4.19)$$

Let 2 Φ be the first order diffracted angle of the beam (2) on the lower side. This angle can be written as

$$2 \Phi = 2 \Psi - 2\theta \qquad (4.20)$$

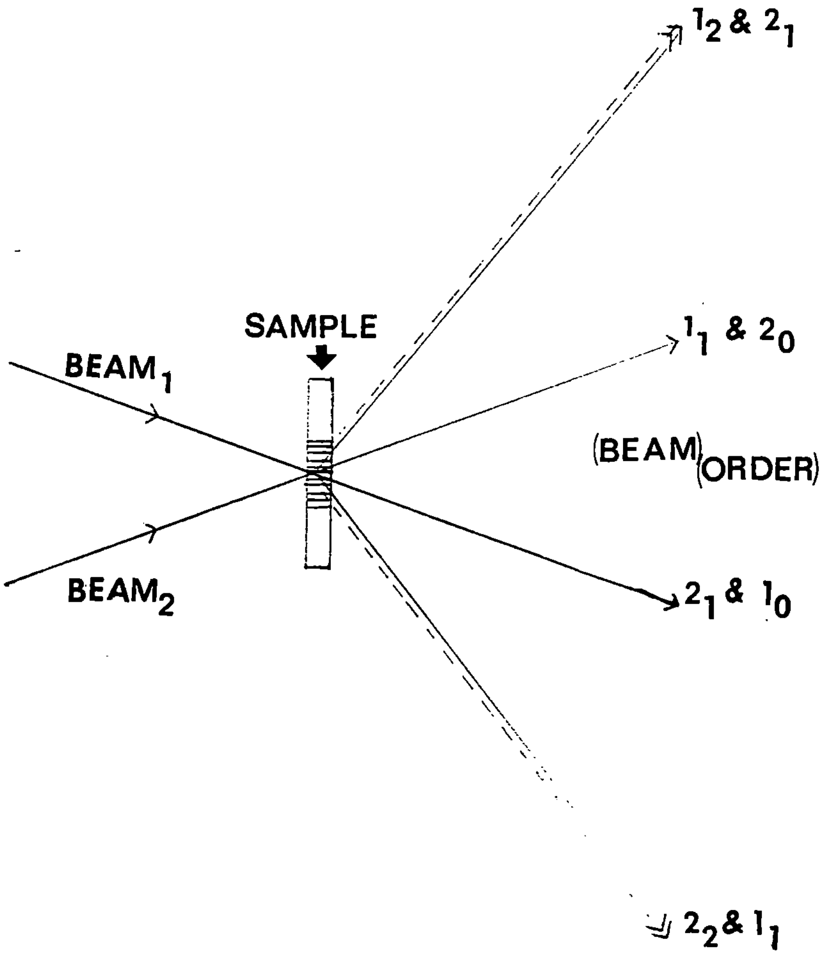

Figure 23. Self-Scattering Geometry for Crossed Beams.

and so $\sin(\Phi) = \sin(\Psi - \theta)$ (4.21)

The above equation (4.21) can be represented using equation (4.19) as

$$\sin(\Phi) = \sin(\theta)\ (\ 2\sqrt{(1 - \sin^2(\theta))} - \sqrt{(1 - 4\sin^2(\theta))}) \qquad (4.22)$$

In fact, in the experiment the crossing angle 2θ was varied from 3° to 12° degrees. The sin square of this angle is very small compared to unity. If we neglect the small terms compared to unity, we get

$$\sin(\Phi) = \sin(\theta). \qquad (4.23)$$

In this approximation we can write the scattering angle for all higher orders as an integer multiple of crossing angle of the beams as

$$\sin(\Phi n) = n \sin(\theta) \qquad (4.24)$$

At this point we have all the tools needed to find the scattering amplitude due to both beams. Let us consider any order of the diffracted maxima. Substituting the expression for the $n(r,0)$ and k , in equation (4.16), one can write the scattering amplitude as

$$H(s) = [(k \sin(\theta))/(I_0 (p))] \int_0^d \exp(i2kr\, n\sin(\theta))\, \exp(p \cos(2kr \sin(\theta)))\, dr. \quad (4.25)$$

Putting $2kr \sin(\theta) = z$ and rearranging equation (4.25) we get

$$H(k) = [1/2\, I_0(p)] \int_0^{2\pi} \exp(inz + p \cos(z))dz. \quad (4.26)$$

This is nothing but the integral representation of the modified Bessel function of nth order, and the scattering amplitude is given by (43,44)

$$H(k) = I_n(p)/ I_0(p) \quad (4.27)$$

Hence the scattering amplitude for 1st order spot and 2nd order spot is given by

$$H(k1) = I_1(p)/ I_0(p) \quad (4.28)$$

and $$H(k2) = I_2(p)/ I_0(p) \quad (4.29)$$

respectively.

The total scattering amplitude is then the sum of the individual scattering amplitude for each beam.

$$H(k1,k2,\ldots,kn) = (f1\, H(k1) + f2\, H(k2) + \ldots \ldots + fn\, H(kn)) \quad (4.30)$$

where for example K1 is the scattered wavevector crossponding to the first order maxima measurement with respect to the first beam and K2 is the scattered wavevector of the second order maxima measurement with respect to the second beam, etc.

The physically measurable quantity is the intensity. The intensity is the absolute value squared of the scattering amplitude, H(K1,K2...Kn). However because we are self-scattering, there is another factor in the scattering intensity, the power of the incident beams. Thus the expression for the output intensity for two self-scattering beams is given by

$$I \propto |H(K1,K2)|^2 \, p \qquad (4.31)$$

where $p = \alpha E(10)^2/KT$.

In the case of non-degenerate four wave mixing a third laser beam is used in order to probe the sample. The intensity of the probe beam is fixed. In this case the scattering amplitude will have only one term. This scattering amplitude, H(K), will be the ratio of modified Bessel function of order 1st to 0th (42,43,44) for first order scattering. The expression for the scattering amplitude can be written as

$$H(k) = f_1 I_1(p)/I_0(p) \qquad (4.32)$$

and the intensity in this case will be simply proportional to the product of the absolute value square of the scattering amplitude.

$$I\ (k) \propto |H_{l}(k)|^{2}\ p. \tag{4.33}$$

At this point we see that intensity I of equation (4.31) and has a cubic power dependence when $p < 1$. As the value of p increases and becomes greater than unity then I deviates from cubic power dependence. At high enough power it is linearly proportional to the input intensity. This model also shows that the higher order diffracted maxima have even larger power law dependences for $p < 1$ (43).

In our experiment the input power from the laser was varied from .015 to .07 watts for four different sizes of spheres and for five different crossing angles. As we have seen, the force on the spheres is dependent on the volume and relative refractive index of the material. It is also shown in equation (4.31) that output intensity is independent of the crossing angle of the two beams. However, from the Chapter II, we have seen that the actual force on the sphere is less than the calculated force from equation (2.49) when the fringe spacing is small compared to the particle diameter. These data are corrected for the effective force by using method describe in chapter II. A theoretical fit to the data is shown in figure 24 and 25 for

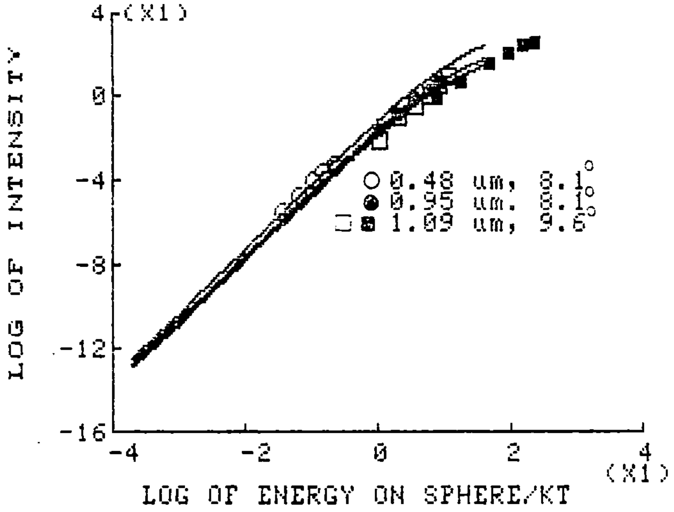

Figure 24. Theoretical Fit to Data for 1st and 2nd order Coherent Mixing. Open Circles, Solid Circles and Open Square as well as Solid Square are for 0.481 um, 0.95 um and 1.09 um Diameter Spheres for Crossing Angles 8.1 , 8.1 , and 9.6 Degrees Respectively.

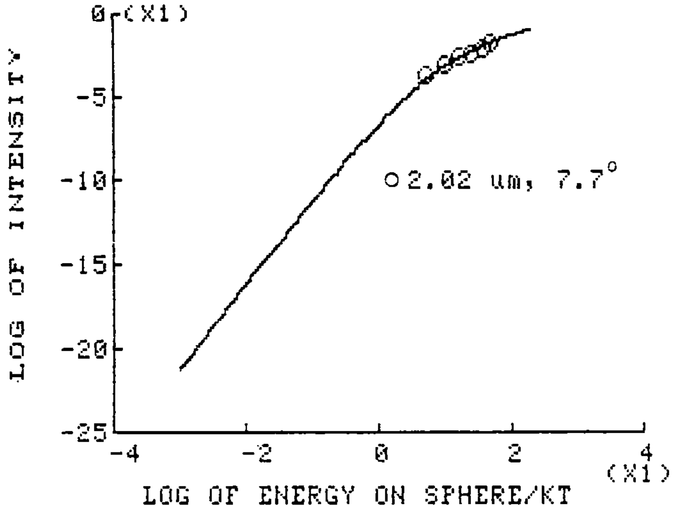

Figure 25. Theoretical Fit to Data for 2nd and 3rd order Coherent Mixing. Open Circles are the Data for the Spheres of Diameter 2.02 um and Crossing angle is 7.7 .

these four different sizes of spheres. We see in figure 24 that the data for 0.481 um diameter spheres fall in the cubic region and the data of 0.95 um and 1.09 um diameter spheres start to deviates from the cubic region. In this case the 1st and 2nd order self diffracted intensities data fits are presented. On the other hand when we used the 2.02 um diameter spheres, then we have an opportunity to study the higher order density modes. The data fit presented in figure 25 is a 2nd and 3rd order superposition of self diffracted maxima. Since the force on the sphere is volume dependent for same relative refractive index, hence these larger spheres are more confined to the center of the intensity potential at the same input powers. These data are in the region where p > 1 and a deviation from the cubic dependence is noted. The arreement between theory and experiment is good.

Study of Intensity as a Function of Crossing angle

The intensity of the self diffracted spot was also studied as function of crossing angle for fixed input power and a plot of this is shown in the figure 26. The intensity of the self diffracted beam diminished as the crossing angle increased. This is due to the particle form factor which is highly angular dependent. This angular dependence in the scattering by single particle was explored in the Chapter II. The effect is due to interference within single finite sized particles. The theory was developed in an approximate

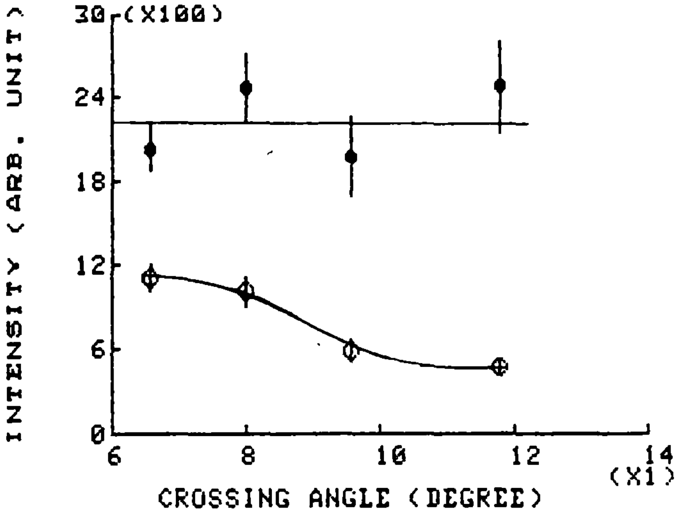

Figure 26. Plot of Output Intensity as a Function of Crossing Angle of the Beams. Input Power of the Write Beams Per Unit Area is 50E6 Watts/m^2 Open Circles is the Data and Solid Circles are Corrected Data using Mie Theory.

way following the approach to Rayleigh and Gans. On the other hand Mie theory discussed in Chapter II, should be used in our case because the relative refractive index is larger than unity and particle diameter is greater than wave length. Taking into account the form factor for Mie Theory with the parameters for our experiment, gives the upper curve in figure 26.

Thus we see that the form factor offers a good explanation as to why the intensity decreases as the crossing angle increases.

Time Dependent Study

The time dependence of particle density grating growth and decay was taken for non-interacting colloids by using the A/D converter and digital memory oscilloscope. The results of these two methods were compared and were found to be in agreement. We found that the small angle light scattering is very difficult using dynamic light scattering (DLS) and is much easier in the cross beam experiment. In dynamic light scattering the spontaneous thermal density fluctuations are measured while in the crossed beams experiment, the density grating is stimulated and its decay is monitored. The crossed beams signal can be much stronger than the DLS signal, and this probably accounts for the case of its measurement.

In the crossed beams experiments two laser beams are crossed in the sample to form holographic fringe pattern.

The dilectric spheres are moved to the high intensity regions by means of the photophoretic force effect. This produces a stimulated density modulation in the two dimensional colloidal system which strongly diffracts light in definite directions. A 488 nm wave was used and is not absorbed by either water or spheres. If one of the beams (the write beam) is blocked, then the stimulated density mode decays. This causes the intensity of the diffracted light produced by the other beam to diminish. Alternatively a third He-Ne laser was also used as a probe beam and both the write beams are blocked.

Data was collected and plotted by the Apple IIe computer as describe in Chapter III. The figures 27a to 31a show the growth and decay of the light intensity diffracted from stimulated density modulation for four different sizes of spheres (0.481 um, 0.95 um, 1.09 um and 2.02 um). Figure 27a to 30a shows the growth and the decay of the grating where the probe beam is one of the write beams and figure 31a. shows the growth and the decay of the grating where the probe beam is a third laser (He-Ne laser). This data is analyzed for both the decay and the growth of this stimulated density modulalation.

The analysis of the diffracted signal is performed as follows: (45,46,47 48). The measured voltage is proportional to the detected intensity. This intensity may not be pure scattering from the sample but may include stray light scattered from cell surfaces, etc. This stray light may mix

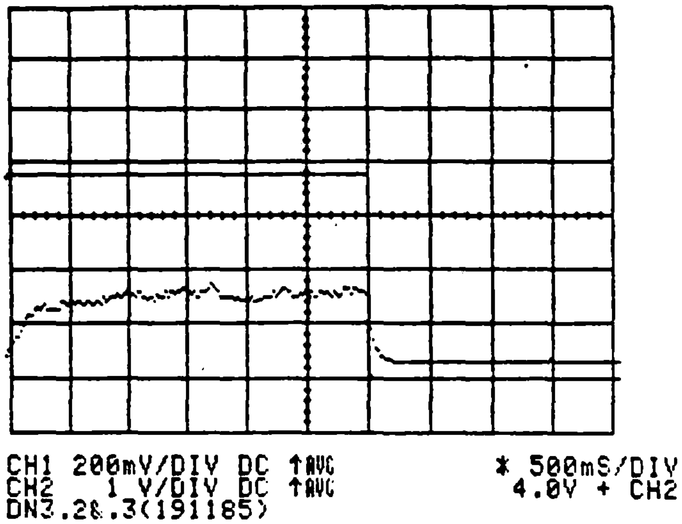

Figure 27a. Growth and Decay of First Order Self Diffrected Grating Mode. Input Power Per Unit Area is 40 MW/m , Diameter of the Spheres is 0.48 um and Fringe Spacing is 1.77 um

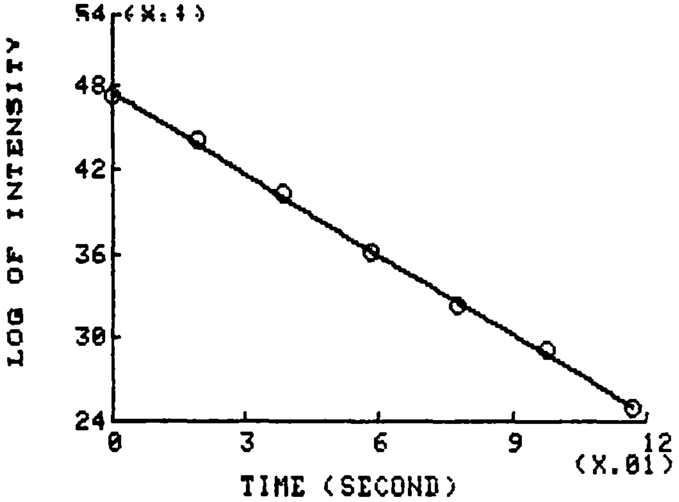

Figure 27b. Decay of First Order Self Diffrected Grating Mode vs Time. Input Power Per Unit Area is 40 MW/m , Diameter of the Spheres is 0.48 um and Fringe Spacing is 1.77 um

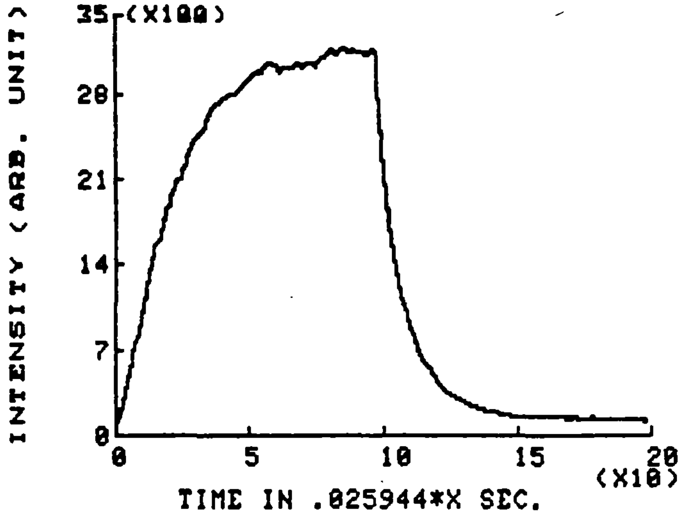

Figure 28a. Growth and Decay of First Order Self Diffrected Grating Mode. Input Power Per Unit Area is 29 MW/m , Diameter of the Spheres is 0.95 um and Fringe Spacing is 2.63 um

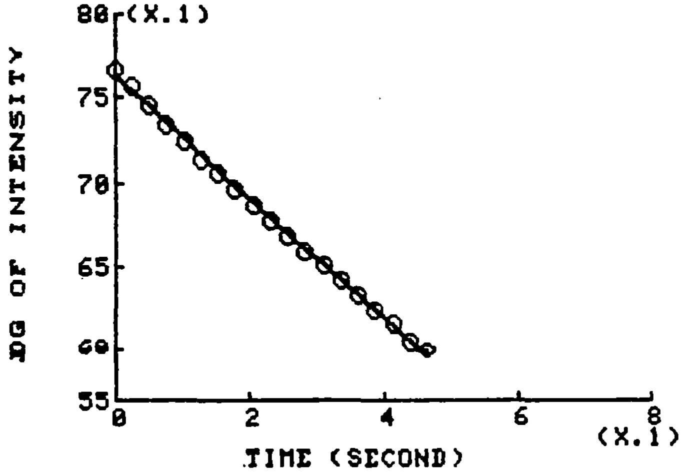

Figure 28b. Decay of First Order Self Diffrected Grating Mode vs Time. Input Power Per Unit Area is 29 MW/m , Diameter of the Spheres is 0.95 um and Fringe Spacing is 2.63 um

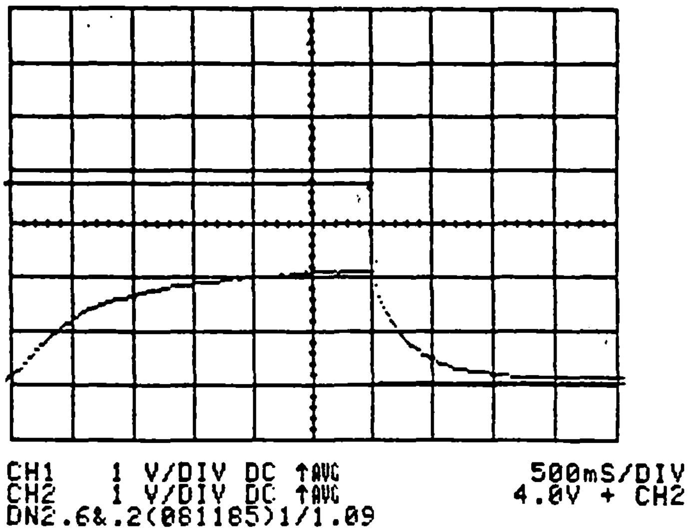

Figure 29a. Growth and Decay of First Order Self Diffrected Grating Mode. Input Power Per Unit Area is 26 MW/m , Diameter of the Spheres is 1.09 um and Fringe Spacing is 2.17 um

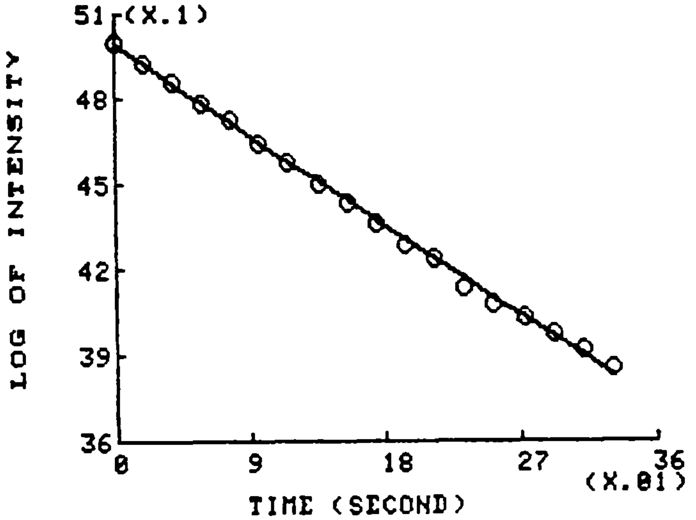

Figure 29b. Decay of First Order Self Diffrected Grating Mode vs Time. Input Power Per Unit Area is 26 MW/m , Diameter of the Spheres is 1.09 um and Fringe Spacing is 2.17 um

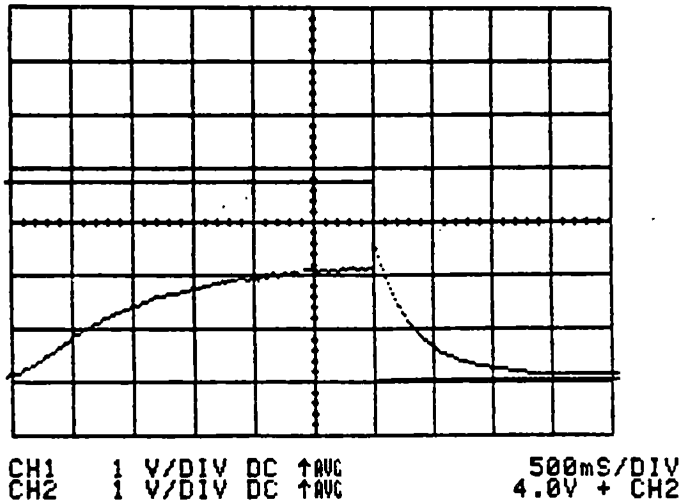

Figure 30a. Growth and Decay of Second Order Self Diffrected Grating Mode. Input Power Per Unit Area is 26 MW/m , Diameter of the Spheres is 2.02 um and Fringe Spacing is 2.89 um

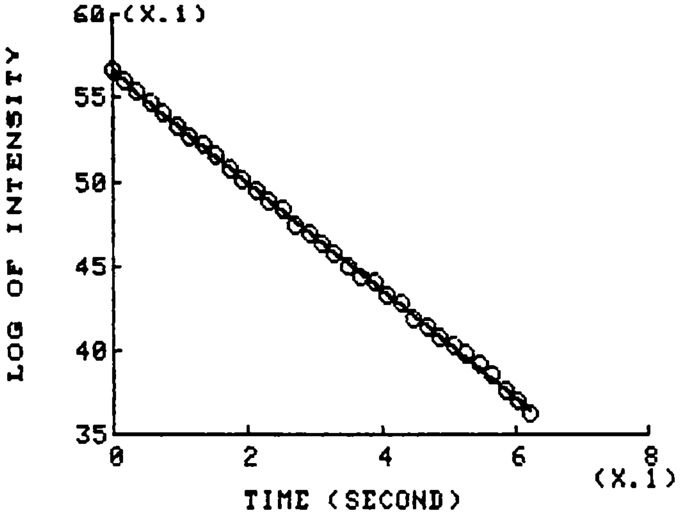

Figure 30b. Decay of Second Order Self Diffrected Grating Mode vs Time. Input Power Per Unit Area is 26 MW/m , Diameter of the Spheres is 2.02 um and Fringe Spacing is 2.89 um

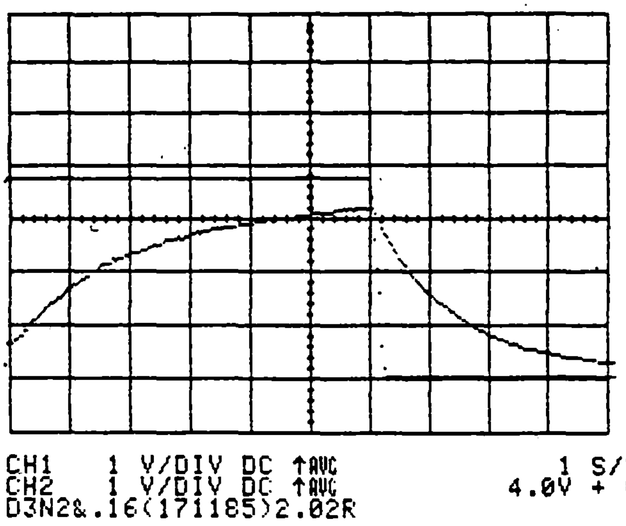

Figure 31a. Growth and Decay of First Order Self Diffrected Grating Mode. Input Power Per Unit Area is 21 MW/m , Diameter of the Spheres is 2.02 um and Fringe Spacing is 2.89 um

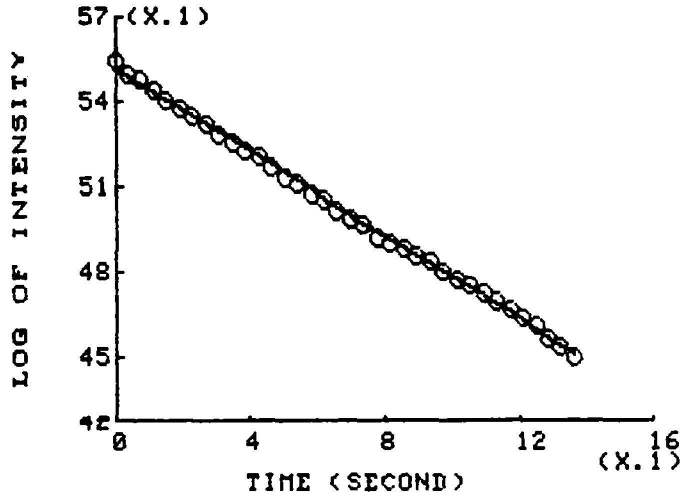

Figure 31b. Decay of First Order Self Diffrected Grating Mode vs Time. Input Power Per Unit Area is 21 MW/m , Diameter of the Spheres is 2.02 um and Fringe Spacing is 2.89 um

coherently or incoherently with the signal. Thus the form for the measured signal is taken to be

$$V(t) = [E(t) + B]^2 + \gamma \qquad (4.34)$$

where E(t) is the electric field amplitude from the sample. B accounts for stray light mixing coherently with the sample signal amplitude (heterodyne effect) and γ represents incoherent mixing.

In general, we can take E(t) to be a sum of the exponentials as

$$E(t) = C\sum_i \exp(-t/T_i) \qquad (4.35)$$

Analysis of our time decay data on independent (hard spheres) particles indicates a good fit with E(t) a single exponential, B equal to zero and set equal to the $V(t \to \infty)$ limit of the data.

Self-Diffusion Measurements

The diffusion of sub-micron particles has been studied previously by CBT (1). The diffusion of small molecules through a swollen polymeric membranes has also been studied using this type of experiment (45) where it was shown that the dependence of the dye diffusion coefficient on the solvent volume fraction does not obey free volume theory. Application of the technique to the liquid crystals indicated that the binary mass diffusion in the nematic phase is faster along the local axis than perpendicular to it (46). While the cited CBT studies focus on interparticle interaction effects, it has been noted in DLS experiments that the diffusion of sub-micron dielectric spheres between two parallel boundaries is slower due to hydrodynamic effects than with no boundary (5). The studies presented here represent what we believe to be an observed transition from free bulk self-diffusion to diffusion hindered by hydrodynamic wall interactions studied by CBT.

In these experiments, hydrodynamic wall effects are encounterted because the particles are pushed by the radiation pressure towards the downstream wall. At constant input power the force is larger on the large diameter particles. This force is always presents to some degree because the decay of the particle allignment is monitored by one of the write beams in the self scattering experiment or by a third beam in a probe experiment. These light beams exert a pressure on the particles even when one (or both) of the crossed beams are eliminated.

Typical data from these experiments is presented in figure 27a to 31a The analysis of the diffracted signal is performed by using equation (4.34) with $B = 0$ and γ is extraced from the long time decay data (background). From a log plot of the data (figure 27b to 31b) we see that the decay is well approximated by a single exponential decay where we have:

$$E(t) = C \exp(-t/Td) \tag{4.36}$$

and the slope obtained from the figure 27b to 31b is related to relaxation time constant as

$$1/Td = slope/2. \tag{4.37}$$

Formally we can understand these experimental results on the basis of the diffusion equation introduced in equation (3.4). While the force term involving F is present for the formation of the periodic particle grating, it is absent when one or both of the incident beams is eliminated and the simple diffusion equation results:

$$\partial n(r,t)/\partial t = D\nabla^2 n(r,t) \tag{4.38}$$

where D is the diffusion coefficient. The intermediate scattering function, S(K,t), is related to the density, n(r,t), by a spatial fourier transform. Thus we may fourier transform the diffusion equation given in equation (4.38) to find

$$\partial S(K,t)/\partial t = -DK^2 S(K,t) \tag{4.39}$$

which is easily solved to find

$$S(K,t) = [\ \exp(\ -Dq^2t)]\ \delta(q \pm K) \qquad (4.40)$$

where $\overline{K} = \overline{K}i - \overline{K}s$ is the interpreted as the scattered wave vector and $\delta(q \pm K)$ is the delta function. The function results from the assumption that a single density mode with wave vector q (or fringe spacing $d = 2\pi/q$) is present at t =0.

The physically measurable quantity is the intensity (in this case voltage) which is directly proportional to the absolute value squared of the S(K,t). Comparing equation (4.37) to (4.40) we see that slope is

$$\text{slope} = 2\ DK^2 \qquad (4.41)$$

and so equation (3.37) becomes

$$T = 1\ /\ DK^2. \qquad (4.42)$$

Thus we expect the measured relaxation time to be directly related to the particle self diffusion constant and the scattered wave vector determined from the incident beam crossing angle. The measured value of the diffusion coefficient for these four different diameter particles are shown in Table I along with the theoretical diffusion coefficient value for an infinitely dilute sample with no boundary (the free diffusion coefficient). The measured diffusion coefficients are smaller than free diffusion

TABLE I

COMPARISON OF MEASURED DIFFUSION CONSTANT TO FREE DIFFUSION CONSTANT FOR FOUR DIFFERENT SIZES OF SPHERES

Diameter of the Sphere in um	Fringe Spacing in um	Input Power per unit Area in Watts/m	Measured Diffusion Constant, D in m^2/s.	Free Diffusion Constant in m^2/s.	$Q = ((KT/D) - 6\pi\eta a)/A$ in Kg/m-s.
0.481*	1.77	39.39E6	6.91E-13	8.90E-13	1.986E4
0.95 *	2.63	29.05E6	3.15E-13	4.51E-13	1.685E4
1.09 *	2.17	21.49E6	2.10E-13	3.93E-13	2.999E4
2.02 **	2.89	26.46E6	8.55E-14	2.12E-13	2.854E4
2.02 *#	2.89	42.49E6	6.87E-14	2.12E-13	3.885E4

A is the square of the radius of the spheres times cos(θ)
* Self-diffracted 1st order maxima, Temperature 20° C
** Self-diffracted 2nd order masima, Temperarure 20° C
*# Third laser (He-Ne) as a probe beam, 1st order maxima and Temperature 20° C

coefficient. We beleve this is to be due to hydrodynamic wall effects discussed previously.

The boundary drag effect can be examined by substracting the Stoke's drag $6\pi\eta a$ from the measured diffusion constant divided into the thermal energy. These values are listed in Table I. As the radiation pressure increases, the sphere exerts more force on the boundary layer and as a result the boundary layer becomes thinner. The thinner the boundary layer is, the greater the drag force. This is discussed in more detail in the following section.

Finally we note the effect of coherent mixing of the two self scattered beams may be seen in the data in figure 27a, 28a, 29a and 31a. When one of the beams is blocked then we see an instantaneous decrease in the diffracted intensity for 0.481 um, 0.95 um and 1.09 um diameter spheres as shown in figure 27a to 29a. However, for 2.02 um diameter spheres the effect is reversed, the diffracted intensity instantaneously increases when one beam is blocked as shown in figure 30a. It was shown in Chapter II that the scattering amplitude of individual spheres can have negative value. The total scattering amplitude is the sum of all amplitudes reaching the detector, and the intensity is proportional to the absolute value squared of the total amplitude. For 2.02 um diameter spheres the scattering amplitude of one beam is positive and other one is negative. This can easily be obtained from the Chapter II form factor calculation and accounts for the observed behavior.

Alternatively, when a third laser beam probe was incident normal to the grating plane and both the write beams are blocked the results shown in figure 31a. and 31b. were produced. The diffusion coefficient was measured be to smaller than the self diffracted method of measuring. Presumably this is due to the larger input crossed beam power which moves the particles closer to the wall. However, more extensive studies need to be done. With the smaller probe power (5.0 mW) and the elimination of the incident crossed beams, during the decay, the probe beam method offers several advantages: no coherence effect due to two beam interference, elimination of most of the radiation pressure during the decay, no extra force parallel to the wall, etc.

BB Pellets Experiment

To explore the boundary effect on the particle motion we did an experiment with BB pellets and glycerin. These BB pellets are dropped in the middle and near the wall of a jar containing glycerin. Here we used two types of jar with diameters of the jar 14 cm and 3.6 cm and length 25 cm and 40 cm respectively. The BB's were 0.44 cm in diameter. When these BB's are dropped, they will experience a drag force and soon reached their terminal velocity. The velocities are recorded and shown in Table II. Here we observed the velocity of the BB's along the wall are smaller than the velocity of these BB's on the cylinder axis. The velocity of the BB's on the cylinder axis is then corrected further for an unbound fluid using the following formula (42)

$$U = V/\{1 - [1/(K + a\ L1)R][5.6112 - 5.5642(a/R)^2]\} \quad (4.43)$$

where U is the velocity in the unbound fluid

V is the velocity on the cylinder axis

a is the radius of the BB pellet

R is the radius of the cylinder

and K and $L1$ are constant dependent on the radius and force on the BB's, as well as, radius of the cylinder.

The value of the constants can be obtained from Table 7-5.4 of reference (49). Using these values the unbound velocity was obtained as shown in Table II for these two cylinders. These velocities are in good agreement with that obtained assuming Stoke's drag U = 4.5 cm/sec.

In these experiments the only force acting on the BB's is the gravitational force which is vertically downwards. So far no external force is exerted on the BB's to hold them near the wall. In general the BB's will be moved away from the wall by a lift effect (50). In conclusion we note that the results of this very simple experiment indicate a strong boundary effect.

TABLE II

COMPARISON OF VELOCITY OF BB PELLETES ALONG THE WALL OF THE CONTAINER TO THE MIDDLE OF THE CONTAINER AND THE CORRECTED FOR THIS CYLINDERICAL BOUNDARY SHAPE IN GLYCERIN

Diameter of BB's = 0.44 cm
Mass of BB's = 0.34 gm
Density of BB's = 7.64 gm/cm
Temperature = 19° C

Density of Glycerin = 1.26 gm/cm

Diameter of the Container in cm	Velocity Along the Wall in cm/sec	Velocity at the Middle in cm/sec	Corrected Velocity for infinite Wall Separa. in cm/sec
3.6	2.12 + 0.19	3.15 + 0.15	4.25 + 0.21
14.0	2.38 + 0.17	4.24 + 0.17	4.54 + 0.20

In the previous experiment we demonstrated the effect of the wall on the terminal velocity of the BB's, where the external force exert on the BB's to stay near the wall was zero. However, another type of experiment was done by using a large tank filled with glycerin. In order to introduce a force holding the BB's near the wall, the tank was placed at an angle. In this way there will be two force components due to gravity: along the direction of motion and perpendicular to the direction. The force perpendicular to the direction of motion will hold the BB's near the bottom wall and result in an extra resistive drag. The measured velocities of the spheres are shown in Table III along with the force components parallel and perpendicular to the wall. It is observed that the BB's have both translational and rotation motion. For small angles (with respect to horizontal) the motion is dominated by rotational motion and as the angle increases the rotational motion decreases.

The thickness of the boundary layer depends on the balance of forces perpendicular to the motion. These forces are due to gravity and hydrodynamic effects. For laminar flow we argue that

$$F(e) = D(L)\ V \tag{4.44}$$

$$F(d) = H(D(L))\ V \tag{4.45}$$

where F(e) [= $m'g \sin(\theta)$] is the component of the force acting along direction of the velocity

TABLE III

COMPARISON OF VELOCITY OF BB'S PELLETES ALONG THE WALL OF THE CONTAINER WHEN BOTH FORCES PARALLEL AND PERPENDICULAR TO THE MOTION ARE PRESENT

Diameter of BB's = 0.44 cm
Density of BB's = 7.64 gm/cm
Mass of BB's = 0.34 gm
Temperature = 19° C

Force due to Gravity = 278.9 dy
Density of Glycerin = 1.26 gm/cm

Angle with the Horizon in degree	Velocity of the BB's in cm/sec	D(L) = F(e)/V in gm/sec.	H(D(L)) = F(d)/V in gm/sec.
14.6	0.17 + 0.01	275 + 10	3.84 + 0.38
17.5	0.22 + 0.01	256 + 10	3.17 + 0.32
20.5	0.27 + 0.01	239 + 9	2.68 + 0.27
23.5	0.35 + 0.01	214 + 8	2.30 + 0.23
80.6	1.07 + 0.04	172 + 17	0.17 + 0.02
85.7	1.12 + 0.04	167 + 17	0.075 + 0.008
87.5	1.14 + 0.04	165 + 17	0.044 + 0.009

F(d) [= m′g cos(θ)] is the component of the force acting perpendicular to the wall

D(L) is the coefficient of drag parallel to the wall

H(L) is a lift coefficient

and L is the distance from the particle center to the wall.

D(L) and H(L) are assumed dependent only on the thickness of the boundary layer in general. A plot of (H(L)/D(L)) vs D(L) can then be determined experimentally from a ratio of the force components and a measurement of the BB′s velocity. The result is shown in figure 32 where we see that H(L) is directly proportional to the square of the D(L).

Finally we note that the diffusion mechanism of microsized spheres near a single boundary were different from unbounded diffusion mechanism. The experiment was done with the BB pellets and glycerin suggests an explanation of this phenomena. The thin layer of fluid between the spheres and the boundary is related to the lubrication layer which becomes smaller as the radiation pressure increases. The drag of the bulk fluid is different from this thin layer.

Growth of the Density Grating

Lastly in this chapter we look at the growth of the density grating. The grating formation time should depend on the incident crossed beams power, sphere size, refractive

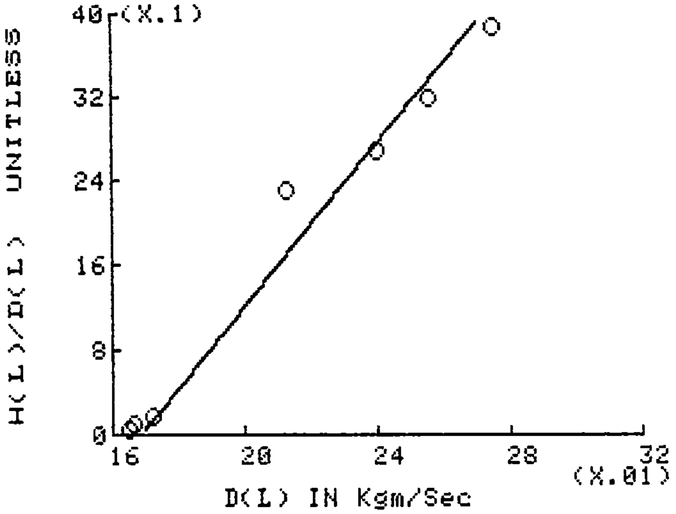

Figure 32. Ratio of Perpendicular Force to Parallel Force vs Drag Force Coefficient

indix of the particles as well as viscosity of the solvent and fringe spacing. The diffraction pattern produced by scattering from the grating contains information on the amplitude of the different spatial modes being stimulated. The zeroth order mode corresponds to a uniform average particle distribution and is time independent. The first order mode has a wavelength, d, equal to the fringe spacing and initially grows most rapidly when the crossed beams are turned on. Higher order modes have shorter wavelength and initially respond weakly to the crossed beams (44). Because of this, we ignore the effect of the higher order modes than the first in our analysis of the initial growth in the CBT experiments. Furthermore we assume that this growth is of the following form

$$E(t) = 1 - \exp\,(t/Tf) \qquad (4.46)$$

and fit the data using equation (4.34) to determine the formation time, Tf. The time for different experimental conditions are listed in Table IV.

We expect the formation time to be inversely proportional to the drift velocity produced by the radiation field and proportional to the length the particle must diffuse ($d = 2\pi/K$):

$$Tf = K'/(k\ V) \qquad (4.47)$$

where K' is the universal constant

$k = 2\pi/d$; d is the fringe spacing

and V is the drift velocity which is given by

$$V = F/\xi \tag{4.48}$$

with ξ being a friction factor. The diffusion constant, D is related to the friction factor ξ via the relation

$$\xi = KT/D. \tag{4.49}$$

Finally putting every thing together in equation (4.47) the universal constant, K', becomes

$$K' = (Tf/Td)\ p\ (k/ks)^2 \tag{4.50}$$

where $Td\ (= 1/DKs^2)$ is the relaxation time constant determine previously

$p\ (= \alpha E(10)^2/KT)$, $E(10)$ is the amplitude of the applied field

and Ks is the scattered wave vector.

The value of the relaxation time constant, Td, can be obtained from Table IV. Here we are not using the free diffusion constant in order to obtain the relaxation time constant because the spheres are diffusing near a wall. We have seen from the previous discussion that the hydrodynamic wall effects produce an increased drag.

From fluid mechanics we know that the velocity of the fluid at the wall and velocity of the fluid at the sphere will be at rest with respect to the wall and sphere surface, respectively (strict boundary condition). A very thin layer will stay between the wall and sphere which is known as the boundary layer. The thickness of this thin layer of fluid is dependent on the surface roughness of the sphere as well as the wall, surface tension of the fluid, viscosity of the fluid and pressure on the sphere. This thin layer undergoes a very high strain when the spheres try to move in the high intensity region. The fluid in the front of the sphere will slip through that thin layer, which causes the sphere to experience a large drag. This slows down the particle. Hence we used the measured relaxation time constant, Td, instead of the theoretical free relaxation time punctuation Stoke's-Einstein constant. The effect of the force due to the finite size of the spheres are also taken into consideration. These values of universal time constant are listed in Table IV.

The universal constant of the first order self diffracted intensity maxima of 0.481 um, 0.95 um and 1.09 um is shown in the begining of the Table IV. We see that the universal constant of 0.481 um diameter sphere is about half of the value of the universal constant obtained for 0.95 um and 1.09 um diameter sphere. This suggested that we are missing an important factor in our estimate of the formation time. The deviation is systamatic following either the

TABLE IV

COMPARISON OF FORCED DIFFUSION TIME OF DIFFERENT GRATING ORDER MODE TO FREE RELAXATION TIME FOR FOUR DIFFERENT SIZE OF SPHERE AT FOUR DIFFERENT FRINGE SPACING

Diameter of the Sphere in um	Fringe Spacing in um	Potential Energy on Sphere/KT (P = U/KT)	Forced Diffusion Time Tf in sec.	Ratio K′ = (Tf/Td) (k/Ks)P	Ku′= K′/a per m.
0.481*	1.77	0.235	0.176	0.399	1.66E6
0.9 *	2.63	1.208	0.397	0.878	1.85E6
1.09 *	2.17	1.192	0.350	0.728	1.34E6
1.09 *	2.17	1.015	0.488	0.865	1.58E6
2.02 **	2.89	7.646	0.968	2.403	2.38E6
2.02 **	2.89	6.162	1.406	2.739	2.71E6

* Self-diffracted 1st order maxima, Temperature 20° C

** Third laser (He-Ne) as a probe beam, 1st order maxima and Temperature 20° C particle radius or energy/KT of the system. If we divide this constant by the radius of the sphere then the values of Tf almost agree within experimental error. On the other hand for a 2.02 um diameter sphere there is no agreement. The first order diffracted spot of 2.02 um diameter sphere was probed by a third laser (He-Ne laser). This laser probed perpendicular to the grating and the two write beams (Ar-ion) were blocked. When both the write beams are on more radiation pressure is exerted on the sphere than when they are blocked. Hence the sphere feels more restoring force when they are diffusing to form a grating. This information can not be obtained from this type of experiment and this type of data.

Clearly a great deal more work needs to be done to sort out the trends noted in these preliminary experiments.

CHAPTER V

INTERACTING SAMPLE STUDIES

Introduction

When highly charged polymer spheres are intoduced into deionized water, they interact with each other via screened coulombic interactions. The screened coulomb potential causes the particles to maintain a rather large and uniform average distance from each other. In some regions the particles order as in a solid and other places as in a liquid. This makes the sample ideal for the study of liquid and solid behavior. When the liquid phase is subjected to an external periodic potential then it can be forced to undergoes a phase change if the average particle separation and spatial period of the external potential are properly adjusted.

Experiments on the interacting samples were divided into three portions. The first is a study of the ordering of particles in a harmonic external field for different spatial periods of the external field (or incident beam crossing angle). The second is a study of the output intensity of the different diffracted intensity maxima as a function of input power and crossing angle. The third is the study of the growth and decay of these different density modes when the external field is modulated.

Study of Structure

When an X-ray beam is scattered from a single or polycrystaline structure, the scattered intensity distribution gives information about the structure of the crystal. Similarly when laser light is scattered from a strongly interacting colloidal sample, the scattered intensity distributions contain information about the particle order. In the case of an amorphous order, the scattered light produces a diffuse Debye-Scherrer ring concentric about the main or unscattered beam as shown in figure 33. Bragg's relation described in Chapter II by equation (2.13) can be used to determine the average particles separation. We simply assume the Debye-Sherrer ring structure to be similar to a powder pattern. For 488 nm wavelength the angle of scattering is about 8 degrees and average particles separation,a, is found to be 2.4 um. In the case of solid ordering the parameter a [= d(hkl)] is identified with the separation between planes and represented as d(hkl), where h,k and l are Miller indices.

As in the case of noninteracting particles described in Chapter IV, when strongly interacting particles are subjected to a periodic intensity potential, they generally line up along the high intensity regions of the fringe pattern to produce diffraction grating which strongly scatters light. However, because the particles are

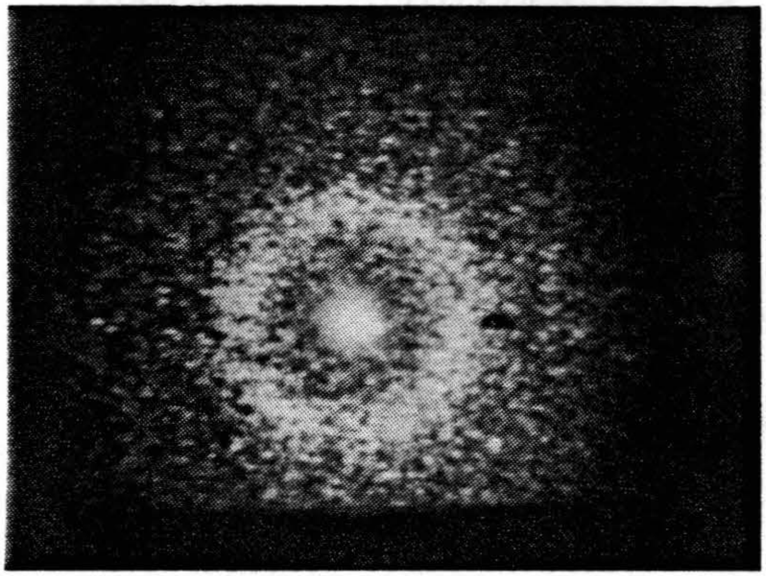

Figure 33. Debye-Scherrer Ring. The Scattering Angle is 7.4 Degrees, Diameter of the Spheres is 0.95 um and the Wavelength used is 488 nm

interacting strongly over micron distance scales, there is a uniform separation between particles within a row and registration between rows. This results in the appearance of other intensity maxima outside the cross beam plane indicating other periodic structures. These periodic structures are not directly excited by the crossed laser beams. However, these modes are coupled to the laser stimulated mode. Evidently this colloidal liquid is frozen, being two dimensionally ordered by applying a one dimensional external field which directly breaks the symmetry of the liquid state parallel to the stimulated density mode.

When the fringe separation, d, is slightly larger than the average particles separation, a, the diffraction from the fundamental density mode which is excited directly by the two crossed beams was observed. The other diffraction spots from the secondary density modes, which are not directly excited by the crossed beams, were not observed. This is because the width of this periodic intensity potential is sufficiently large such that the interaction between particles in adjacent rows is reduced. The particles lose their correlation between rows of this structure. Although the fundamental mode is produced, the diffracted light from this mode is less than that for other configarations. Figure 34a shows diffracted maxima for this incident beam crossing angle. Also visible are the Debye-Sherrer rings, produced by self scattering of each incident beams. The intensity of the Debye-Sherrer ring was measured and found to be uniform around the ring within experimental error. Figure 34b shows the real space picture order for this experimental configuration. Here the particles try to align along the high intensity region and to form other registrations. There are weak correlations between these rows and the symmetry is weakly broken in this liquid phase.

A more interesting case to study is when the fringe separation is larger than the size of the particles but smaller or equal to the average particles separation. In this configuration the particles line up in rows along the fringe direction. Due to the fact that there are interactions between the particles and that the fringe spacing is smaller, there exists a correlation between these rows. This means that the rows register forming density modes in other directions, a breaking of the liquid symmetry. Figures 35a to 37a show the diffracted maxima from the directly excited (fundamenal) and indirectly excited other (secondary) modes. The corresponding real space pictures are shown in figure 35b to 37b. The diffraction patterns represent the reciprocal lattice of the two dimensional real space lattice.

The scattering angles of the intensity maxima are measured as explained in appendix (A), and the separation between the corresponding real space scattering lines were obtained using Bragg's law (For two dimensional systems we have scattering lines instead of planes as is the case in three dimensions). These lines with proper orientation are plotted in figure 35c to 37c. From this construction we find that the packing fraction of these lattices for three different crossing angles are the same. Thus the density of of these micro-crystals does not change much with the application and variation of the external field. These real space structures can be identified as destorted hexagomal lattices. It is observed that for a fringe separation equal to the square root of half of the square of the average particle separation, then the two diffracted intensity maxima of fundamental mode move outside of the liquid Debye-Sherrer ring figure 35a. There are also four other diffracted intensity maxima from the secondary density modes which appear near the Debye-Sherrer ring. These four intensity maxima are 90° degrees apart from each other and 45 degree from the fundamental diffracted maxima in a plane normal to the incident beam. Using the Bragg's law, this micro-crystal structure was identified as a two dimensional square lattice. The principle axis of this lattice is along one of the secondary registration directions. The secondary diffracted intensity maxima are from the [10] lines of the micro crystal square lattice and the fundamental diffracted maxima correspond to scattering from (11) lines. There are also two diffuse spots visible in figure 35a which correspond to scattering from other (11) lines. The lattice constant was found to be 2.3 um as shown in figure 35c.

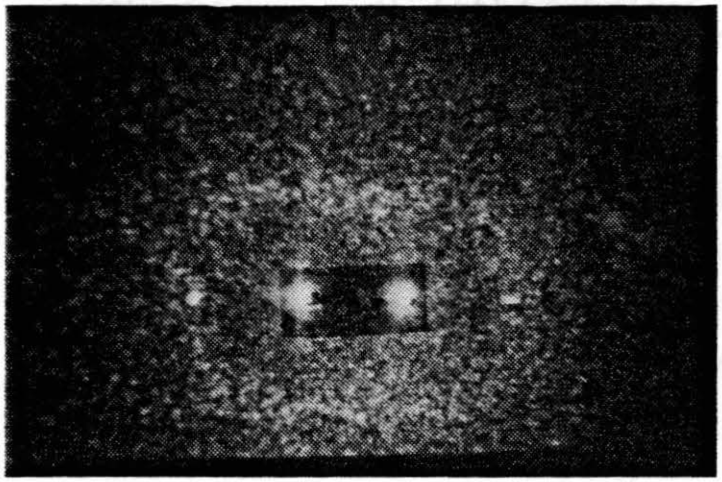

Figure 34a. Self-Diffraction Pattern. The Average Particle Separation is 2.5 um, the Fringe Spacing is 3.2 um and the Two Central Bright Spots are due to the Emerging Crossed Beams

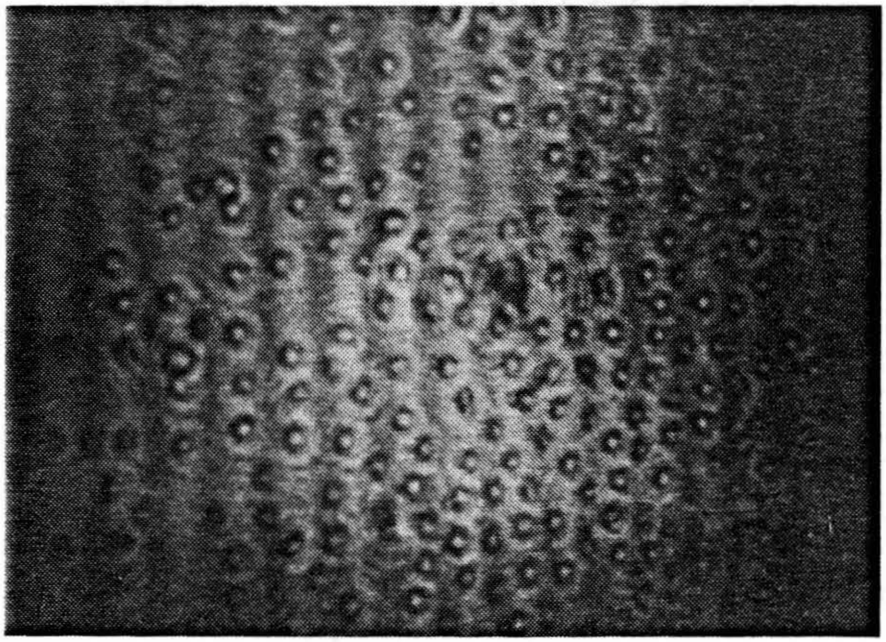

Figure 34b. Real Space Image of Corresponding to the Diffraction in 34a.

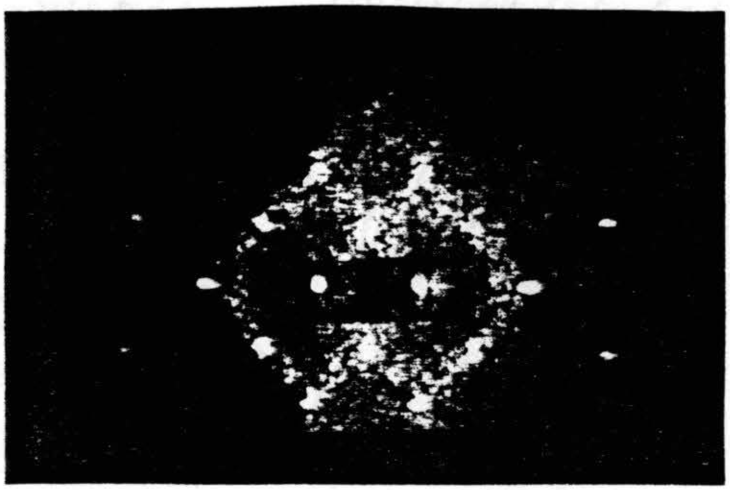

Figure 35a. Self-Diffraction Pattern. The Average Particle Separation is 2.5 um, the Fringe Spacing is 1.77 um and the Two Central Bright Spots Partially blocked by Tape are the Emerging main Beams

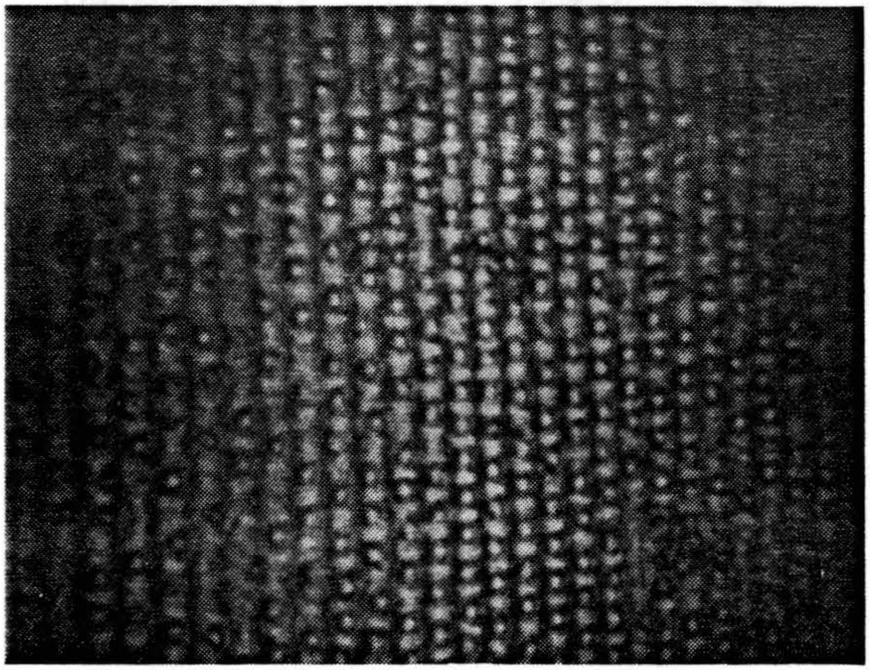

Figure 35b. Real Space Image of Corresponding to the Diffraction pattern in Figure 35a

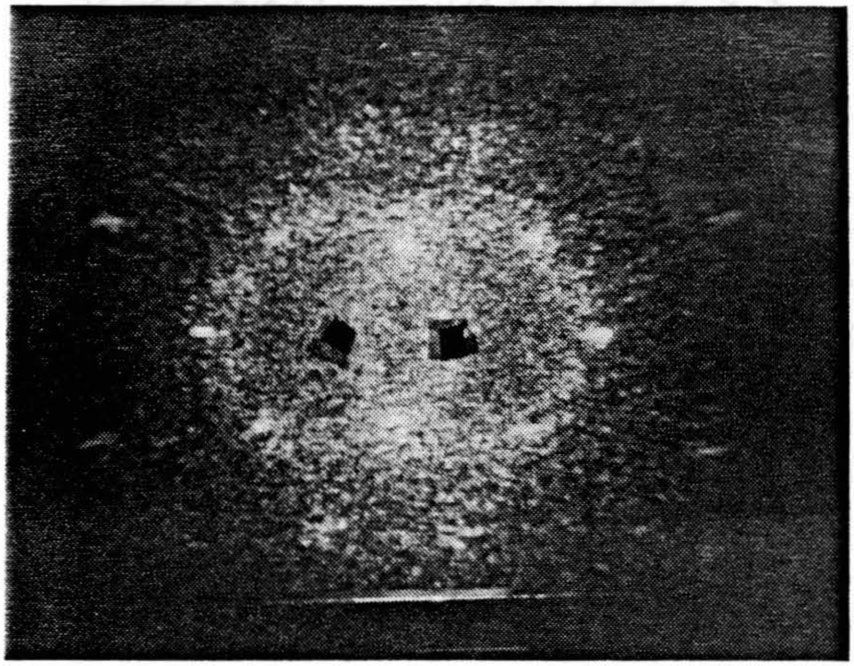

Figure 36a. Self-Diffraction Pattern. The Average Particle Separation is 2.5 um, the Fringe Spacing is 2.17 um and the Two Main Beams are blocked by Beam Stops in this Figure

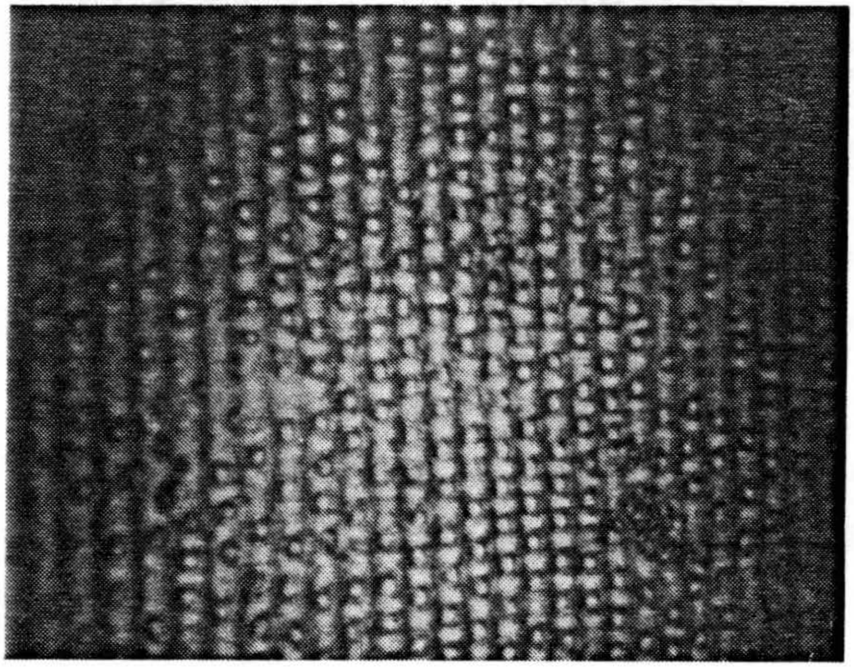

Figure 36b. Real Space Image of Corresponding to the Diffraction pattern in Figure 36a

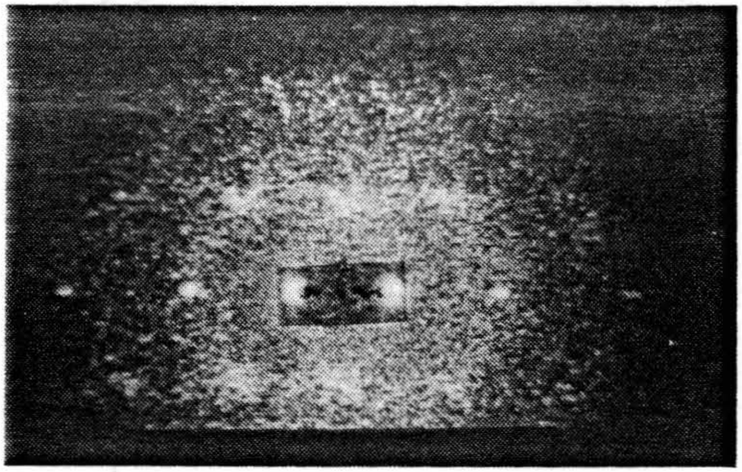

Figure 37a. Self-Diffraction Pattern. The Average Particle Separation is 2.5 um, the Fringe Spacing is 2.45 um and the Two Central Bright Spots Partially blocked by Tape are the Emerging main Beams

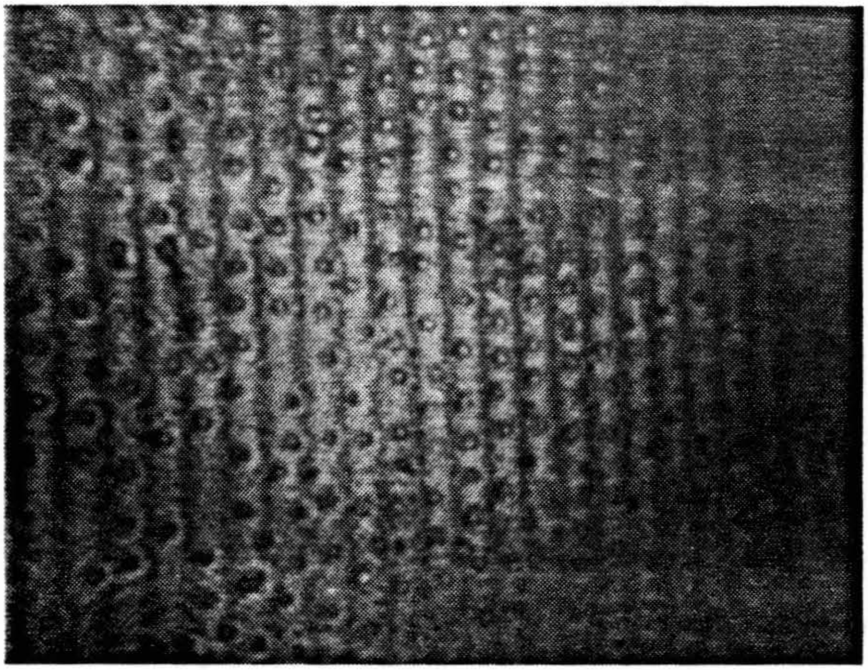

Figure 37b. Real Space Image of Corresponding to the Diffraction pattern in Figure 37a

When the fringe separation increased, the fundamental diffracted maxima appeared just outside the Debye-Sherrer ring and the other secondary maxima stayed near the Debye-Scherrer ring with unequal angular separation between them (see figure 36a). The angular separation between the fundamental and secondary increased to more than 45°degrees but less than 60°degrees. Since the angle of scattering and angular separaton are known, the line separation and the orientation are determined. This distorted hexagonal close pack structue is similar to a two dimensional tetragonal body centered lattice. Using Bragg's equation ($1/(d(kh))^2 = (h/a)^2 + (k/b)^2$) and applying the scattering condition for two dimensional body centered lattice, (2D-bcl) that the sum of the Miller indices must be even, we find the first two diffracted spots from the fundamental density mode corresponds to scattering from [20] lines. The lattice constant, (a = 4.4E-6 um) is found to be twice the size of the fringe separation (d = 2.2E-6 um). The other diffracted spots from secondary registration corresponds to the scattering from [11] lines. The lattice constant a (= 4.4E-6 um) is not equal to b (= 2.3E-6 um). The diffracted maxima from third order registration is diffuse.

It is also observed that for the fringe separation, $d = \bar{a}\{ 1 - (1/4)\}^{1/2} = 0.866\bar{a}$, then the micro-crystal becomes exactly hexagonal close pack. The fundamental diffracted maxima appear just outside the Debye-Sherrer ring as does the secondary maxima. This is shown in the figure 37a. Using

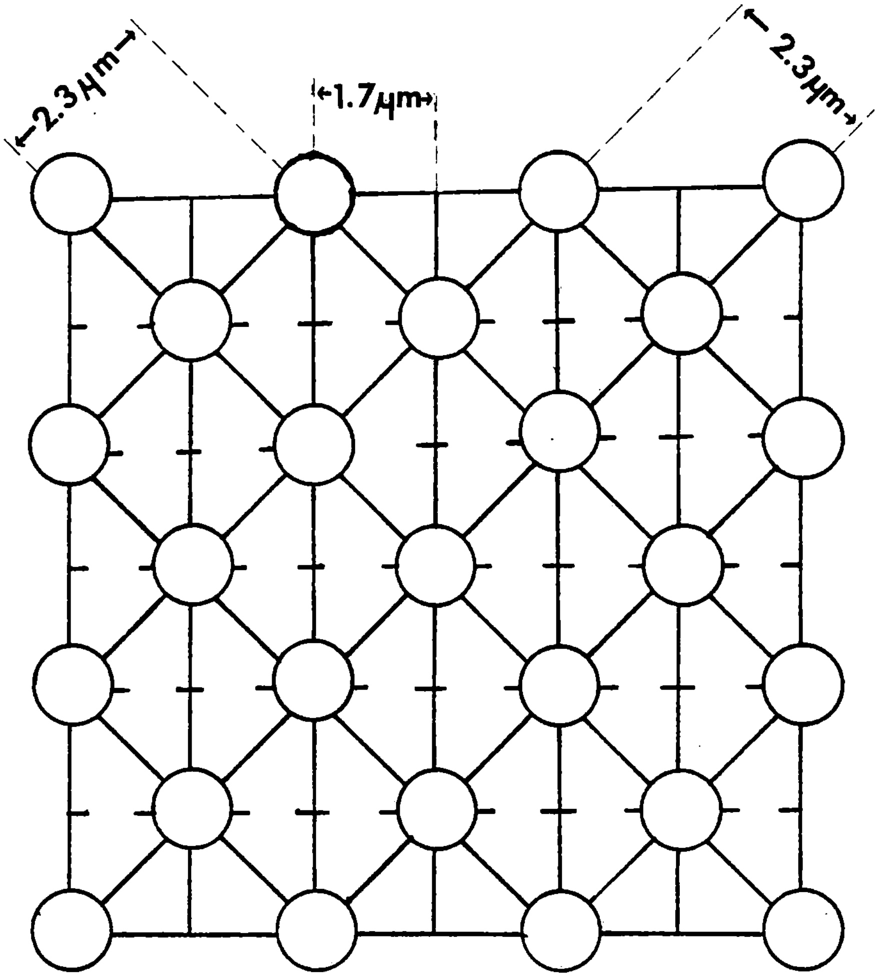

Figure 35c. Two Dimensional Square Lattice
Packing Fraction is .11

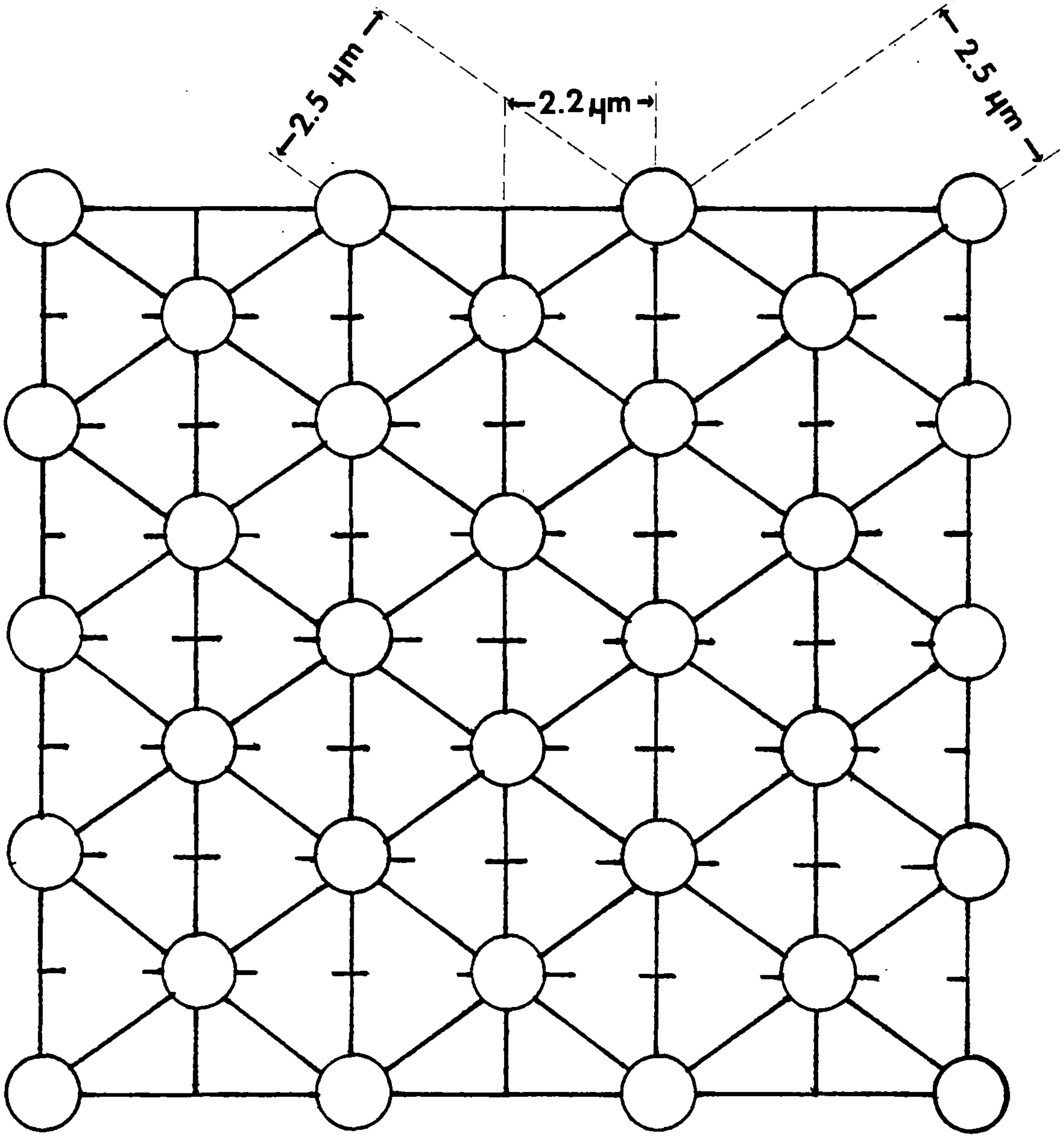

Figure 36c. Two Dimensional Distorted Hexagonal Lattice. Packing Fraction is .105

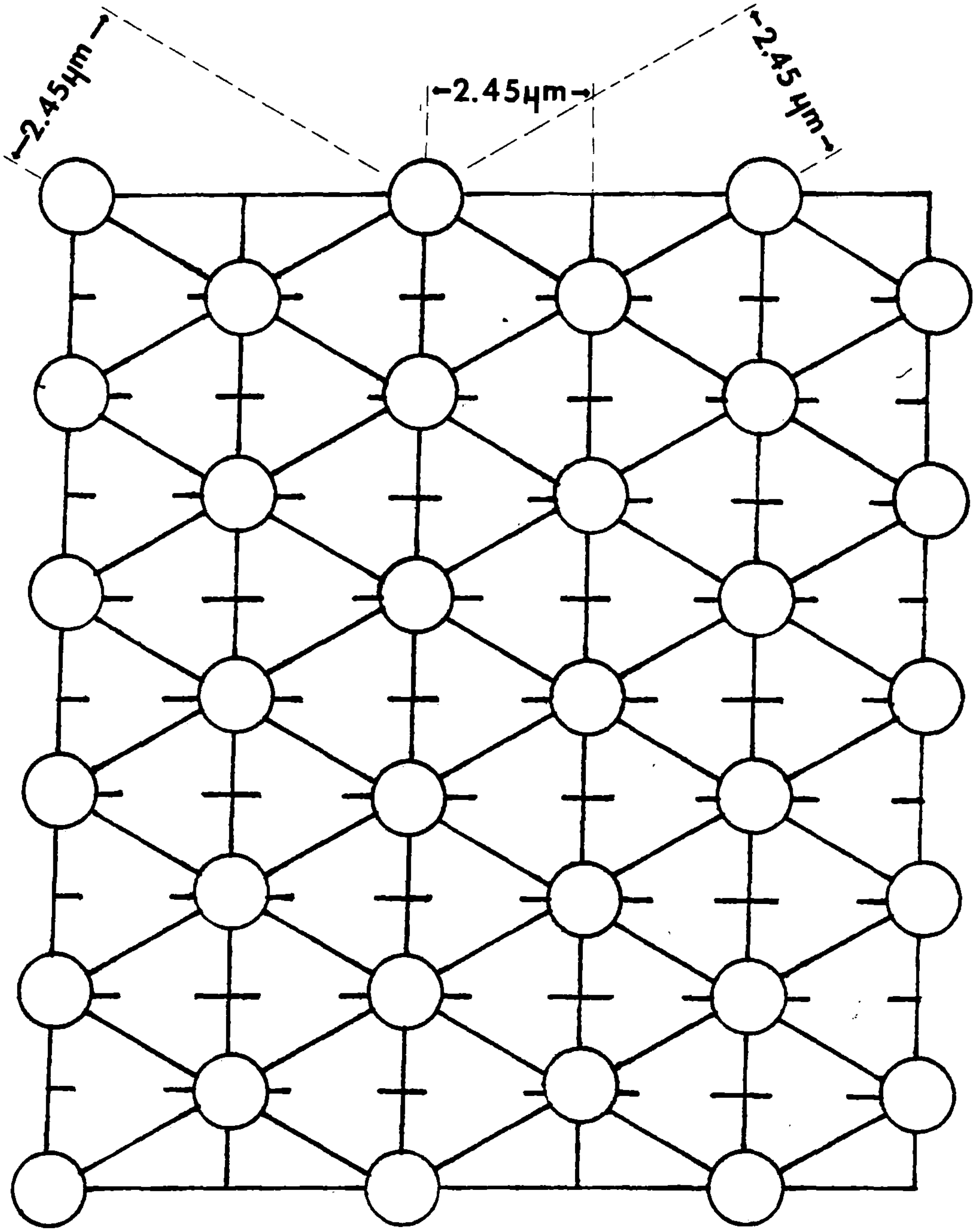

Figure 37c. Two Dimensional Hexagonal Lattice.
Packing Fraction is .105

Bragg's equation $\{ 1/(d(hk))^2 = (4/3)[(h^2 + hk + k^2)/a^2]\}$ from Chapter II and applying the condition that the sum of the Miller indices must be an integer, the lattice constant (a = 2.5*E-6 um) was obtained which is the average particle separaton as shown in figure 37c. The diffracted maxima from higher order registarion was also observed.

The nice feature of his experiment is that we not only make a phase change from liquid to hexagonal solid but also from liquid to cubic and destorted hexagonal structures directly. In other words by applying an external field, the liquid symmetry was broken; and by changing the period of the external field, the crystal symmetry can be broken. It is also possible to get the phase change from cubic to either of the distorted or perfect hexagonal structures (or vice versa) by changing the period of the external field.

Study of the Structure as a Function of Input Power

In the experiments on strongly interacting particle samples, the data are taken in two different ways. One method is the weighted average method as described in Chapter III, and the other method involves taking 1000 data points in some time interval and averaging them. It was found that both of these methods are in agreement with each other. The weighted average method works as a dynamic average where the signal growth can be monitored. On the other hand, when the structure is stable, then the 1000 data point method as well as weighted average method can be used.

The data presented here is for stable structures using the weighted average method. The data collections for both methods are reproduceable.

The sample cell gap is made wedge shaped to obtain a monolayer of particles as describe in Chapter III. The sample order is a liquid like or amorphous (having no long range order) in some regions and solid like in other regions. If the incident crossed beams are placed in those parts of the sample where the interacting particles exhibit short ranged order and near regions where the gap spacing excludes all particles (a colloidal vaccum), then a stable structure can be obtained using radiation pressure. This allows us to take the data for any period of time and to average the data. On the other hand, if the crossed beams are placed in a regions with larger gap spacings, then many particles are drawn into the crossed beams region and the spheres evidently try to form three dimensional structures. The signal for the fundamental diffracted maxima is observed to grow to a maximum before decreasing to lower values. At the same time the secondary diffracted maxima are also observed to grow to a maximum before decreasing to lower values. A typical plot of intensity as a function of time shows this effect in figure 38a and figure 38b for fundamental and secondary maxima, respectively. The open and solid circles represent two different input power and the bars represent the signal fluctuation (given by equation (3.6)). The peak value of the intensity for fundamental and

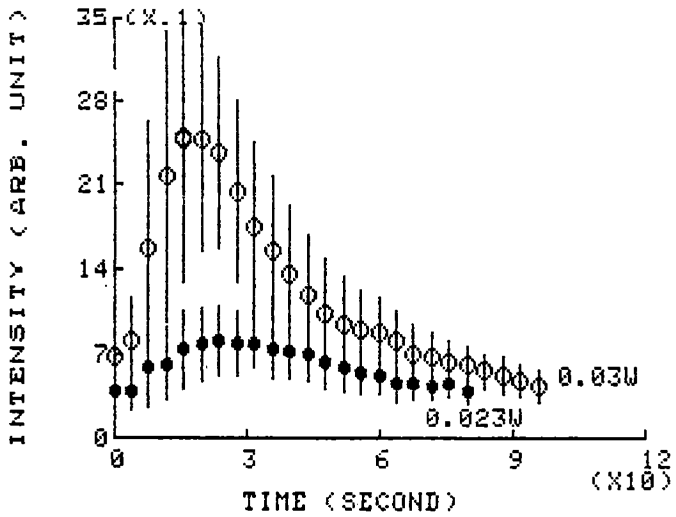

Figure 38a. Typical Behavior of the Fundamental Mode for a Non-Stable Sample. Open and Solid Circles Respect Two Different Input Powers of the Crossed Beams and the Bar Represent Fluctuations

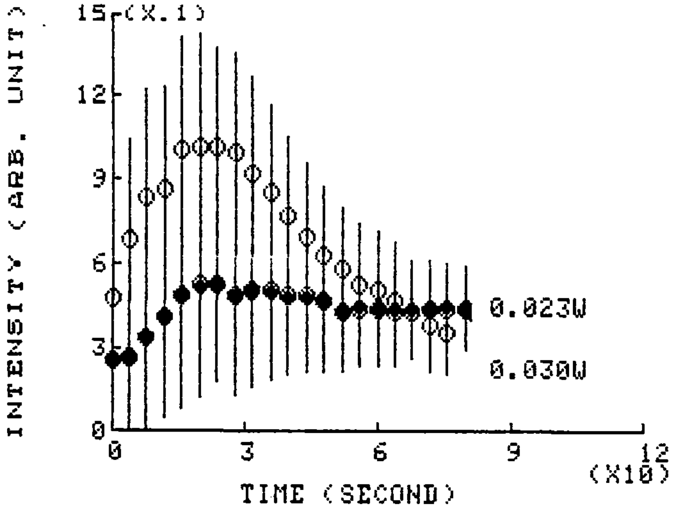

Figure 38b. Typical Behavior of the Secondary Mode for a Non-Stable Sample. Open and Solid Circles Respect Two Different Input Powers of the Crossed Beams and the Bar Represent Fluctuations

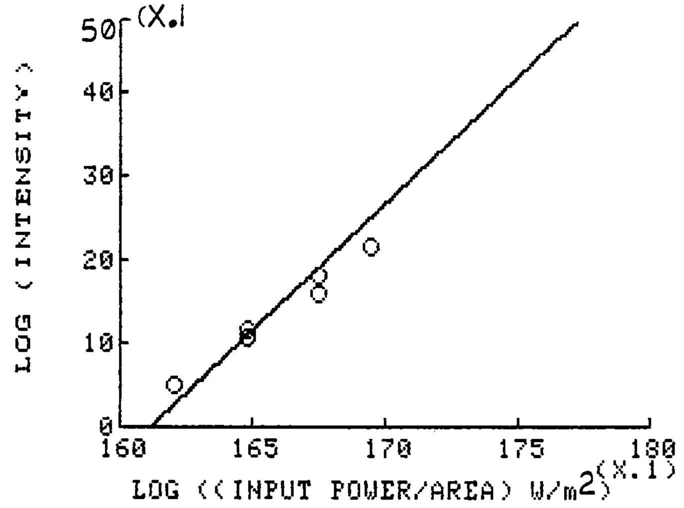

Figure 39a. A Plot of the Self-Diffracted Intensity from the Fundamental Mode vs Input Power per Unit Area. The Open Circles Represents a Stable Condition of the Sample. The Solid line is Cubic fit to Data and the Fringe Spacing is 3.2 um.

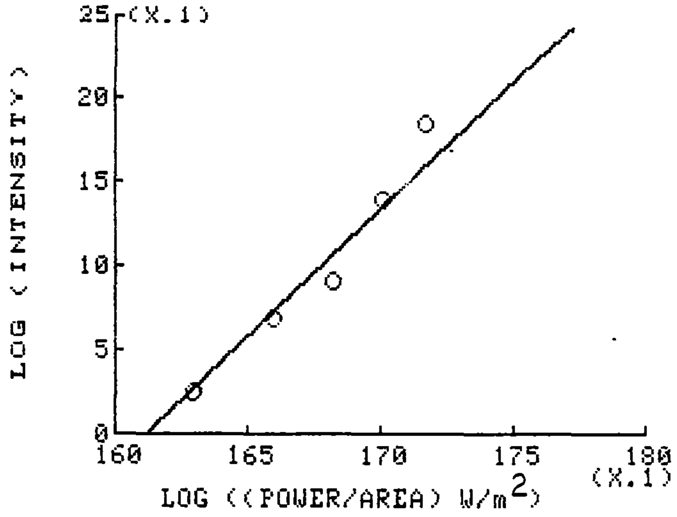

Figure 39b. A Plot of the Self-Diffracted Intensity from the Secondary Mode vs Input Power per Unit Area. The Open Circles Represent a Stable Condition of the Sample. The Solid Line is Three-Half Fit to Data and the Fringe Spacing is 3.2 um.

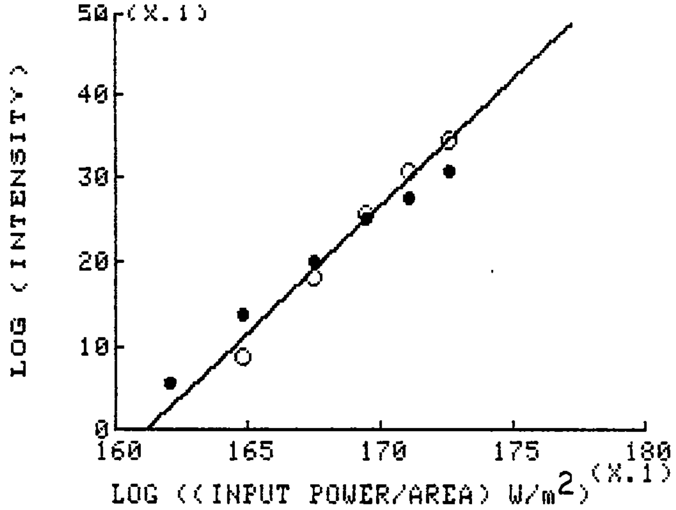

Figure 40a. A Plot of Self-Diffracted Intensity from the Fundamental Mode vs Input Power per Unit Area. The Open and Solid Circles Represent Stable and Non-Stable Sample Respectively. The Solid Line is Cubic Fit to Data and the Fringe Spacing is 2.63 um

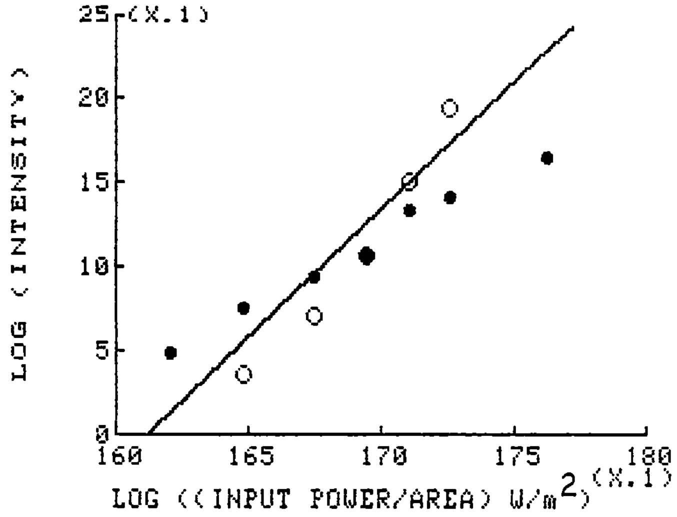

Figure 40b. A Plot of Self-Diffracted Intensity from the Secondary Mode vs Input Power per Unit Area. The Open and Solid Circles Represent Stable and Non-Stable Sample Respectively. The Solid Line is Three-Half Fit to Data and the Fringe Spacing is 2.63 um

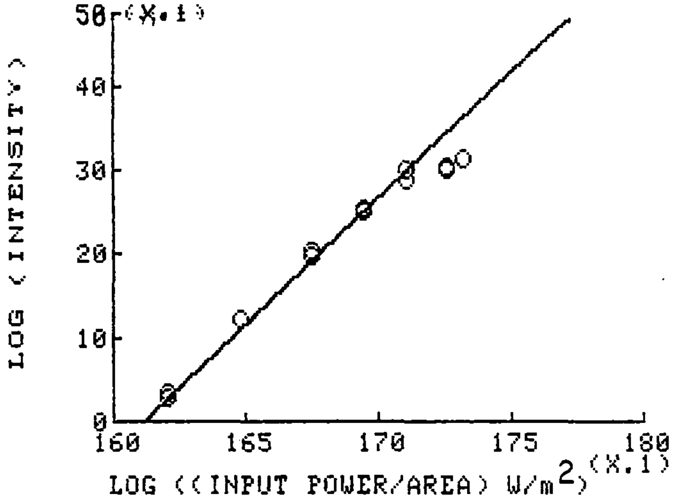

Figure 41a. A Plot of Self-Diffracted Intensity from the Fundamental Mode vs Input Power per Unit Area. The Open and Solid Circles Represent Stable and Non-Stable Sample Respectively. The Solid Line is Cubic Fit to Data and the Fringe Spacing is 2.17 um

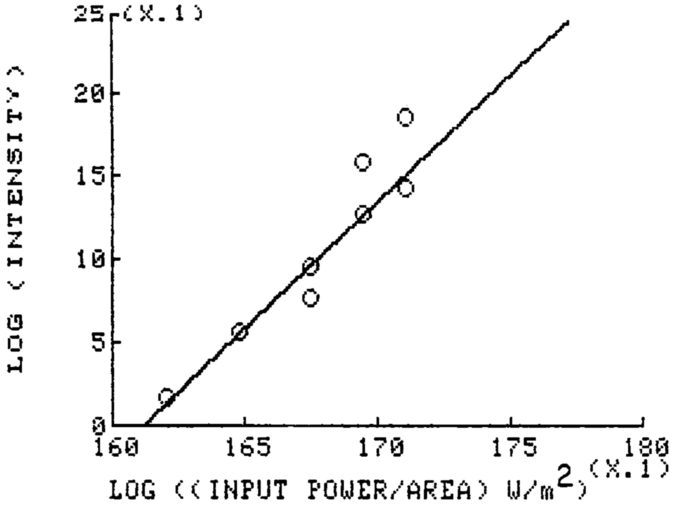

Figure 41b. A Plot of Self-Diffracted Intensity from the Secondary Mode vs Input Power per Unit Area. The Open and Solid Circles Represent Stable and Non-Stable Sample Respectively. The Solid Line is Three-Half Fit to Data and the Fringe Spacing is 2.17 um

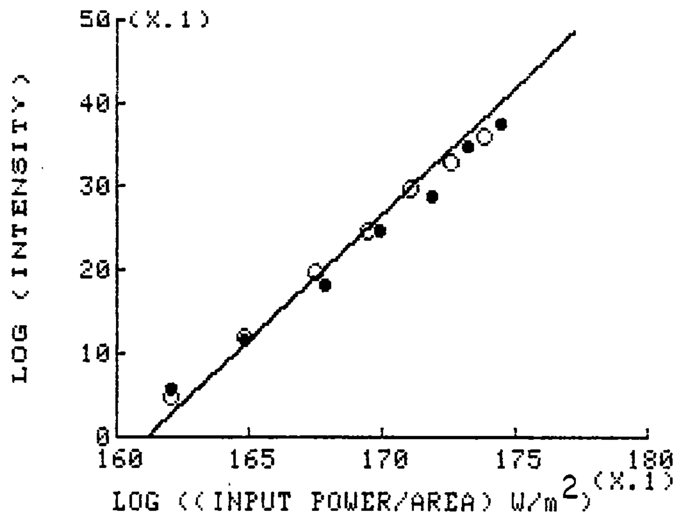

Figure 42a. A Plot of Self-Diffracted Intensity from the Fundamental Mode vs Input Power per Unit Area. The Open and Solid Circles Represent Stable and Non-Stable Sample Respectively. The Solid Line is Cubic Fit to Data and the Fringe Spacing is 2.04 um

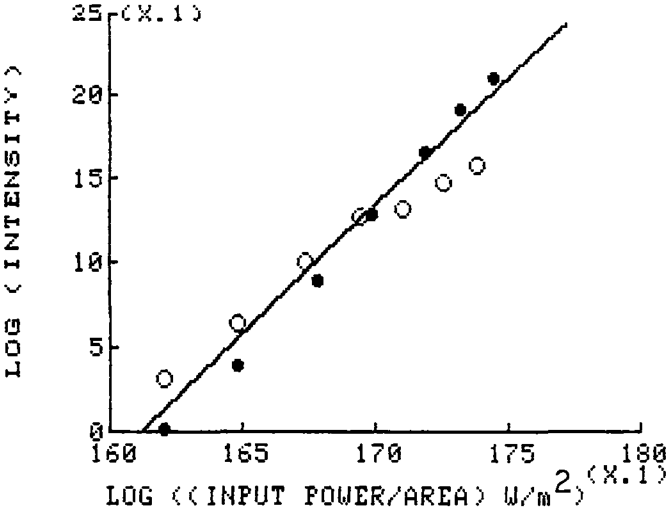

Figure 42b. A Plot of Self-Diffracted Intensity from the Secondary Mode vs Input Power per Unit Area. The Open and Solid Circles Represent Stable and Non-Stable Sample Respectively. The Solid Line is Three-Half Fit to Data and the Fringe Spacing is 2.04 um

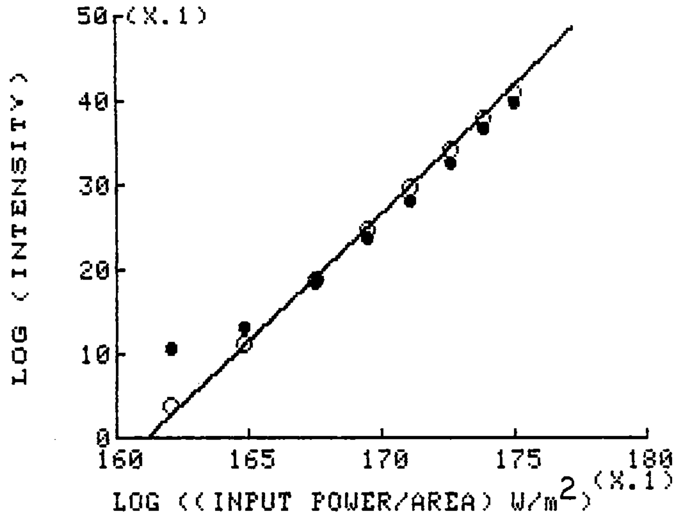

Figure 43a. A Plot of Self-Diffracted Intensity from the Fundamental Mode vs Input Power per Unit Area. The Open and Solid Circles Represent Stable and Non-Stable Sample Respectively. The Solid Line is Cubic Fit to Data and the Fringe Spacing is 1.77 um

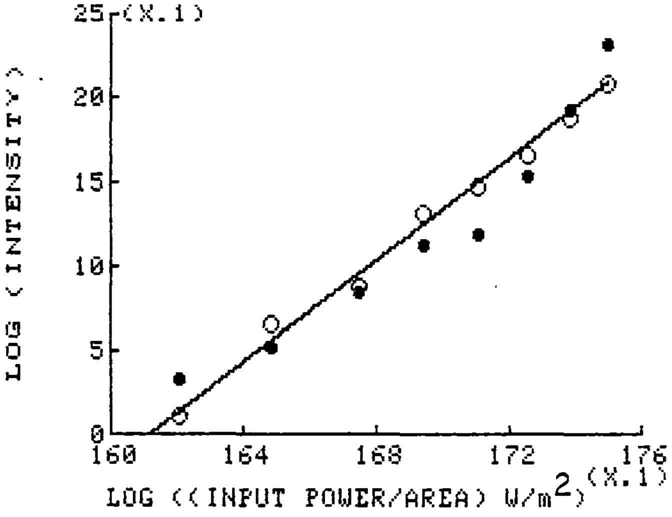

Figure 43b. A Plot of Self-Diffracted Intensity from the Secondary Mode vs Input Power per Unit Area. The Open and Solid Circles Represent Stable and Non-Stable Sample Respectively. The Solid Line is Three-Half Fit to Data and the Fringe Spacing is 1.77 um

secondary maxima were determined and plotted as a function of input power per unit area for five different crossing angles. These results are shown with solid symbol in figure 39a to figure 43a for the fundamental diffracted maxima and for the secondary diffracted maxima in figure 39b to figure 43b. The data for stable condition of the sample are also shown in there figures with open symbol. The solid lines are a cubic power law fit for the fundamental maxima and three halves power law fit for the secondary maxima. It is seen that they are generally in agreement with one another and follow a cubic dependence and three half power depencence for the fundamental and secondary modes, respectively.

The scattered electric field from the fundamental density mode is directly proportional to the amplitude of the density modulation, which for non-interacting particles is proportional to the input intensity of the crossed beams. This was discussed in Chapter IV. Since the scattered intensity of the fundamenatal density mode is the absolute value square of the scattered electric field, it is proportional to the square of the input power of the crossed beams. Since the probing beam is one of the pump beams the intensity of the probe beam increases as the pump beam intensity increases. Hence the scattered intensity of the fundamental maxima is proportional to the cubic power of the pump beam intensity. This is true only in the low power region, because at high enough power these spheres will be essentially completely localized in the fringes. Further increases in incident power will not increase the order of the particle. Evidently the interactions are weak enough here, that particle interactions do not produce a significant deviation from the cubic law dependence.

Landau Theory

It has been shown that in the presence of the external intensity field, not only do we see the directly excited density modes, but also we see the indirectly excited (slaved) density modes as well. In order to discuss this mode coupling, a Landau theory was constructed. Let the number density of the spheres be described by

$$P(r) = P_0 + \sum_i a_i \cos(\bar{k}_i \cdot \bar{r}) + \text{Higher order terms} \quad (5.1)$$

where P_0 is the average number density of the spheres

and $a_i \cos(\bar{k}_i \cdot \bar{r})$ are the stimulated and slaved density variations of wave vectors $\bar{k}$.

In the fluid like phase the second term on the right hand side of equation (5.1) is zero [$a_i \cos(\bar{k}_i \cdot \bar{r}) = 0$]. Thus the coeffcients of this term can be used as the order parameters for the phase transitions from the disordered to the ordered phases. The free energy density of the system is assumed to have form

$$f = \sum_i A_i P^i \quad (5.2)$$

where we terminate at the 4th order term to form a standard 4th order theory (6). The free energy is found by integrating over space (50):

$$F = \int f \, d^3\bar{r} \tag{5.3}$$

and only the terms in which the sum of the wave vectors, k , is zero contribute to the result such that (6)

$$F = 2Aa_1 + B \sum_i a_i^2 + 2Ca_1 a_2 a_3 + D(\sum_i a_i^2)^2 + E(\sum_i a_i^4). \tag{5.4}$$

or equivalently

$$= 2Aa_1 + B\sum_i a_i^2 + 2Ca_1 a_2 a_3 + E\sum_i \sum_j (a_i^2 - a_j^2)^2/6 + (E/3 + D)(\sum_i a_i^2)^2 . \tag{5.5}$$

where (A,B,C,...) are phenomenological coefficients described below. The a_i (= 1 - 3) represent the amplitudes of density modes with wave vectors we take to be k1, k2 and k3 as indicated in (6), and shown in figure 44a. The experimentally observed structure was a quasi-long-range 2D-hcp structure which is approximated with the three (six complex) lowest-order modes given above. The first term in equation (5.4) represents the external field which couples only to the k1 mode and only to first order in a_1. The second term stabilizes the fluid state (a_i = 0) for sufficiently large value of B. The third term couples all the modes together and induces the observed (13,17) first-order freezing transition in the absence of the external fields. The last two terms equalize the mode amplitudes and stabilize the overall free energy. In this experiment only a single mode is directly stimulated by the external field, and we expect a_1 to differ from the degenerate modes a_2 , a_3 . From the experiment, we see that the other two indirectly excited modes are symmetric and equivalent, hence we can assume that $a_2 = a_3$. The state of the system is given by the values of a_i (a_1,a_2) which minimize the free energy F. For C = -1, D = 1/2, E = 3/2, the minimized result of F is found numercially and is shown in figure 44b as a function of A and B. As we see for A = 0 (no external field) all the density modes, a are equal and undergo a first-order phase transition from solid to a liquid as B is increased. On the other hand, if A is non zero, the directly excited mode, a is larger than indirectly excited mode, a in general. For sufficiently large B the transition from liquid to solid becomes a second-order phase change with $a_2 = a_3 \sim (A - Ao)^{1/2}$ for the initial change in the slaved modes from zero amplitude. This type of symmetry-changing transition can be second order, because the external field reduces the symmetry of the fluid before freezing occurs. Thus it would be possible to take a fluid system to a solid by a second-order process which involves externally applied fields, as indicated by the

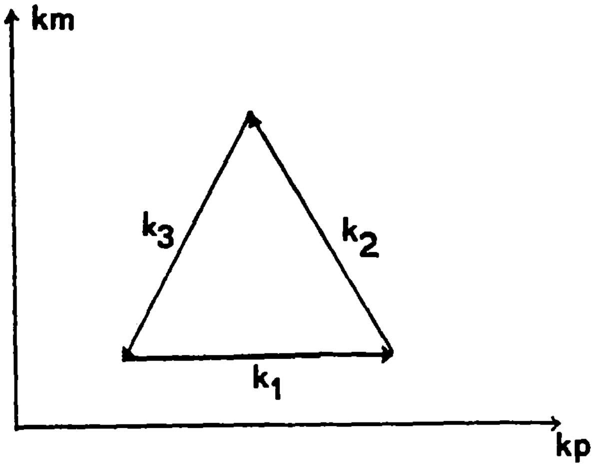

Figure 44a. The Crossed Beams Directly Excite a Density Mode with Wavevector K, and two other Modes with Wave-Vector K_2 and K_3 are Coupled to the K_1 Mode by Particle Interactions.

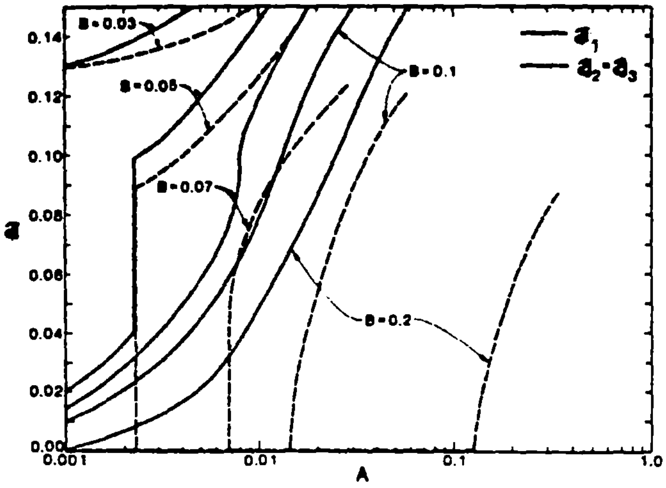

Source: A.Chowdhury and B.J.Ackerson, Laser-Induced Freezing, Phys. Rev. Lett., Vol.55, No.8, p835 (1985).

Figure 44b. Landau Theory for the Order Parameter a (Solid curves) and a =a (Dashed Curves) for C=-1, D=1/2 and E=3/2 as a Function of A and Parametrized by B.

continuous growth of the structure in our experiment. Our experimental results indicate both solid and liquid phases can exist as described by the Landau theory. When an external field is applied the fundamental mode (a_1) is stimulated and grows faster than the slaved (secondary) modes (a_2) as indicated by the Landau theory. The agreement is not quantitative. The experiments indicate a continuous change in intensity consistent with the behavior for large B values in the Landau theory. Again the agreement is not quantitative. Spatial fluctuations, which are not included in the Landau theory, may destroy the low amplitude behavior of a_2 and a_3.

Study of the Intensity maxima as a function of Crossing Angles

The study of the scattered intensity from the diffraction grating (produced by crossed beams) was observed as a function of crossing angle in Chapter IV for non-interacting particles. There we observed that as the crossing angle increases the scattered intensity decreases. This is a form factor effect. This effect was corrected by using the Mie theory. But when a interacting sample is subjected to crossed beams and the crossing angle of the beam was varied, something different happens.

The intensity of the fundamental and secondary maxima was studied for different crossing angles. Two pin diodes were positioned at the fundamental and secondary diffracted maxima respectively. The data was taken by the weighted average method. The intensity of the two pump beams was made the same and kept constant. The scattering angle of the liquid-like Debye-Scherrer ring was 7.4° degrees. It was observed that when the fringe separation, d, is equal to 0.87a, (the average particle separation) then the intensity of the fundamental diffracted maxima is maximum. If the fringe separation is increased or decreased from this point the intensity of the fundamental diffracted maxima decreased for fixed input power of 40E6 Watts/m^2 of the pump beam. This is shown in figure 45a with a solid line. The data is also corrected for the particle form factor using Mie Theory, assuming the scattering from each beam is equal and in phase (dash-dash line of figure 45a). There is no correction for the intensity potential due to finite particle size. (A rough calculation indicates this may increase the value at 12° degrees by a factor 2.5 compared to the 5° degrees, without destroying the maximum at 8° degrees).

A plot of intensity of the secondary diffracted maxima is shown in figure 45b for different crossing angles and for fixed input power of the pump beams. The maximum intensity of the secondary diffracted maxima was observed for a fringe separation d equal to 0.87a. If the crossing angle is decreased the intensity of the secondary diffracted maxima decreases rapidly to the intensity of the Debye-Scherrer ring. If the crossing angle is increased such that fringe separation is greater than particle diameter of the sphere then the intensity of the secondary diffracted maxima again decreases. Note that the secondary diffracted maxima always stays positioned near the Debye-Scherrer ring, only the angular position of this maxima changes as the crossing angle changes.

When the fringe separation, d, is increased or decreased from 0.87a, there exists a competition between fluid and soild phases and the structure goes from a "commensurate" to an "incommensurate" phase or vice versa. In particular, when the crossing angle is decreased from the commensurate crossing angle the intensity of the both maxima decreases. This is because the particles belonging to same fringe are strongly correlated but the correlation between particles of neighbouring fringes become weak as the fringe spacing increases. In this case the fluid phase dominates the system and only the weak registration with the applied intensity potential occurs. However, if the crossing angle is increased (still keeping the fringes larger than the particle diameter), the intensity of the maxima again decrease. In fact, in this condition there exists a strong correlation between particles of neighbouring fringes. However, the interparticle forces become strong enough to compete with the external potential registration force. The interparticle forces can dominate the external potential and the sample assumes a liquid like order. It was observed that the fundamental diffracted spot changed in shape from circular to eliptical as the crossing angle increased. This

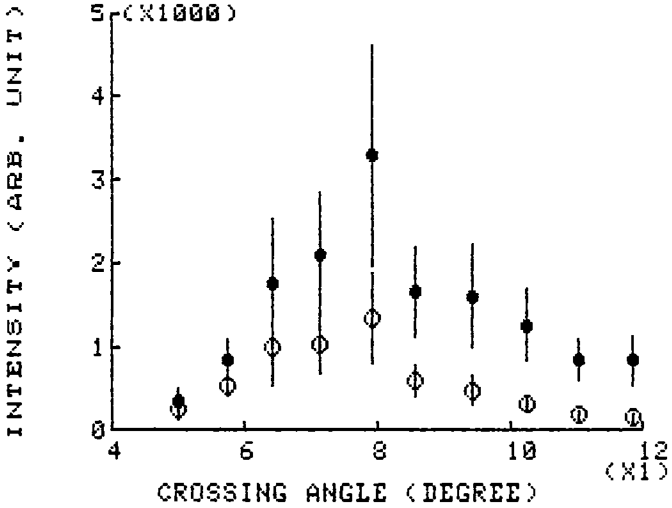

Figure 45a. Plot of Self-Diffracted Intensity of Fundamental Mode vs Crossing Angles. The Scattering Angle of the Debye-Scherrer Ring is 7.4 Degrees. The Particle Diameter is 0.95 um. The Open and Solid Circles Represents Data and Corrected Data Using Mie Theory, Respectively. The Bar Represents the Intensity Fluctuations

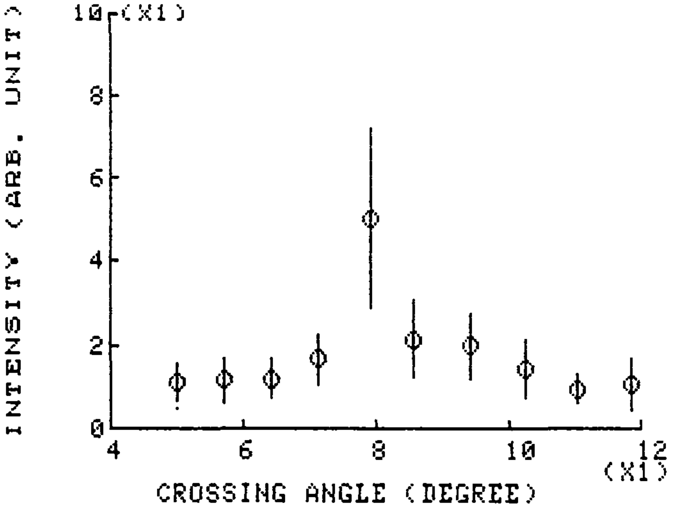

Figure 45b. Plot of Self-Diffracted Intensity of Secondary Mode vs Crossing Angles. The Scattering Angle of the Debye-Scherrer Ring is 7.4 Degrees. The Particle Diameter is 0.95 um. The Open Circles Represent Data and the Bar Represents Intensity Fluctuation

may indicate the transition from a commensurate to chaotic phase rather than to a liquid phase (40).

A Study of Intensity of the Debye-Scherrer Ring as a Function of the Write Beam Intensity

A study of the intensity of the liquid Debye-Scherrer ring at an anticorrelation position (a position midway between stimulated and slaved intensity maxima) was made on the commensurate structure. It was observed that as the intensity of the write beams were increased the scattered intensity of the Debye-Scherrer ring at an anticorrelation position decreases relative to the input intensity, as the scattered intensity of the fundamental and secondary maxima increase. This is shown in figure 46. This is not surprising because the dominance of the few density modes stimutaled by an external field comes at the expense of other modes in the same. These modes decrease in amplitude and scatter less light with increasing external field strength. This effect also corresponds to the development of anticorrelations in the CCIFS technique (3,4).

Time Dependent Study Of The Structure

The data for time dependent measurements were collected as described in Chapter III. When the beams are crossed in the interacting sample, the liquid symmetry is broken. This allows the growth of a solid structure which is monitored by the growth of the diffracted intensity. The growth of the

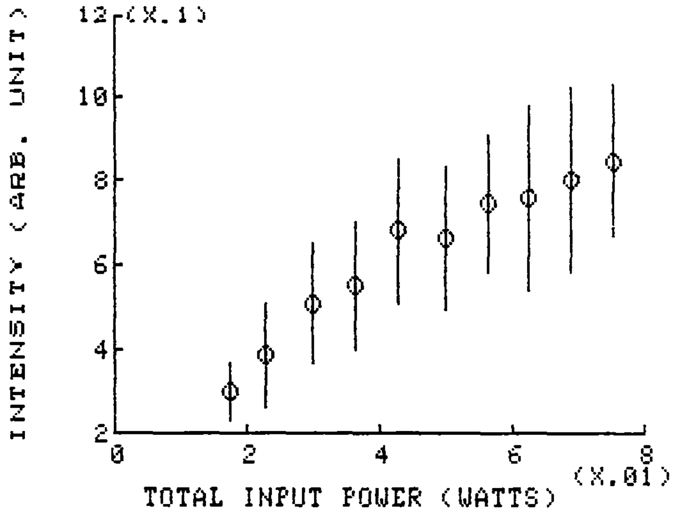

Figure 46. Plot of Intensity of Debye-Scherrer Ring vs Input Power. The Scattering Angles is 7.4 Degrees. The Particle Diameter is 0.95 um. The Open Circles and Bar Represents Data and Fluctuations

structure is dependent on the strength of the interaction between the particles and strength of the applied external periodic potential. One of the pump beams is then blocked periodically by the chopper. It was observed that as the write beams were blocked, the sample lost its solid symmetry. The scattered intensity slowly diminished which is the indication of the decay of the structure. The growth and decay of the fundamental and secondary maximas are studied and given in figures 47a,48a & 49a and figure 50a, respectively.

Study of the Growth of the Fundamental Mode

Plots of the intensity of the fundamental diffracted maxima as a function of time are shown in figures 47a, 48a and 49a for a total input power 22E6 W/m^2, a wavelength of 488 nm and three crossing angles 11°, 9.6° and 8° degrees respectively. As in Chapter IV, we expect the growth of these density modes to be dependent on the input power of the pump beam, the crossing angle, the strength of the interaction of the particles and the viscosity of the suspended medium. In this case the scattering angle of Debye-Scherrer ring is 8.5° degrees. It is observed that the structure grows faster when the fringe separation d approches 0.87a. On the other hand if the crossing angle is increased or decreased from this point then competion between the interparticle forces and the external field increases the growth time.

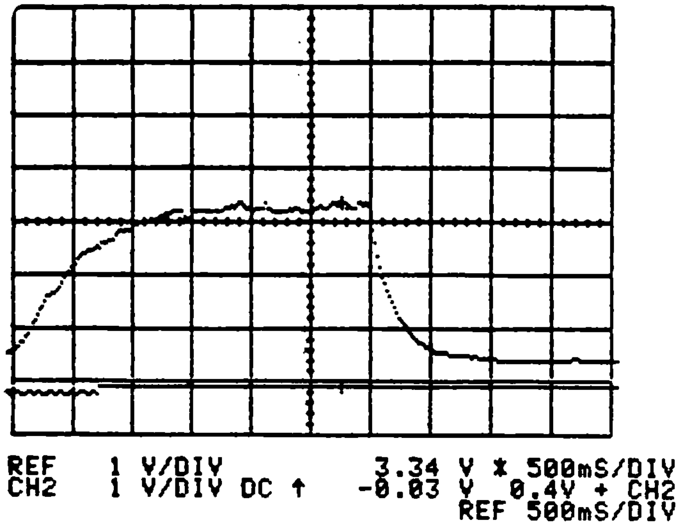

Figure 47a. Growth and Decay of Fundamental Mode. The Particle Diameter is 0.95 um. The Average Particle Separation is 2.7 um. The Fringe Spacing is 2.63 um. The Input Power is 0.024 Watts and 250 Frames are Averaged

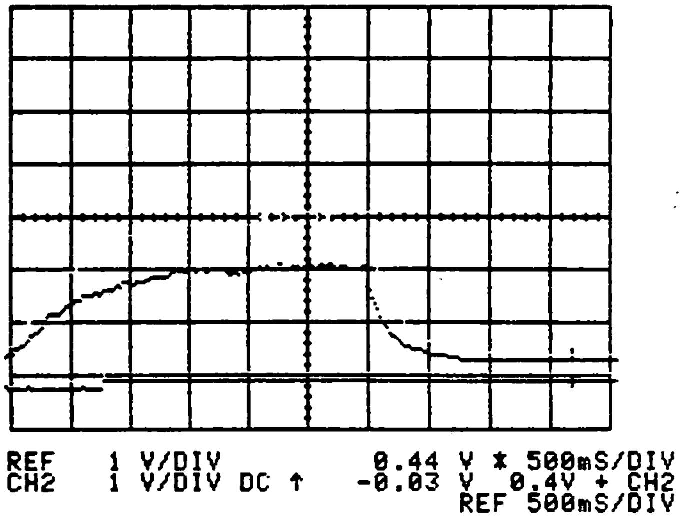

Figure 48a. Growth and Decay of Fundamental Mode. The Particle Diameter is 0.95 um. The Average Particle Separation is 2.7 um. The Fringe Spacing is 2.17 um. The Input Power is 0.025 Watts and 250 Frames are Averaged

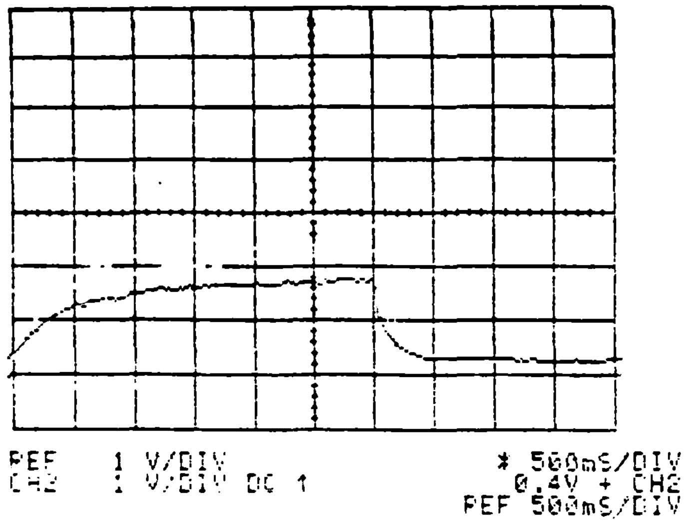

Figure 49a. Growth and Decay of Fundamental Mode. The Particle Diameter is 0.95 um. The Average Particle Separation is 2.7 um. The Fringe Spacing is 1.89 um. The Input Power is 0.039 Watts and 250 Frames are Averaged

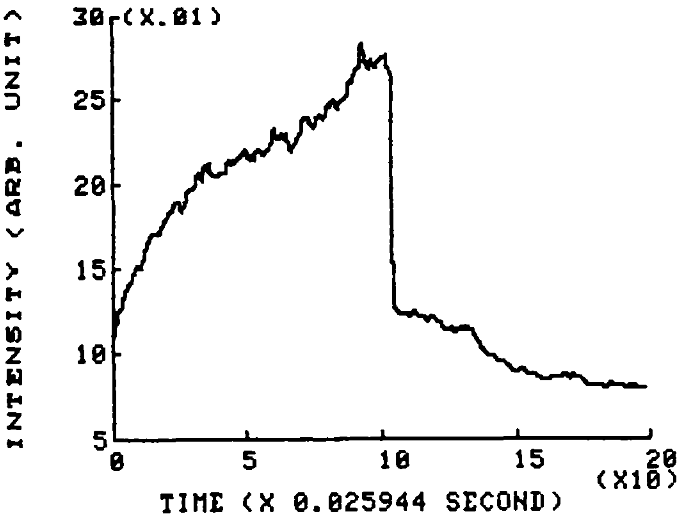

Figure 50. Growth and Decay of Secondary Mode. The Particle Diameter is 0.95 um. The Average Particle Separation is 2.7 um. The Fringe Spacing is 2.17 um. The Input Power is 0.05 Watts and 221 Frames are Averaged

The data for the initial growth of the fundamental density mode is fitted to equation (4.34) with the assumption that coherently scattering background B is zero, is extracted from the incoherent background and the scattered electric field, E(t), is assumed to be given by

$$E(t) = 1 - \exp(-t/Tf) \qquad (5.6)$$

Here Tf is the formation time constant. A plot of the log of E(t) as a function time is shown in figures 47b, 48b and 47b for three different crossing angles. The value of the (1/Tf) along with input power and crossing angles are listed in Table V.

The growth of the density modes is dependent on the strength of the interparticle interaction and external periodic potential as discussed earlier. Let us assume that free diffusion coefficient is related to this transition time via a function which is dependent on the input power and the strength of the interaction

$$Dok^2 Tf = C \qquad (5.7)$$

where C is a function of the strength of the particle interaction and of the applied field

Do is the free diffussion constant

and k is the scattered wave vector.

The values of the C's are also listed on Table V. It is observed that as the power increased the C's decreased. In other words, it takes less time to form this structure. It can also be seen that when the fringe separation is 0.87a (average particle separation) then the structure grows faster. Our results are very tentative and need to be further studied for different input powers.

Decay of the Fundamental Mode

When one of the write beams is blocked, the structure decays. But this decay is different from the decay in the non-interacting samples. It was found that the decay is not a single exponential. It was also observed that when one of the write beams is blocked the structure sometimes stays frozen for about 30 msec which we refer to as the "free induction time" for nucleation of the liquid phase. This type of free induction time has been observed in a computer simulation experiment by Hess (52). Immediately after this free induction decay the structure decays non-exponentialy. The data for the decay after the free induction period for three different crossing angles is fitted to equation (4.34) with the assumption that B is zero, that the incoherent background γ is extracted from the data at large times and that the scattered electric field, E(t) given by

$$E(t) = \sum_i \exp(-t/Ti) \tag{5.8}$$

where Ti's are the relaxation times.

TABLE V

COMPARISON OF INITIAL FORMATION TIME CONSTANT OF FUNDAMENTAL MODE OF INTERACTING PARTICLES TO FREE RELAXATION TIME OF SAME NON-INTERACTING PARTICLES FOR THREE DIFFERENT FRINGE SPACING

Diameter of the spheres = 0.95 + 0.05 um
Scattering angle of Debye-Scherrer ring = 7.9° + 0.4°

Fringe Spacing in um	Total Input Power in Watts	Initial Formation Time Constant in sec.	Ratio C = (Tf/Td)
1.89E-6	0.039	0.34 + 0.04	1.7 + .2
1.89E-6	0.050	0.27 + 0.04	1.4 + .2
2.17E-6	0.027	0.43 + 0.05	1.6 + .2
2.17E-6	0.037	0.36 + 0.05	1.4 + .2
2.63E-6	0.025	0.39 + 0.03	1.0 + .2

Self-diffracted 1st order maxima, Temperature 20° C

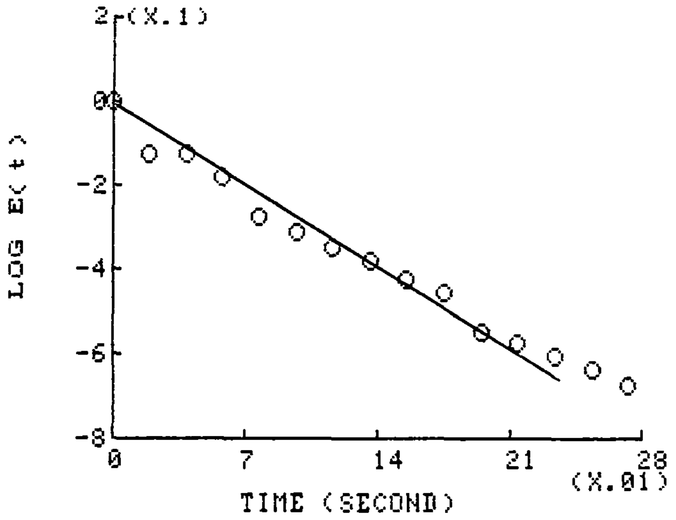

Figure 47b. Initial Growth of Fundamental Mode. The Particle Diameter is 0.95 um, the Average Particle Separation is 2.7 um, the Fringe Separation is 2.63 um, Input Power is 0.024 Watts and a 250 Frames Average is Performed

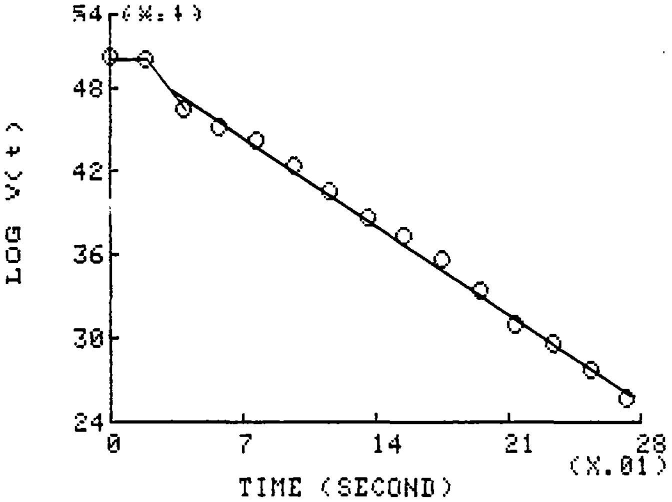

Figure 47c. Decay of Fundamental Mode. The Particle Diameter is 0.95 um, the Average Particle Separation is 2.7 um, the Fringe Separation is 2.63 um, Input Power is 0.024 Watts and a 250 Frames Average is Performed

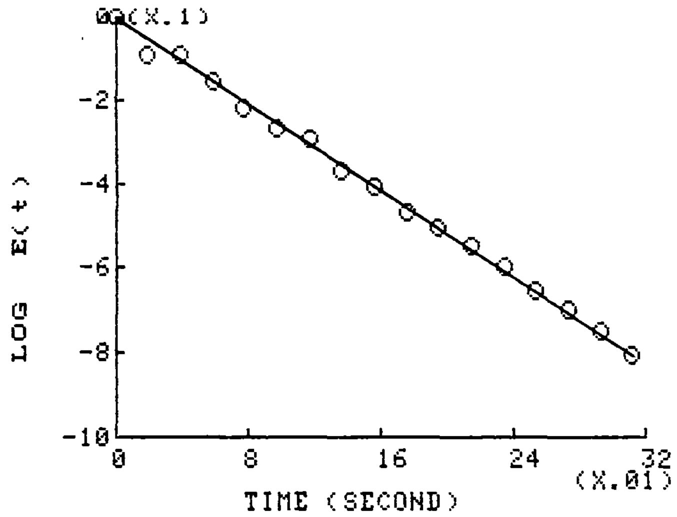

Figure 48b. Initial Growth of Fundamental Mode. The Particle Diameter is 0.95 um, the Average Particle Separation is 2.7 um, the Fringe Separation is 2.17 um, Input Power is 0.025 Watts and a 250 Frames Average is Performed

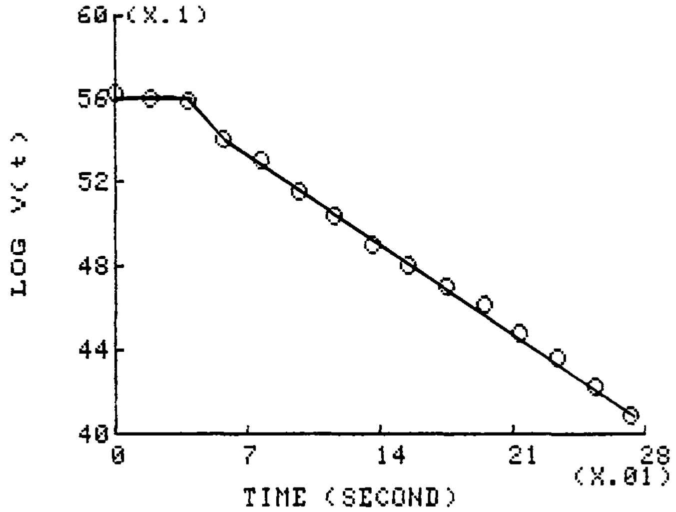

Figure 48c. Decay of Fundamental Mode. The Particle Diameter is 0.95 um, the Average Particle Separation is 2.7 um, the Fringe Separation is 2.17 um, Input Power is 0.025 Watts and a 250 Frames Average is Performed

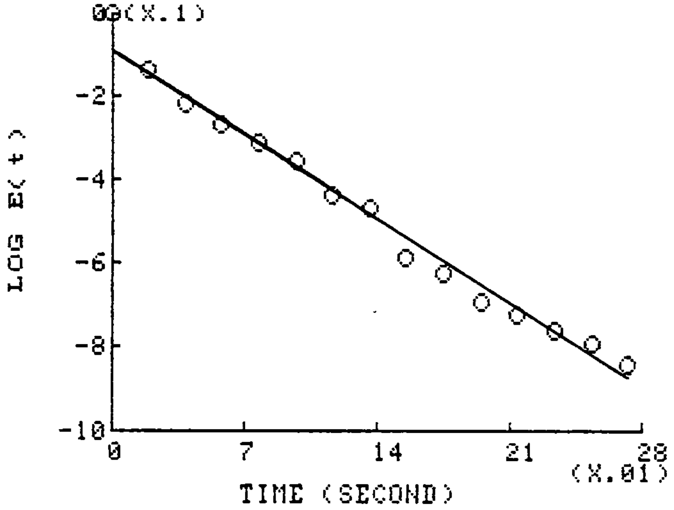

Figure 49b. Initial Growth of Fundamental Mode. The Particle Diameter is 0.95 um, the Average Particle Separation is 2.7 um, the Fringe Separation is 1.89 um, Input Power is 0.039 Watts and a 250 Frames Average is Performed

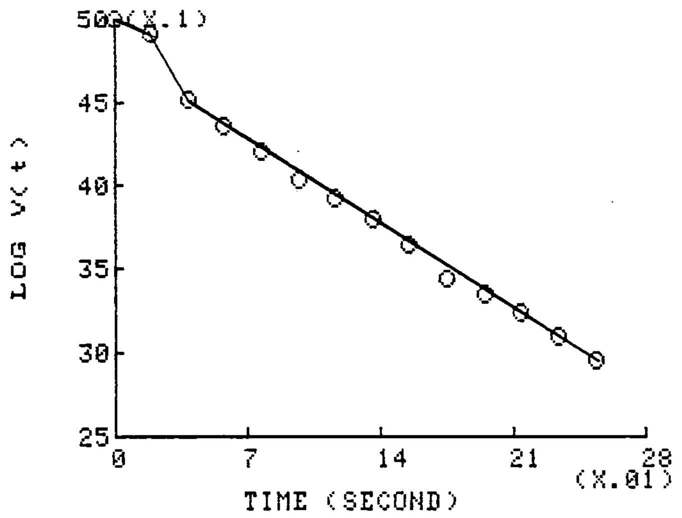

Figure 49c. Decay of Fundamental Mode. The Particle Diameter is 0.95 um, the Average Particle Separation is 2.7 um, the Fringe Separation is 1.89 um, Input Power is 0.039 Watts and a 250 Frames Average is Performed

A plot of log V(t), which is corrected as described above for the coherent and the incoherent background, as a function of time is shown in figure 47c, 48c and 49c for three different crossing angles. We found that first relaxation time constant is smaller than second relaxation time constant in general. In fact, after this free induction time the structure decays rapidly to a metaliquid state followed by a slow decay to liquid state. The value of the (1/Ti)'s are shown in Table VI along with input power and fringe separation. Here we observed that the quasi-solid structure transfer to a liquid state continuously.

We have discussed in Chapter IV that the radiation pressure moved the spheres near the down stream wall resulting in an extra hydrodynamic friction which slows the diffusion process. To see the hydrodynamic effect of the wall and the strength of interaction between particles in this process, we assume that

$$Dok^2T = C' \tag{5.9}$$

where C' is relaxation time divided by the free diffusion time at the same k vector

Do is the free diffusion constant

k is the scattered wave vector.

The values of the constant C's are listed in Table VI. The initial decay of the structure is faster than free diffusion even with wall effects present. This gives an

TABLE VI

COMPARISON OF RELAXATION TIME CONSTANTS OF FUNDAMENTAL MODE OF INTERACTING PARTICLES TO FREE RELAXATION TIME OF SAME NON-INTERACTING PARTICLES FOR THREE DIFFERENT FRINGE SPACING

Diameter of the spheres = 0.95 + 0.05 um
Scattering angle of Debye-Sherrer ring = 7.9° + 0.4°

Fringe Spacing in um	Total Input Power in Watts	Ratio of (T1/Td)	Ratio (T2/Td)
1.89E-6	0.039	0.48 + 0.03	1.2 + .2
1.89E-6	0.050	0.64 + 0.04	1.4 + .2
2.17E-6	0.027	0.56 + 0.04	1.1 + .1
2.17E-6	0.037	0.65 + 0.05	1.0 + .2
2.63E-6	0.025	0.53 + 0.02	.88 + .2

Self-diffracted 1st order maxima, Temperature 20° C indication that the structure breaks the symmetry of solid very fast. The following decay is approximately two times slower than the first. This tells us that the sample is slowly getting its liquid symmetry. If the wall effect could somehow be neglected, then the structure would probably decay faster. However, this later decay is slower than the free diffusion decay and is consistent with the slow decay observed in the interacting system near the peak intensity in the structure factor (53).

Study of the Growth and Decay of the Secondary Mode

We have seen that in these experiments the applied external field breaks the liquid symmetry and the solid structure grows continuously. In the previous two sections and last two sections of Chapter IV, we studied the growth and decay of the density mode which is directly induced by the external field. Here we will study the growth and decay of the density modes which are not directly induced by the field, the modes which give a clear indication of the solid symmetry.

If the intensity potential is adiusted to be 0.87 times the average particle separation, then the Bragg scattering from the secondary modes appear near or just outside the Debye-Scherrer ring. This makes it very hard to interpret data for the growth and decay of this density mode. As the secondary mode starts growing the Debye-Scherrer ring background diminishes. Also, in a self scattering mode both the write beams are used as probe beams. When the field is turn off by means of blocking one beam, then the contribution of this beam to the scattering is also eliminated and a large decrease in the scattered intensity of secondary Bragg spots is observed. This can be inferred from figure 50. Also in the growth of the secondary mode, a small jump in the scattering intensity of the Bragg spots was observed over the background, immediately when both crossed beams are turned on. Both of these effects are due to the fact that scattering by the write beam (1) is adding coherently to the scattering by the write beam (2). This jump in intensity is less than 25% of the maximum scattered intensity in the growth case. The particle form factor is very important analyzing these results, because the incident light wavelength is approximately equal to the radius of the sphere. Hence the scattering intensity will in general be less as the angle increases from the forward direction. Furthermore the scattered intensity of the other write beam (2) will contribute to the intensity at that point as higher order modes exist which will scatter in this direction, as they are formed.

Each probe beam produces four lowest order slaved mode diffracted spots near the Debye-Scherrer ring as a result of the induced first order mode. But in the picture figure 35a, 36a and 37a only six diffracted spots are visible instead of eight diffracted spots. However, the diffracted spots which are sitting in the middle above and below the write beam plane are a combination or superposition of diffracted spots from each incident beam. The observed growth is non-exponential. The order of the formation time constant is similar to that of the fundamental modes which is listed in Table V. The growth of this mode is dependent on the strength of the interaction and the spacing of the periodic intensity potential. The growth of this secondary density mode clearly indicates the growth of the solid from liquid continuously.

The decay of this indirectly induced mode (secondary density mode) is also interesting to study. When one of the write beams is blocked, then there is a sharp fall in the scattered intensity. This is due in part to the coherent mixing of the two write beams which changes when one of the write beams is eliminated. This contribution is less than 25% of the total intensity based on the jump in the intensity seen when both beams are turned on. If we subtract this number from data though, we still see a rapid decay followed by a slow decay. This rapid decay is so fast that it happens within 50 msec. This faster decay can not be interpreted through this data. This is because the write beam (2) is chopped by a blade connected to a motor. The revolution of the motor was one revolution per second. The width of the laser beam is 1.25 mm. Hence there is finite time to choped the beam completely. The chopping of this beam sends a triggering signal to the computer. The time it takes to chopped the beam completely is about 60 msec. Hence the initial decay is in the limit of the chopping rate. If we chopped the beam at a faster rate then we lose information of the mode formation. Since the secondary mode became distint at long times. Considering all of this we find that we are restricted by the apparatus to do any further detailed study of the sample.

CHAPTER VI

DISCUSSION, CONCLUSIONS AND SUGGESTIONS FOR FUTURE WORK

Discussion and Conclusions

The statistical behavior of dilute colloidal non-interacting and interacting samples are studied in the presence of two crossed laser beams. It was observed that if transparent dielectric spheres with a dielectric constant larger than the dielctric constant of the surrounding medium are subjected to a focused laser light, these spheres are moved into the high intensity regions and pushed to the down stream wall due to radiation pressure. However, when two laser beams are crossed in a non-interacting sample of this type which produces a fringe pattern, the particles are moved into the high intensity region and create periodic density modes. This in fact formed a diffraction grating which scattered light.

These density modes can be probed by self-scattered, by degenerate or by non-degenerate four wave mixing methods. As the intensity of the two crossed beams increased, the force gradient on the particles increased which localized the spheres strongly in the high intensity regions. It was observed that if the thermal energy (KT) is larger than the effective potential energy then the first order diffracted intensity from these density modes follows cubic dependence for self-scattering or non-degenerate four wave mixing. On the other hand, if the thermal energy is less than the effective potential energy of the spheres, the diffracted intensity from these density modes deviates from cubic dependence. A theoritical model had been developed by us which agrees with the experiment. In that model, we observed that higher order modes follow higher power dependence when thermal energy is less than the effective potential energy on the spheres and saturates if the effective potential energy on the spheres increases.

The growth and decay of the density modes has also been studied. D. Rogovan and co-workers (31) suggested in their model that higher order density modes will grow slowly. This was also observed. The growth of these density modes depends on the effective potential energy on the spheres. It was observed that the growth time is larger than the relaxation time when thermal energy is larger than the effective potential energy of the spheres and is smaller than relaxation time when effective potential energy of the spheres is larger than the thermal energy.

The diffusion of particles along a single boundary is different from the diffusion of the same particles without boundary. Due to the radiation pressure, the spheres move to the down stream wall and as the intensity of the crossed beams increases, the radiation pressure on the spheres increases which decreases the thickness of the boundary layer. When one of the crossed beams is blocked then these density modes decay. The decay is a single exponent but the diffusion constant is different from the diffusion of same spheres without boundary. In this case, the boundary layer undergoes a very high strain. This creates an extra drag force on the spheres. As the thickness of the boundary layer decreases, then a higher shear stress is needed in order to have the same strain. This has been observed when the diffusion of 2.02 um diameter spheres was found to be even slower than 1 um diameter spheres. This diffusion process is independent of thickness of the gap between the cell wall. Since the radiation pressure on the less than .5 um diameter spheres is less, the effect of boundary is very small, and the diffusion constant obtained by this method is in approximate agreement with value of the diffusion constant without boundary.

When these highly charged dielectric spheres are kept in a highly deionized aqueous environment, they exhibit a interparticle ordering over a distance considerably larger than the diameter of the spheres due to the coulombic interactions. The local ordering of these interacting particles has been observed by crossed correlation intensity fluctuation (CCIFS) methods (2,3,4). This coulombic interacting potential is spherically symmetric. However, if the sample is subjected to a one dimensional periodic potential produced by crossing two laser beams (CBT) in the sample, the spherical symmetry of the amorphous liquid like order breaks and exhibits two dimensional periodicity. In Chapter II, it was shown that when the thermal energy of the particles is larger than the effective potential energy of the particles then mathematically CBT and CCIFS are related to each other (35). It was observed that the two experiments are in agreement where CCIFS minitors the statistical local ordering and CBT monitor the induced long range ordering. It was also found that when the fringe separation is equal to the square root of half of the square of the average particle separation, then they form a two dimensional square lattice with its principle axis along the secondary registration direction. On the other hand, when the fringe separation is .866a (average particle separation) then they form a hexagonal close pack structure. In between these separations they exhibit a destorted hexagonal structure.

The diffracted intensity from these Bragg's spots was studied, and it was found that the diffracted intensity from the fundamental registration follows a cubic power dependence of the input power and the diffracted intensity from the secondary registration follows a three-halves power dependence of input power for thermal energy less than effective potential energy for self-diffraction method. It was found in the Landau free energy minimization theory that the fundamental modes can grow continuously for a continuous increase of input power and secondary modes grow continuously from certain threshold values (6).

Experimentally we found that the secondary modes grow continuously for a continuous increase in input power. The liquid symmetry of the sample breaks continuously when the sample is subjected in a periodic intensity potential.

The growth and decay of the fundamental modes and secondary modes has also been studied. It was found that when the fringe separation is 0.867 times the average particle separation, the fundamental modes grow faster than when the fringe separation is less than that for the same input power. This is due to the presence of interaction potential of the spheres. It was also observed that fundamental modes grow faster than secondary modes.

When one of the write beams is blocked the structure decays. The decay of the fundamental mode is not a single exponential and this structure stays in its metastable state for few moments which is termed the "free induction decay". This "free induction decay" is followed by a faster and then a slower decay process. Experimentally, it was found that initial decay of the fundamental mode is even faster than the decay of non-interacting particles for same scattering angle. The initial decay of the secondary modes was even faster than the decay of the fundamental modes. Since we are limited by the apparatus, the detail of the decay process of the secondary modes is not possible at this time.

Finally we found that CBT is a very powerful tool which can be used in both solids and liquids to monitor the structure. This method allows us to study the diffusion of microspheres near a single boundary; it even allows different thickness of the boundary layer to be studied. We found quantitative agreement between CBT and CCIFS in monitoring the structure.

Suggestions for Future Work

So far we have collected a drop of water out of an ocean in this experiment. The mathematical model we developed agrees excellently with our experiment for non-interacting particles. We have also observed that while the Landau theory does explain our data qualitatively, it does not explain the continuous growth of the structure quantitatively. The growth of density modes has been explained by us and by D. Rogovin and his co-workers; and works excellently for non-interacting case when there is no boundary or the effect of the boundary is very small. In the case of the interacting samples, there is not a single mathematical model to explain this growth and decay. On the basis of the observation we made for this thesis, the following future suggestions are made as follows:

1. The growth and decay of the density modes near a single boundary needs to be studied in further detail in order to get a relation between thickness of the boundary layer and applied force on the paticles. This needs very fine measurements of the force acting on the spheres. A mathematical model needs to be developed in order to explain the results.

2. The behavior of the higher order density modes which are not excited directly, needs to be studied as a function input power and strength of interaction for an interacting sample. A theoretical model has to be developed to explain quantitatively the higher order density modes.

3. The growth and decay of the fundamental density modes needs to be studied further as a function of input power and quantitatively analyzed as a function of the strength of the interactions.

4. The growth and decay of the secondary and higher order density modes needs to be studied further for faster sampling rate. A theoretical model is needed in order to explain these growths and decays.

5. So far we have studied the spherical symmetry of the liquid which can be broken by applying an external periodic potential. In this case, the strength of the interaction potential is not known accurately. The interaction potential can be generated in the sample externally in a controlled way for example by applying a magnetic field to the colloidal particles imbeded in a ferro fluid. This will allow further studies of laser freezing.

6. All of these studies can also be performed in a three dimensional sample.

In order to understand the statistical behavior of micro-size particles these are the minimum studies necessary.

A SELECTED BIBLIOGRAPHY

1. P.W.Smith, A.Ashkin and W.J.Tomlinson, Optics Letters, Vol.6, No.6, p284, (1981).

2. N.A.Clark, B.J.Ackerson and A.J.Hurd, Phys. Rev. Letts. Vol.50, No.19, p1459 (1983).

3. B.J.Ackerson and N.A.Clark, Faraday Discuss Chem. Soc. Vol.76, p219 (1983).

4. B.J.Ackerson, T.W.Tayler and N.A.Clark, Phys. Rev. A, Vol.31, No.5, p3183 (1985).

5. A.J.Hurd. Ph.D. Thesis, University of Colorado, Boulder.

6. A.Chowdhury, B.J.Ackerson and N.A.Clark. Phys. Rev. Letts, Vol.55, No.8, p833 (1985).

7. D.Ronis, Phys. Rev. Letts. Vol.52, p473 (1984).

8. Milton Kerker, The Scattering of Light and other Electromagnetic Radiation, Milton Kerker, Academic Press, New York and London.

9. W.A.Farone and M.J.Robinson III. Appl. Opts. Vol.7, No.4, p643 (1968).

10. Light Scattering by Small Sphere. H.C.Van De Hulst. John Willy and Sons. Inc. New York.

11. R.O.Gumprecht and C.M.Sliepecvich. J. Phys. Chem. Vol.57, p90 (1953).

12. Tables of Scattering Functions of Spherical Particles. National Bureau of Standards Applied Mathematics. Series-4, U.S.A. Government Printing Office. Washington D.C. (1948).

13. W.J.Pengonis, W.Heller and A.Jacobson. Table of Light Scattering Functions for Spherical Particles. Wayne State University Press, Detroit, (1957).

14. H.Z.Cummins and E.R.Pike. Photon Correlation Spectroscopy and Velocitmetry, Plenum Press, New York and London.

15. M.A.Omar. Elementry Solid State Physics, Addison-Wesley Publishing Company, Massachusetts, USA.

16. J.M.Robbins. M.S. Thesis, Okalhoma State University, Stillwater, Okalhoma.

17. B.Crosignani, P.Di Proto and M.Bertolotli. Statistical Properties of Scattered Light, Academic Press, New York, (1975).

18. B.J.Ackerson. J.Chem. Phys. Vol.64, p242 (1976).

19. B.J.Ackerson, P.N.Pusey and R.J.A.Tough. J. Chem. Phys. Vol.76, No.3, p1279 (1982).

20. D.Chatenay, W.Urbach, A.M.Cazabat and D.Lengevin. Phys. Rev. Letts. Vol.54, No.20, p2253 (1985).

21. R.Pecora, Dynamic Light Scattering, Plenum Press. New York, USA.

22. G.K.Batchelor. J. Fluid Mech. Vol.52, p245(1972) and Vol.74, p11 (1976).

23. F.H.Stillinger and T.A.Weber. Phys. Rev. A. Vol.25, No.2, p978 (1982).

24. R.L.Abrams and R.C.Lind. Optics Letters. Vol.2, No.4, p94 (1978).

25. I.C.Khoo, Phys. Rev. A. Vol.25, No.2, p1040 (1982).

26. H.Eichler, G.Salje and H.Stahl. J. Appl. Phys. Vol.44, No.12, p5383 (1973).

27. D.W.Pohl, S.E.Schwarz and V.Irniger. Phys. Rev. Letts. Vol.31, No.1, p32 (1973).

28. A.M.Ghazzawi, J.K.Tyminski and R.C.Powell. Phys. Rev. B. Vol.30, No.12, p7182 (1984).

29. J.D.Jackson. Classical Electromagnetics. 2nd Edition, John Willy and Sons. Inc. New York.

30. J.P.Gordon. Phys. Rev. A. Vol.8, No.1, p14 (1973).

31. A.Ashkin. Phys. Rev. Letts. Vol.24, No.4, p156 (1970).

32. A.Ashkin. Science. Vol.210, No.4474, p1081 (1980).

33. A.Ashkin and J.M.Dziedzie. Appl. Phys. Letts. Vol.19, No.8, p283, (1971).

34. A.Ashkin and J.M.Dziedzie. Appl. Phys. Letts. Vol.24,

No.12, p586 (1974).

35. B.J.Ackerson and A.H.Chowdhury. Cross-Correlation Intensity Fluctuation Spectroscopy and Laser Trapping Studies of Colloidal Suspensions. Presented in the meeting on Statistical Mechanics, Oaxtapec, Mexico, Jan(6-8), (1986).

36. B.Jancovivi. Phys. Rev. Letts. Vol.19, No.1, p20 (1967).

37. N.D.Mermin, Phys.Rev. Vol.176, No.1, p250 (1968).

38. Per Bak and D.Mukaml. Phys. Rev. B. Vol.19, No.3, p1604 (1985).

39. J.Villain. Phys. Rev. Letts. Vol.41, No.1, p36 (1978).

40. Per Bak. Rep. Prog. Phys. Vol.45, p587 (1982).

41. J.R.Moody and R.M.Lindstrom. Anal. Chem. Vol.45, p2264 (1977).

42. D.Rogovin and S.Q.Sare. Phys. Rev. A. Vol.31, No.4, p2375 (1985).

43. D.Rogovin and P. McGrath. Phys. Rev. Letts. Vol.54, No.20, p2222 (1985).

44. D.Rogovin, R.McGrath and P.Yeh. Phys. Rev. Letts. Vol.55, No.26, p2864 (1985).

45. J.A.Wesson, H.Teakezoe, H.Yu and S.P.Chen. J. Appl. Phys. Vol.53, No.10, p6513 (1982).

46. H.Hervet, W.Urbach and F.Rondelez. J. Chem. Phys. Vol.68, No.6, p2725 (1978).

47. H.Eichler, G.Salje and H.Stahl. J. Appl. Phys. Vol.44, p5383 (1973).

48. D.W.Pohl, S.E.Schwarz and V.Irniger. Phys. Rev. Letts. Vol.31, No.32, p32 (1973).

49. J.Happel and H.Brenner. Low Reynolds Number Hydrodynamics. Prentice-Hall Inc. Englewood Cliffs, N.J.

50. P.Vasseur and R.G.Cox. Fluid Mechs. Vol.80, Part.3, p561 (1977).

51. S.Alexander and J.McTague. Phys. Rev. Letts. Vol.41, No.10, p702 (1978).

52. Decay of BCC-Structure and of Bond-Orientational

Order in a Fluid. by S.Hess
Institut Max von Laue - Paul Langevin
Avenue des Martyrs - 156 X - 38042 Grenoble
Cedex - France.

53. P.G.deGennes. Physics. Vol.3, p37 (1967).

APPENDIXES

APPENDIX A

We have seen that when two laser beams are crossed in an interacting colloidal sample, then the liquid symmetry of the sample is broken. The sample undergoes a phase change from liquid to solid crystalline phase. This solid crystalline structure will scatter light. This diffraction pattern of the Bragg's spots has been captured in a photographic flim. The scattering angle of these Bragg's spots were then measured by calculating the distance from the screen to the sample cell and the Bragg's spots.

The sample is sandwiched between two quartz plates and the refractive index of the scattering medium is different from the cell wall and environment. On the other hand, the two beams are incident at an angle to the cell wall. Therefore, the angles we measured from the photographic flim are not the exact scattering angle coming from the cell. The following mathematics will correct the measured scattering angle. It is helpful to consider the ray diagram given in figure (51).

Let us assume that 2θ is the crossing angle of the two beams, then θ is the angle of incidence on the cell wall measured from a normal to the wall and L is the distance from the screen to the cell. Let P be any Bragg's spot on the screen and making an angle ϕ_N with the normal, as shown

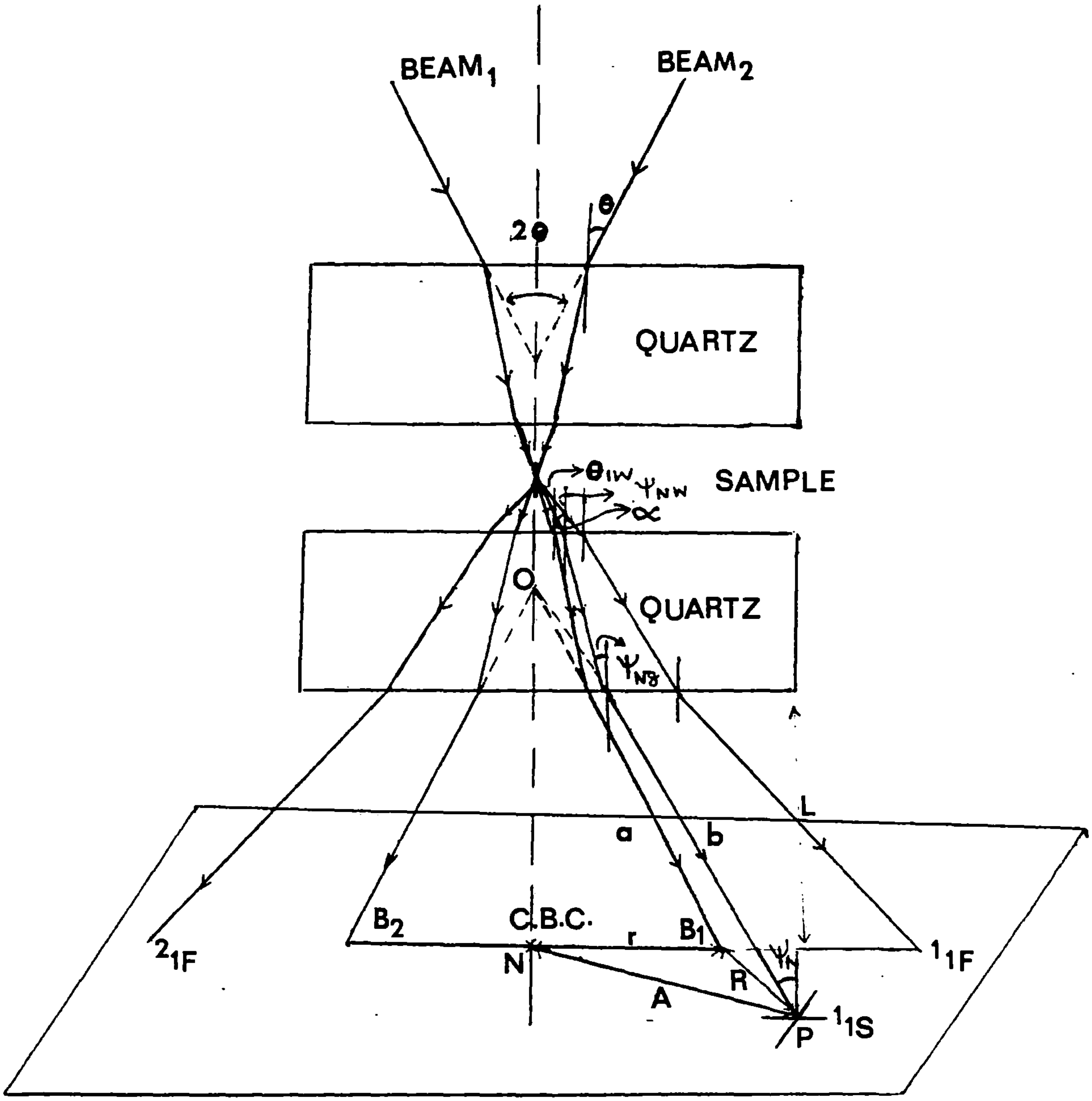

Figure 51. Scattering Geometry.

in figure (51). Using law's of refraction we get

$$n_a \sin(\phi_N) = n_g \sin(\phi_{N_g}) \qquad (A.1)$$

and

$$n_g \sin(\phi_{N_g}) = n_w \sin(\phi_{N_w}) \qquad (A.2)$$

where n_a , n_g , and n_w , are the refractive index of the air, the quartz and the sample, respectively. The angle ϕ_N , ϕ_{N_g} , and ϕ_{N_w} are the scattering angle of the same Bragg's spots in the air, the quartz and the sample, respectively. In practice the thickness of the quartz wall, q, is much smaller than the distance from the screen to the cell wall. Hence from the figure (51) we

$$\sin(\phi_N) = + A/\sqrt{(A^2 + L^2)} \qquad (A.3)$$

and

$$\sin(\phi_{N_w}) = (n_a/n_w) \sin(\phi_N) \qquad (A.4)$$

where A is the distance from the center position of the crossed beams to the Bragg spot. Let us assume that γ is the actual scattering angle and a and b are the distance from the scattering volume to the main scattering beam and point P respectively. Using the law's of triangle we get

$$a^2 + b^2 - 2ab \cos(\gamma) = R^2 \qquad (A.5)$$

$$a = r/[\sin(\theta_{lw})] \qquad (A.6)$$

and

$$b = A/[\sin(\phi_{N_w})] \qquad (A.7)$$

where R is the distance from one of the write beams to the

Bragg spot on the screen, r is the distance from the main beam to the center of the two crossed beams, θ is the half of the crossing angle in medium and ϕ_{Nw} is the angle between Bragg spot and center of the main beam. Finally putting everything together in terms of physically measurable quantities we have

$$\cos(\gamma) = (1/2)[\{(A \sin(\theta_{Iw}))/(r \sin(\phi_{Nw}))\} + \{(r \sin(\phi_{Nw}))/(A \sin(\theta_{Iw}))\} - \{(R^2 \sin(\theta_{Iw}) \sin(\phi_{Nw}))/(A\, r)\}]. \qquad (A.8)$$

The physically measurable quantities are R, r, A, L, θ_{Iw} and ϕ_{Nw} can be obtained from measurement and equation (A.4).

APPENDIX B

The size of the focused area is calculated by assuming that the diameter of the incident beam has a circular aperture. The expression for the optical disturbance at point P shown in figure (52), arising from the circular aperture in the far-field case is

$$E = E_A [\{\exp i(wt - kR)\}/R] \int_{aperture} \{\exp ik(Yy + Zz)/R\} \, ds \qquad (B.1)$$

where E_A is the amplitude of the electric field.

From the symmetry of the problem, spherical polar coordinates can be used for both cases and the equation (B.1) becomes

$$E = E_A [\{\exp i(wt - kR)\}/R] \int_0^{2\pi} \int_0^{a} \exp \{i(Kqp/R) \cos(\varnothing' - \varnothing)\} \, p \, dp \, d\varnothing \qquad (B.2)$$

Because of the complete axial symmetry, the solution must be independent of $\varnothing'$. We might just set $\varnothing' = 0$ and carrying out the integral we get

$$E = E_A [\{\exp i(wt - kR)\}/R] \, 2\pi$$

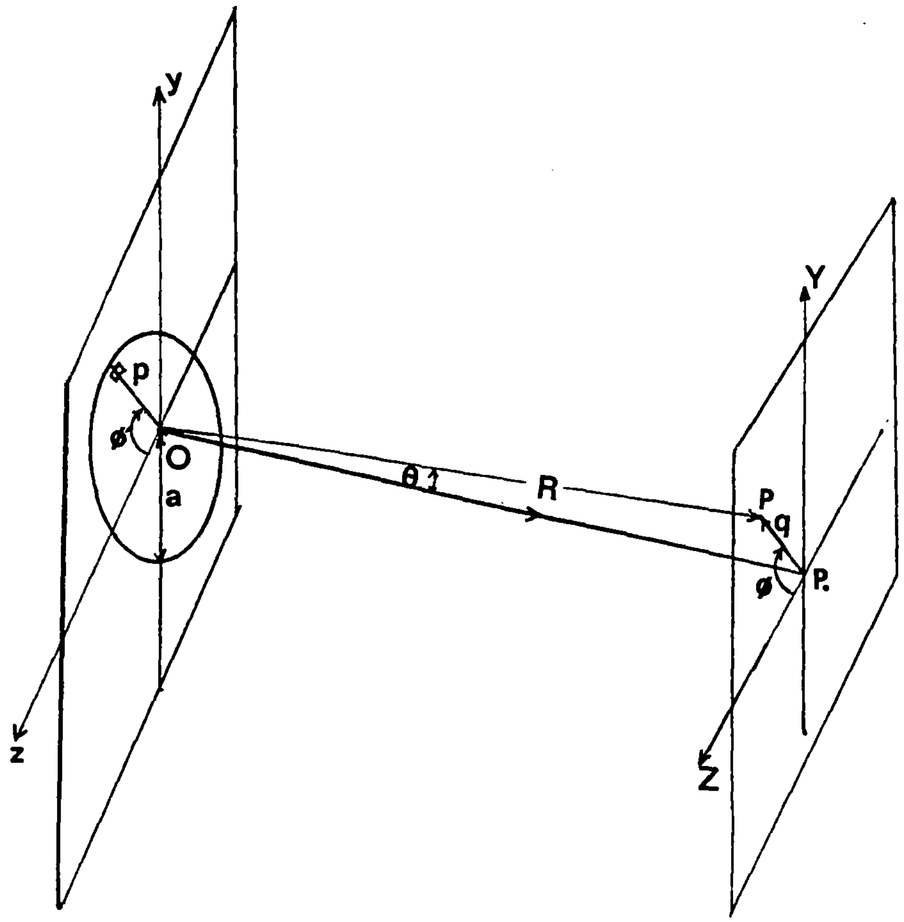

Figure 52. Circular Aperture Geometry.

$$\int_0^a J_0(Kqp/R)\ p\ dp \qquad (B.3)$$

where $J_0(Kqp/R)$ is the 0th order Bessel function.

Finally we get

$$E = E_A\ [(\exp\ i(wt - KR))/R]\ 2\pi\ a\ (r/Kqa)$$

$$J_1(kqa/R) \qquad (B.4)$$

where $J_1(Kqa/R)$ is the 1st order Bessel function.

The irradiance, I (intensity), at point P is $\langle(\text{Re } E)^2\rangle$ or $(1/2)(\bar{E}^*\bar{E})$ which is

$$I = [(2\ E_A^2\ A)/R^2][(J_1(kqa/R))/(kqa/R)]^2 \qquad (B.5)$$

where A is the area of the aperture $(=\pi a^2)$.

Because of the axial symmetry, the towering central maximum corresponds to a high intensity circular spot known as the Airy disk. First order zero occurs

$$J_1(Kqa/R) = 0$$

when $kqa/R = 3.83 \qquad (B.6)$

and for lens with focal length, f is given by

$$q = 1.22\ (\lambda f)/D$$

where $D = 2a$ is the diameter of the aperture

λ is the wavelength

and $f = R$.

APPENDIX C

```
10  REM  THIS IS THE MASTER PROGR
AM FOR AI13.A/D CONVERTER
20  REM  IT WILL COLLECT DATA AT
GIVEN TIME INTERVAL FOR
30  REM  FALLING EDGE OF THE TRIG
GERING
31  REM
40  LOMEM: 16384
50  HIMEM: 36864
55  PRINT  CHR$ (4)"BLOAD GETAI13
.DELAY"
60 D$ =  CHR$ (4)
70 G$ =  CHR$ (9)
75  DIM A%(1,1024)
80  REM
81  REM  THIS INTEGER ARRAY IS FO
R CHANNEL AND DATA
82  REM  THE DATAS COME IN INTEGE
R FORM
83  REM
90  DIM B(512),T(512)
91  REM
100  REM  THESE ARE DONE TO CONVE
RT NUMBER TO VOLTAGE
110  REM  FOR CERTAIN GAIN CODE
111  REM
120  DIM S(7):S(0) = 5 / 4096:S(1
) = S(0) / 5:S(2) = S(0) / 1
0:S(3) = S(0) / 50: FOR I =
4 TO 7:S(I) = S(I - 4) + S(I
 - 4): NEXT I
130  DIM O(7):O(4) =  - 5:O(5) =
 - 1:S(6) =  - .5:S(7) =  -
.1
140  REM
150  REM  THIS FLAGS ARE FOR SOFT
WARE TRIGGERING
160  REM
200 FLAG = 1
210 FLAG1 = 0
220 N1 = 0
230 L1 = 0
235 K = 0
240  REM
250  HOME
260  PRINT
270  PRINT " GETAI13.DELAY IS A A
SSEMBLY LANGUAGE"
280  PRINT " ROUTINE WHICH MAKES
A SERIES OF AI13"
290  PRINT " READINGS EACH TIME I
```

```
T IS CALLED."
300  PRINT : PRINT " THE LIST OF
READINGS IS PUT IN A"
310  PRINT " BASIC ARRAY, GETAI13
 IS CALLED,"
320  PRINT " AND THE RESULTS ARE
RETURNED IN THE"
330  PRINT " SAME BASIC ARRAY."
340  PRINT
350  PRINT " OLD OR NEW (O/N) "
360  GET A$
370  IF A$ = "O" THEN 5000
380  IF A$ = "N" THEN 1000
997  REM
998  REM  GETAI13 IS IN SLOT # 5

999  REM
1000 A%(0,0) = 5:A(1,0) = 0
1010  TEXT
1020  INPUT " NUMBER OF RUN N = "
;N
1030 N1 = N1 + N
1040  IF FLAG1 > 0 THEN 2000
1050  INPUT " CHANNEL? (0-15 OR R
ETURN) ";CHAN$
1060 CHAN =  VAL (CHAN$): IF CHAN
$ = "" THEN 5000
1070  PRINT
1075  PRINT "     G A I N       C
 O D E "
1080  PRINT "  0  =  0 TO 5V    4
  =  -5 TO +5V"
1090  PRINT "  1  =  0 TO 1V    5
  =  -1 TO +1V"
1100  PRINT "  2  =  0 TO .5V   6
  =  -.5 TO +.5V"
1110  PRINT "  3  =  0 TO .1V   7
  =  -.1 TO +.1V"
1120  PRINT
1130  REM
1140  REM  THESE ARE THE GAIN COD
E
1150  REM
1160  INPUT " ENTER GAIN CODE = "
;GAIN
1170  INPUT " ENTER TRIGGERING CH
ANNEL NUMBER = ";C
1180  INPUT " EVEN # OF DATA POIN
T (0 - 1024) = ";D2
1190  INPUT " ENTER DELAY (1 TO 2
55) ";D
1198  REM
1199  REM  DELAY = 162 + (7*SUM O
```

```
1540 I1 = (2 * I) - 1
1550  IF A%(1,I1) < 3500 AND A%(1
,I1 + 1) > 3500 THEN 1570
1560  GOTO 1530
1570 SP = 1:EP = SP + 500
1580 P = 500
1590  FOR J = 1 TO P
1600 P1 = SP + J
1610 B(J) = B(J) + A%(1,P1)
1620  NEXT J
1630  PRINT "RUN NUMBER = ";K
1640 L1 = L1 + 1
1650  IF L1 = 10 OR K = N1 THEN 1
670
1660  GOTO 2000
1670  HGR : HCOLOR= 3: SCALE= 1: HPLOT
0,0 TO 0,157: HPLOT 0,157 TO
279,157
1680 Z1 = 1
1690 Z2 = Z1 + 1
1700 X1 = Z1:X2 = Z2:Z3 = (2 * Z1
) - 1:Z4 = (2 * Z1) + 1:Z5 =
2 * Z1:Z6 = (2 * Z1) + 2
1710 Y1 = 155 -  INT (B(Z3) / (26
.5 * K)):Y2 = 155 -  INT (B(
Z5) / (26.5 * K)):Y3 = 155 -
 INT (B(Z4) / (26.5 * K)):Y4
 = 155 -  INT (B(Z6) / (26.5
 * K))
1720  SCALE= 1
1730  HPLOT X1,Y1 TO X2,Y3
1740  HPLOT X1,Y2 TO X2,Y4
1750 I = I + 1
1760 Z1 = Z1 + 1
1770  IF (Z1 + 3) < Y THEN 1690
1780  PRINT " RUN NUMBER = ";K
1790 L1 = 0
1800 FLAG1 = FLAG1 + 1
2000  IF K < N1 THEN 1410
2010  INPUT " DO U WANT TO RUN IT
 (Y/N) ";A$
2020  IF A$ = "Y" THEN 1020
2030  INPUT " WANT TO SAVE IT (Y/
N) ";A$
2040  IF A$ = "N" THEN 200
2050  FOR J = 1 TO 500
2060 T(J) = (J - 1) * D1
2070 G% = A%(0,J) / 16:C% = A%(0,
```

```
F NUMBER UPTO D)
1200  REM
1210 S1 = 0
1220  FOR I = 1 TO D:S1 = S1 + I:
 NEXT I
1230 D1 = 162 + (7 * S1)
1240 A%(1,0) =  - D2
1250 M = D2 / 2
1260  FOR I = 1 TO M
1270 I1 = (2 * I) - 1:I2 = 2 * I
1280 A%(0,I1) = C:A%(0,I2) = CHAN
 + 16 * GAIN
1290 A%(1,I1) = 0:A%(0,I2) = 0
1300  NEXT I
1310  REM
1320  REM  LOADIND A%(0,I) WITH T
HE ADDRESS OF CHANNEL NUMBER
 AND GAIN
1330  REM  LOADING A%(1,I) WITH Z
ERO FOR DATA COLLECTION
1340  REM
1350  REM  FOR TRIGGERING THE CIR
CUIT THIS PORTION OF THE BAS
IC PROGRAM IS
1360  REM  RESPONSIBLE WHERE THE
ADDRESS OF AI13 IN A%(0,0) L
OCATION
1370  REM
1380 AI13 =  - 16256 + A%(0,0) *
16
1390  GOTO 1410
1400 FLAG = 0
1410  POKE AI13,C
1420 RESULT =  PEEK (AI13 + 1) *
256 +  PEEK (AI13)
1430  IF RESULT > 3900 THEN 1400
1440  IF FLAG = 1 THEN 1410
1450 K = K + 1
1460  REM
1470  REM  REDAY TO TAKE DATA IN
SOME TIME INTERVAL SPECIFY B
Y D.
1480  REM
1490  POKE 25,D
1500  POKE 8,1: CALL 36864
1510 FLAG = 1
1520 I = 0
1530 I = I + 1
```

```
J) - (G% * 16)
2080 B(J) =  INT ((B(J) * S(G%) +
O(G%)) * 100000) / 100
2090 B(J) =  INT (B(J) / K)
2100  NEXT J
2110 M = 2 * P
2200  INPUT " NAME OF THE FILE ";
F$
2210  INPUT " PLACE THE DISK INTO
 THE DRIVE AND HIT RETURN";G
$
2220  PRINT D$"OPEN"F$
2230  PRINT D$"WRITE"F$
2240  PRINT M
2250  FOR I = 1 TO P
2260  PRINT T(I)
2270  PRINT B(I)
2280  NEXT I
2290  PRINT D$"CLOSE"F$
2300  GOTO 6000
5000  INPUT " NAME OF THE FILE =
";F$
5010  PRINT D$"NOMON C,I,O"
5020  PRINT
5030  PRINT D$"OPEN"F$
5040  PRINT D$"READ"F$
5050  INPUT I
5055  DIM A$(I)
5060  FOR J = 1 TO I
5070  INPUT A$(J): NEXT J
5080  PRINT D$"CLOSE"F$
5090  PRINT D$"MON C,I,O"
5100 " WANT A HARD COPY (Y/N) ";A
$
5110  IF A$ = "N" THEN 5490
5120  PRINT D$;"PR#1"
5130  PRINT " TIME (IN MICROSECON
D)     DATA (IN VOLTS)"
5140  FOR J = 1 TO I
5150 J1 = (2 * J) - 1:J2 = 2 * J
5160  PRINT  VAL (A$(J1)); TAB( 3
0); VAL (A$(J2))
5170  NEXT J
5180  PRINT D$;"PR#0"
5490  GOTO 200
5500  IF  PEEK ( - 16384) > 127 THEN
 POKE  - 16368,0: GOTO 5900
5550  GOTO 1500
5900  GOTO 1280
6000  END
```

APPENDIX D

```
1  REM
2  REM  THIS PROGRAM WILL TAKE DA
TA AND
3  REM  DISPLAY THE WEIGHTED AVER
AGE ON
4  REM  THE MONITOR AND PRINTER.
5  REM
6 M = 0
10  INPUT "WEIGHTING FACTOR W = "
;W
20 S1 = 0:S2 = 0
30 T1 = 0:T2 = 0
31  REM
32  REM  AI13 IS IN SLOT 5 OF APP
LE IIe
33  REM
35 SLOT = 5
40 AI13 =  - 16256 + SLOT * 16
50  INPUT " CHANNEL NUMBER C1 & C
2 ";C1,C2
51  REM
52  REM  GAIN CODE IS ZERO (MEAN
0 TO 5 VOLT RANGE)
53  REM
60 G = 0
70  POKE AI13,C1 + 16 * G
80 R1 =  PEEK (AI13 + 1) * 256 +
 PEEK (AI13)
90 V1 = R1 * 5 / 4095
100  POKE AI13,C2 + 16 * G
110 R2 =  PEEK (AI13 + 1) * 256 +
 PEEK (AI13)
120 V2 = R2 * 5 / 4095
130 S1 = V1 + (W * S1)
140 S2 = V2 + (W * S2)
150 T1 = (V1 * V1) + (W * T1)
160 T2 = (V2 * V2) + (W * T2)
170 Q1 =  SQR (T1 * (1 - W) - (S1
 * (1 - W)) ^ 2)
180 Q2 =  SQR (T2 * (1 - W) - (S2
 * (1 - W)) ^ 2)
190  PRINT S1 * (1 - W);" -+ ";Q1
;"     ";S2 * (1 - W);" -+ "
;Q2
200 M = M + 1
210  IF M = 10 THEN 230
220  GOTO 70
230  PRINT D$;"PR#1"
240  PRINT S1 * (1 - W);" -+ ";Q1
;"     ";S2 * (1 - W);" -+ "
;Q2
250 M = 0
260  PRINT D$;"PR#0"
270  GOTO 70
```

APPENDIX E

```
0000:              2 ;
0000:              3 ; INTERACTIVE STRUCTURES INC
0000:              4 ;    DAT DEC '80
0000:              5 ;
0000:              6 ;   AI13 TO APPLESOFT ARRAY
0000:              7 ;


0000:              9 ;
0000:             10 ; VARIABLE DEFINITIONS
0000:             11 ;
C080:             12 DEV     EQU  $C080     DEVICE SELECT LOCATION
006B:             13 AARY    EQU  $6B       APPLESOFT ARRAY POINTER
006D:             14 AARYE   EQU  $6D       APPLESOFT ARRAY END
0006:             15 PTR     EQU  6
0008:             16 ARYPTR  EQU  8
003C:             17 OLDCH   EQU  $3C       LAST CHANNEL/GAIN USED
003D:             18 DELAY   EQU  $3D       DELAY COUNTER
0006:             19 DLYVAL  EQU  6         FOR ABOUT 45 MS DELAY
00F9:             20 STASUB  EQU  $F9       'STA DEV+SLOT*16'


----- NEXT OBJECT FILE NAME IS GETAI13
9000:             22         ORG  $9000
9000:             23 ;
9000:             24 ; THIS ROUTINE TAKES THE N'TH INTEGER ARRAY
9000:             25 ;  TO DETERMINE THE SAMPLING SEQUENCE FOR
9000:             26 ;  THE AI13.  BEFORE USE DIMENSION A YOUR
9000:             27 ;  ARRAYS AS 1 BY N.  THE (0,0) ELEMENT
9000:             28 ;  CONTAINS THE SLOT NUMBER FOR THE AI13.
9000:             29 ;  THE (0,1)'TH ELEMENT CONTAINS THE
9000:             30 ;   NEGATIVE OF THE NUMBER
9000:             31 ;  OF SAMPLES TO TAKE (LESS THAN THE
9000:             32 ;  ARRAY DIMENSION SIZE)
9000:             33 ;  THEN FILL THE (0,I)'TH ELEMENTS WITH
9000:             34 ;  THE AI13 ADDRESS/GAIN PARAMETERS.
9000:             35 ;   IF THIS IS NEGATIVE THIS SAMPLE IS SKIPPED
9000:             36 ;  AFTER CALLING THE (1,I)'TH ELEMENTS WILL
9000:             37 ;  CONTAIN THE VALUES.
9000:             38 ;  TO SELECT THE ARRAY TO USE POKE
9000:             39 ;  ITS NUMBER INTO LOCATION 8 BEFORE CALLING.
9000:             40 ; NOTE: THIS LOCATION IS CLOBBERED!
9000:             41 ;
9000:             42 GETAI13 EQU  *
9000:A5 6B        43         LDA  AARY      GET START OF ARRAY SPACE
9002:85 06        44         STA  PTR
9004:A5 6C        45         LDA  AARY+1
9006:85 07        46         STA  PTR+1
9008:A0 00        47 GAA1    LDY  #0
900A:B1 06        48         LDA  (PTR),Y
900C:10 24        49         BPL  GNARY1
900E:C8           50         INY
900F:B1 06        51         LDA  (PTR),Y
9011:10 20        52         BPL  GNARY
9013:C6 08        53         DEC  ARYPTR
9015:D0 1C        54         BNE  GNARY
9017:C8           55         INY
```

```
9018:C8          56         INY
9019:C8          57         INY
901A:B1 06       58         LDA  (PTR),Y    GET NUMBER OF DIMENSIONS
901C:AA          59         TAX             WE WANT TO SKIP OVER THEM
901D:C8          60         INY
901E:C8          61 GAA2    INY
901F:C8          62         INY
9020:CA          63         DEX
9021:D0 FB       64         BNE  GAA2
9023:98          65         TYA
9024:18          66         CLC
9025:65 06       67         ADC  PTR
9027:85 08       68         STA  ARYPTR     NOW GET REAL POINTER
9029:A9 00       69         LDA  #0
902B:65 07       70         ADC  PTR+1
902D:85 09       71         STA  ARYPTR+1
902F:18          72         CLC
9030:90 22       73         BCC  GETOK      GOT THE ARRAY
9032:C8          74 GNARY1  INY
9033:C8          75 GNARY   INY
9034:18          76         CLC
9035:B1 06       77         LDA  (PTR),Y    POINT TO NEXT ARRAY
9037:65 06       78         ADC  PTR
9039:48          79         PHA             CAN'T OVERWRITE JUST YET
903A:C8          80         INY
903B:B1 06       81         LDA  (PTR),Y
903D:65 07       82         ADC  PTR+1
903F:85 07       83         STA  PTR+1
9041:68          84         PLA             NOW WE CAN
9042:85 06       85         STA  PTR
9044:A5 07       86         LDA  PTR+1
9046:C5 6E       87         CMP  AARYE+1    SEE IF PAST END
9048:F0 03       88         BEQ  GNAA2
904A:90 BC       89         BCC  GAA1
904C:60          90 GNAA3   RTS             RETURN WITHOUT DOING ANYTHING
904D:A5 06       91 GNAA2   LDA  PTR
904F:C5 6D       92         CMP  AARYE
9051:90 B5       93         BCC  GAA1
9053:60          94         RTS

9054:            96 GETOK   EQU  *          NOW GOT THE ARRAY
9054:A9 8D       97         LDA  #$8D       'STA' OPCODE
9056:85 F9       98         STA  STASUB     SETUP A STORE SUBROUTINE
9058:A9 C0       99         LDA  #$C0
905A:85 FB      100         STA  STASUB+2
905C:A9 60      101         LDA  #$60       'RTS'
905E:85 FC      102         STA  STASUB+3
9060:A0 01      103         LDY  #1         WANT THE SLOT #
9062:B1 08      104         LDA  (ARYPTR),Y
9064:29 07      105         AND  #7         JUST IN CASE
9066:0A         106         ASL  A          TIMES 16
9067:0A         107         ASL  A
9068:0A         108         ASL  A
9069:0A         109         ASL  A
906A:AA         110         TAX
906B:09 80      111         ORA  #$80
906D:85 FA      112         STA  STASUB+1
906F:C8         113         INY             NOW GET NUMBER OF SAMPLES
```

```
9070:B1 08              LDA  (ARYPTR),Y
9072:85 07              STA  PTR+1
9074:C8                 INY
9075:B1 08              LDA  (ARYPTR),Y
9077:85 06              STA  PTR
9079:A9 00              LDA  #0         INITIALIZE OLD CHANNEL/GAIN
907B:85 3C              STA  OLDCH
907D:         GETLOOP   EQU  *
907D:18                 CLC
907E:A9 04              LDA  #4         POINT TO NEXT ELEMENT
9080:65 08              ADC  ARYPTR
9082:85 08              STA  ARYPTR
9084:A9 00              LDA  #0
9086:65 09              ADC  ARYPTR+1
9088:85 09              STA  ARYPTR+1
908A:A9 06              LDA  #DLYVAL    INIT DELAY LOOP
908C:85 3D              STA  DELAY
908E:A0 00              LDY  #0         GET HI-ORDER BYTE
9090:B1 08              LDA  (ARYPTR),Y TO SEE IF SKIPPING
9092:30 29              BMI  SKIPTHIS
9094:C8                 INY             NOW FOR LO-ORDER BYTE
9095:B1 08              LDA  (ARYPTR),Y
9097:20 F9 00           JSR  STASUB     SETUP ADDRESS/GAIN
909A:48                 PHA
909B:C5 3C              CMP  OLDCH      SEE IF SAME AS BEFORE
909D:F0 08              BEQ  SKPDLY     YES, DON'T HAVE TO DELAY
909F:29 02              AND  #2         SEE IF HI-GAIN SETTINGS
90A1:F0 04              BEQ  SKPDLY     NO, LO-GAIN (FASTER)
90A3:C6 3D    WAITLP    DEC  DELAY      NOW TWIDDLE OUR THUMBS
90A5:D0 FC              BNE  WAITLP
90A7:68       SKPDLY    PLA             RESTORE CHANNEL/GAIN
90A8:85 3C              STA  OLDCH      UPDATE OLD
90AA:20 F9 00           JSR  STASUB     TAKES CARE OF OP-AMP SPROING
90AD:48                 PHA
90AE:68                 PLA
90AF:C8                 INY
90B0:BD 81 C0           LDA  DEV+1,X    THIS COMES OUT FIRST
90B3:29 0F              AND  #$F        AND OFF FLAGS
90B5:91 08              STA  (ARYPTR),Y SAVE HI-ORDER
90B7:C8                 INY
90B8:BD 80 C0           LDA  DEV,X
90BB:91 08              STA  (ARYPTR),Y AND LO-ORDER
90BD:         SKIPTHIS  EQU  *          # ELEMENTS COUNTER
90BD:E6 06              INC  PTR
90BF:D0 BC              BNE  GETLOOP
90C1:E6 07              INC  PTR+1
90C3:D0 B8              BNE  GETLOOP
90C5:60                 RTS

*** SUCCESSFUL ASSEMBLY: NO ERRORS
```

Source: AI13 Analog Input System Users Manual
Interactive Structures, Inc. P.O.Box 404
Bala Cynwyd, Pennsylvania

?

VITA

Aslam Habib Chowdhury

Candidate for the Degree of

Doctor of Philosophy

Thesis: LASER INDUCED FREEZING

Major Field: Physics

Biographical:

Personal Data: Born in Serajganj, Bangladesh, December 22, 1956, the son of Mr. Abul Hossain Chowdhury and Mrs. Sara Hossain Chowdhury. Married to Israt J. Chowdhury on February 7, 1980.

Education: Received Secondary School Certificate from Victoria High School, Serajganj, Bangladesh, in 1971; received Higher Secondary Certificate from Dacca College, Dhaka, Bangladesh, in 1973; received Bachelor of Science Degree in Physics from Dacca University, Dhaka, Bangladesh, in 1976; received Master of Science Degree in Physics from Dacca University, Dhaka, Bangladesh, in 1977; received Master of Science Degree in Physics from Marquette University, Milwaukee, Wisconsin, in December, 1982; completed requirements for the Doctor of Philosophy degree at Oklahoma State University in December, 1986.

Professional Experience: Research Fellow, Department of Physics, Dacca University, from February, 1980 to April, 1980; Lecturer, Department of Physics, Dacca University, from May, 1980 to August, 1980; Teaching Assistant, Physics Department, Marquette University, from August, 1980 to May, 1982; Teaching and Research Assistant, Department of Physics, Oklahoma State University, from August, 1982 to present.